2011

Evaluation of volumetric modulated arc therapy (VMAT) patient specific quality assurance

Gordon Mark Mancuso
Louisiana State University and Agricultural and Mechanical College

EVALUATION OF VOLUMETRIC MODULATED ARC THERAPY (VMAT) PATIENT SPECIFIC QUALITY ASSURANCE

A Thesis

Submitted to the Graduate Faculty of the
Louisiana State University and
Agricultural and Mechanical College
in partial fulfillment of the
requirements for the degree of
Master of Science

in

The Department of Physics and Astronomy

by
Gordon Mark Mancuso
B.S., Brigham Young University, 2008
May 2011

Acknowledgements

I am deeply indebted to a large number of people for supporting me during my academic career. This thesis work would not have been possible without my advisor, Dr. Jonas Fontenot, who has constantly been a source of guidance as he has assisted me in its completion. I'd like to thank my supervisory committee, consisting of the following people: Dr. John Gibbons, Dr. Gabriela González, Daniel Neck, and Dr. Brent Parker. I appreciate all of their comments, feedback, and encouragement, and for taking time from their busy schedules to meet with and assist me in this work.

I also would like to extend thanks to all of those who have guided and instructed me as part of my graduate experience, including Dr. Kenneth Matthews, Dr. Polad Shikhaliev, Dr. Wei-Hsung Wang, and Dr. Erno Sajo at LSU, and all of the faculty, staff, and physicians at Mary Bird Perkins Cancer Center. Without these people, I would not know about scintillation detectors, the Radon transform, the number of rems in a sievert, nor which flagon has the brew that is true. I especially want to thank Dr. Kenneth Hogstrom, whose dedication to this program, teaching, and to the advancement of medical physics has been a source of inspiration throughout my graduate career. I am also thankful to my fellow graduate students. We've been through a lot together, and I am sure some of us will have opportunities to work together in the future. I look forward to it.

Louisiana State University and Mary Bird Perkins Cancer Center deserve special thanks for supporting me both financially and with such excellent facilities in which to learn. In addition, I extend thanks to Elekta, Inc. for their part in sponsoring this research.

I'd like to thank Page Barcia, Susan Hammond, and Yvonne Thomas for all of their assistance and support throughout my graduate career. The medical physics program and the physics department at Mary Bird would have a difficult time functioning without their efforts and dedication.

My parents, Mark and Tammy Mancuso, have been a constant support to me throughout my life. As I grow older, I realize more and more how much they sacrificed to provide me with all the opportunities I have had. I thank them for always loving me and teaching me to stay on the right path, and for gently guiding me back when I've erred.

Finally, I am eternally grateful to my beautiful wife Megan, on whom I've come to rely more and more as time has passed. I am so very blessed to have her, and I am so thankful for her patience with me. I would be a lonely, sad, and hungry man without her.

Table of Contents

List of Tables

List of Figures

Abstract

Purpose: The purpose of this work was to perform a comprehensive comparison of fixed-beam intensity modulated radiation therapy (IMRT) and volumetric modulated arc therapy (VMAT) patient specific quality assurance (QA) results, in order to investigate the appropriateness of applying IMRT QA methods and action levels to VMAT treatment plans.

Methods: QA measurements were evaluated for the test geometries provided in AAPM Task Group Report 119. The structure sets were copied onto a cylindrical water-equivalent phantom. Using the Philips Pinnacle^3 treatment planning system, fixed-beam IMRT and VMAT treatment plans were constructed. The plans were delivered to the phantom and the resulting dose distributions were measured (1) in the coronal and sagittal planes and at high and low dose points in the cylindrical phantom using radiochromic film and ion chamber, respectively, and (2) using a commercial 2D diode array. Ion chamber and diode array measurements were taken five times each, and film measurements were taken three times. Measured planar doses were analyzed using gamma analysis with criteria of 3%/3 mm. Measured point doses were analyzed using percent difference. Differences between IMRT QA and VMAT QA results were tested for significance using the Wilcoxon rank-sum test.

Results: The radiochromic film results showed averages of 98.9%±1.0% and 99.1%±0.9% of measured doses within 3%/3 mm of calculated doses for IMRT and VMAT plans, respectively. Ion chamber results showed average differences between measured and calculated point doses of $-0.7\% \pm 1.5\%$ and $-1.7\% \pm 1.8\%$ for IMRT and VMAT plans, respectively. The diode array results showed averages of $98.7\% \pm 0.5\%$ and $98.6\% \pm 0.8\%$ of measured doses within 3%/3 mm of calculated doses for IMRT and VMAT plans, respectively. The Wilcoxon rank-sum test found p values of $p = 1.00$, $p = 0.27$, and $p = 0.89$ for the film, point dose, and diode array measurements, respectively.

Conclusion: Differences between IMRT QA and VMAT QA results were not statistically significant for any of the measurement types. The measured differences between IMRT and VMAT QA results were small and likely do not constitute clinically significant differences. These results suggest that it is appropriate to apply IMRT QA methods and action levels to VMAT treatments.

Chapter 1

Introduction

1.1 VMAT Overview

1.1.1 History of VMAT

IMRT

The primary goal of radiation therapy is to deliver a prescribed dose to a target volume, while minimizing the deleterious effects of radiation to normal tissue (Khan 2010). This is referred to as conforming the dose to the target. Various techniques are employed to achieve this goal. For example, multiple beams may enter the patient from different angles, all irradiating the target volume. The summing of doses at the focus point allows a high dose to be delivered there while comparatively lower doses are delivered to surrounding normal tissue. Another technique employed is to choose beam angles that avoid critical structures, thus reducing the dose to organs of comparatively low radiation tolerance.

A technique called intensity modulated radiation therapy (IMRT) is a method employed to further reduce dose to critical structures while maintaining a high uniform dose to a target volume. IMRT is distinguished from conventional radiotherapy by the ability to deliver fields of nonuniform intensity (Webb 2003). While wedges may be used in conventional therapy to achieve nonuniform intensity, wedges are inherently unidirectional and inflexible. IMRT, on the other hand, is much more adaptable. Figure 1.1 illustrates increasing conformity to the target. For much of the history of radiation therapy, treatment fields were limited to rectangular fields, with the addition of blocks and wedges. In Fig. 1.1(a), the rectangular field covers the dashed outline of the target, but also irradiates surrounding tissue due to the irregular shape of the target. While blocks can be used to reduce this effect, they are time consuming to construct, and changes to the treatment plan may require new blocks to be made. When multileaf collimators (MLCs) became available,

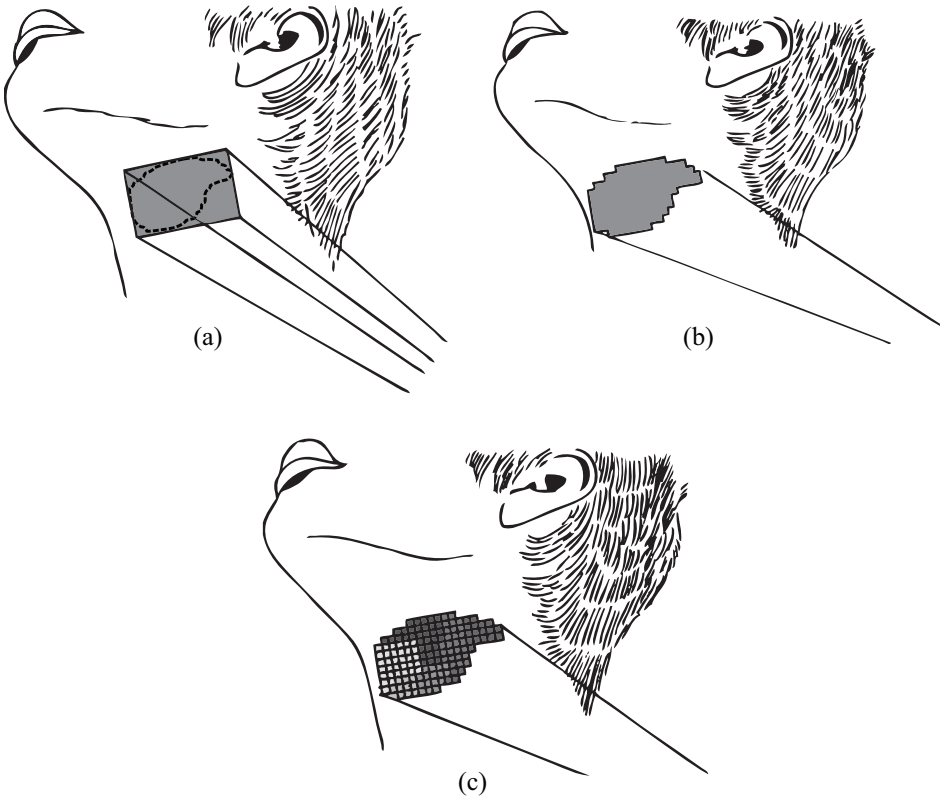

Figure 1.1: Increasing conformity to the target volume. (a) Treatment with rectangular fields was the treatment method used for almost a century, with the addition of wedges and blocks. (b) This illustrates 3D conformal radiotherapy, in which multileaf collimators make it easier to conform fields to the outline of a target. (c) IMRT allows the intensity to vary at different points in the field. Figure adapted from Webb (2003).

it became significantly easier to conform the radiation to the target shape (see Fig. 1.1(b)). This is typically referred to as 3D conformal radiotherapy (3DCRT). However, while MLCs shape the beam to follow the outline of the target, the beam is still of uniform intensity across the entire area being irradiated. Figure 1.1(c) illustrates the concept of utilizing varying intensities in each bixel in the radiation field, which is the primary distinction of IMRT. Different areas can receive differing amount of radiation from a single gantry angle. By adding up several of these fields from different angles, the composite dose distribution can yield a high uniform dose to the target while reducing the dose to the surrounding normal tissue.

IMRT offers a significant advantage over 3DCRT. A single beam using 3DCRT only conforms to the target in two dimensions, and 3DCRT cannot create a concave dose

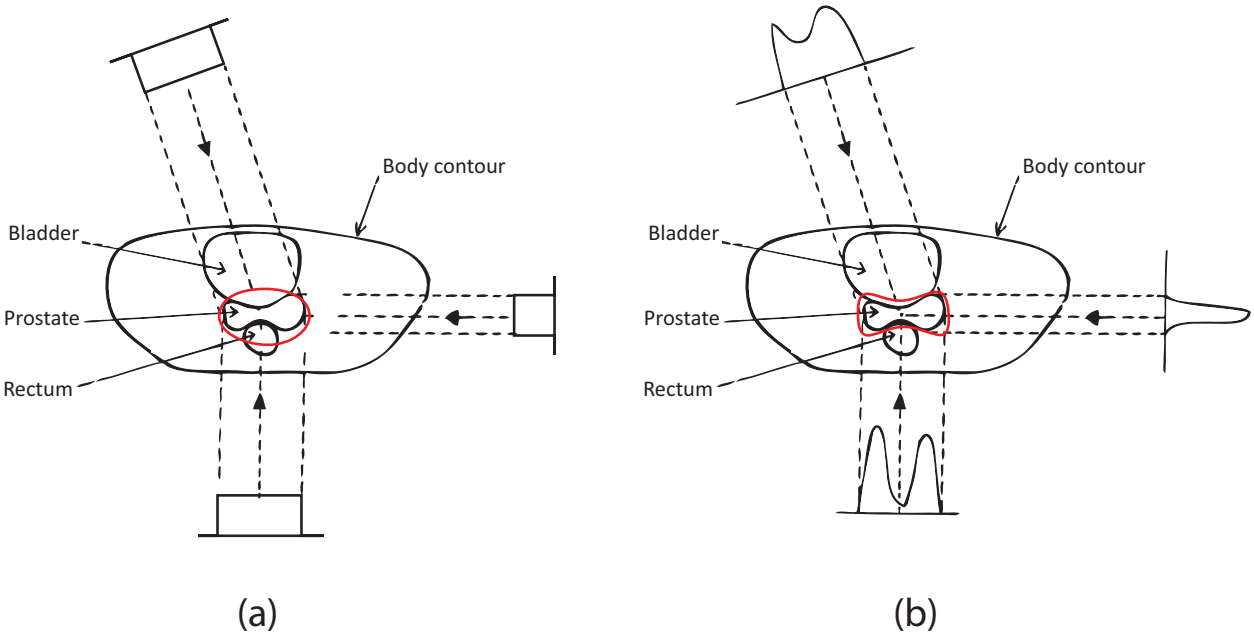

Figure 1.2: Example of how an IMRT treatment can conform to a concave target shape. Shown are (a) a 3DCRT treatment and (b) an IMRT treatment. The prostate is the target, and the rectum and bladder are organs at risk. A representative PTV isodose line is shown in red for each figure. 3DCRT delivers a uniform intensity over the field, and cannot create a concave dose distribution. IMRT can vary the intensity across the field, and thus provide better sparing of the organs in the concave regions. Figure adapted from Webb (2003).

distribution. As a result, planning target volumes (PTVs) with concave shapes, like the prostate shown in Fig. 1.2(a), will result in normal tissue in the concave areas being unnecessarily irradiated when treated with 3DCRT. IMRT, on the other hand, reduces the level of this unnecessary radiation, which is especially useful when organs at risk (OARs) lie in the concave regions. By decreasing the amount of radiation traveling through an OAR, the dose to the organ can be reduced without compromising the uniform dose to the target (see Fig. 1.2(b)). The use of IMRT has repeatedly been shown to reduce dose to OARs compared with 3DCRT (Arbea et al. 2010; Zabel et al. 2002).

Intensity modulation can be achieved in a number of ways. These include compensator based IMRT (Chang et al. 2004), helical slice-by-slice delivery (Mackie et al. 1993), and selective fluence modulation using an MLC. The last of these techniques can be achieved using two methods: "step-and-shoot" IMRT (SMLC-IMRT) and "dynamic" IMRT

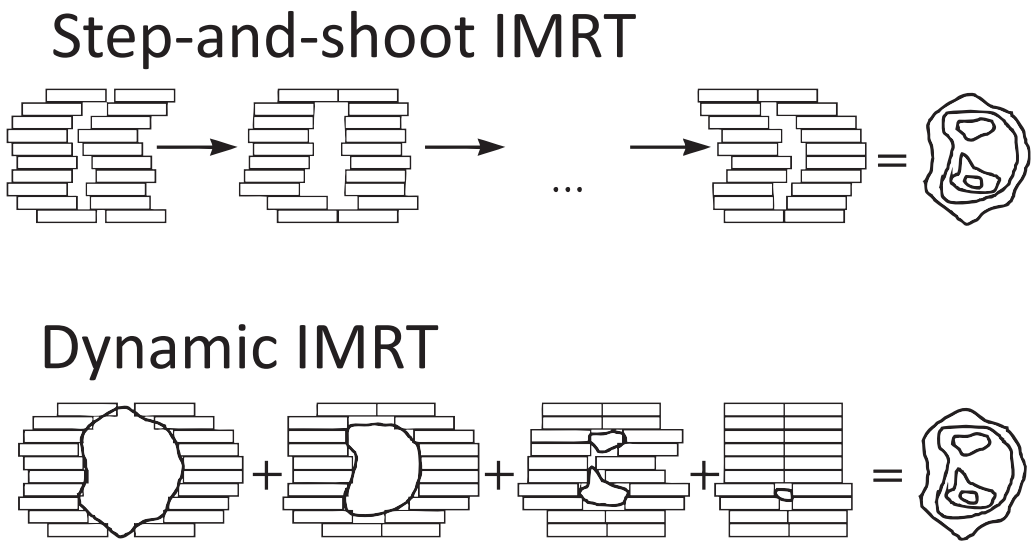

Figure 1.3: Methods of using MLCs to create intensity distributions. When the step-and-shoot method is used, the beam is off during leaf motion, while the dynamic method delivers radiation during leaf motion. Figure from Bortfeld et al. (1999).

(DMLC-IMRT). A graphical representation of these two methods is shown in Fig. 1.3. In step-and-shoot IMRT, the MLC leaves remain fixed during irradiation and the beam is turned off between consecutive MLC shapes. Several small static fields are added up to create the dose distribution. In dynamic IMRT, the leaves are in continuous motion while the beam is on, moving in and out of the field to create the desired dose distribution. It should be noted that the term "intensity modulation" is somewhat of a misnomer, as what is really being modulated is the fluence. However, the term "intensity modulation" has gained such widespread use that it is generally regarded as the proper method of referring to the technique.

VMAT

Volumetric modulated arc therapy (VMAT) is a method of delivering intensity modulated fields that is currently gaining widespread use. VMAT is distinguished from traditional fixed-beam IMRT in that the radiation is delivered while the gantry rotates around the patient. The dose is shaped using three variables: MLC shape, gantry rotation

speed, and dose rate. The primary advantage of VMAT over fixed-beam IMRT is that VMAT treatments can be delivered significantly faster.

VMAT evolved from intensity modulated arc therapy (IMAT), which was first proposed by Yu (1995). IMAT is similar to VMAT in that radiation is delivered while the gantry rotates around the patient. With IMAT, however, the dose rate and gantry speed are held constant. Intensity modulation is achieved by delivering radiation over multiple gantry arcs. This means that the number of intensity levels is equal to the number of gantry arcs. Increasing dose level resolution requires an increased number of arcs, which significantly increases treatment time. Yu found that IMAT treatments took as long or longer to deliver than comparable fixed-beam IMRT treatments. Yu observed that IMAT treatments spread normal tissue dose around the patient, while fixed-beam IMRT treatments concentrate the normal tissue dose along fixed lines.

Over the next decade, development of IMAT continued (Earl et al. 2003; Ma et al. 2001; Ramsey et al. 2001; Wong, Chen, and Greenland 2002; Yu et al. 2002), but the modality did not gain widespread clinical use. There were several reasons for this. First, there were no commercially available tools for routine treatment planning (Shepard et al. 2007). Second, the marginal dosimetric and delivery benefits of IMAT did not provoke much interest in furthering its development.

In 2007, Shepherd et al. showed that treatment planning with IMAT gave better results in fewer arc rotations when the gantry speed and dose rate were allowed to vary (Shepard et al. 2007). In 2008, Otto introduced the concept of volumetric modulated arc therapy, which was originally described as delivering the radiation dose in a single 360° arc (Otto 2008). This meant that treatments could be delivered significantly faster than with other IMRT options. At this point, there were sufficient incentives for rapid clinical and commercial development of VMAT tools and technology.

On Varian machines, VMAT is referred to as RapidArc, while on Elekta machines it is simply called VMAT.

1.1.2 VMAT Advantages and Disadvantages

VMAT has several potential advantages over traditional methods of IMRT delivery. The main advantage is that treatments are delivered in a fraction of the time as compared with fixed-beam IMRT treatments. Rao et al. (2010) compared VMAT treatments with fixed-beam IMRT and helical tomotherapy treatments. VMAT treatment times varied from 2.1 to 4.6 minutes, IMRT treatment times varied from 7.9 to 11.1 minutes, and tomotherapy treatment times varied from 4.0 to 7.0 minutes. Other work has shown similar decreases in treatment time (Otto, Milette, and Wu 2007; Otto 2008; Verbakel et al. 2009). The possible advantages of decreased treatment time include increased patient comfort and compliance, increased patient throughput, and enhanced image guidance.

Another advantage of VMAT is increased monitor unit (MU) efficiency, meaning fewer MUs are required to deliver the prescribed dose. Increased MU efficiency has two main effects: reducing the wear and tear on the treatment machine, and decreasing leakage and scatter dose. Rao et al. (2010) found that the VMAT treatments they planned used 18% fewer monitor units than fixed-beam IMRT plans for the same geometries. Others have found similar increased MU efficiency for VMAT treatments (Palma et al. 2008; Verbakel et al. 2009).

Both decreased treatment time and increased MU efficiency have been achieved while maintaining target coverage and OAR sparing similar to fixed-beam IMRT. In some cases, VMAT has shown better OAR sparing than fixed-beam IMRT (Otto 2008; Palma et al. 2008; Rao et al. 2010).

The main disadvantage of VMAT has been an increased optimization time as compared to fixed-beam IMRT (Rao et al. 2010). However, optimization times have decreased, and as techniques develop, this disadvantage will continue to be mitigated.

1.2 IMRT Patient Specific QA

Quality assurance (QA) in radiation therapy is the method used to ensure that the correct amount of radiation is being delivered to the correct location. QA is performed routinely

on all parts of the treatment process, from planning to delivery. The QA performed on traditional treatments tends to consist of testing the capabilities of the system. For example, the flatness and symmetry of the beam are measured to ensure they are within predetermined tolerances. When a system is found to be within these tolerances, traditional treatments are generally delivered without further testing of the individual plans, because the possible errors are few and are quantifiable (Ramsey, Dube, and Hendee 2003).

IMRT treatments, on the other hand, are considerably more complex than traditional treatments, and have a greater potential for delivery errors. In addition, IMRT often delivers treatment fields of higher doses that come closer to critical structures. This makes the consequences of misdelivery more pronounced than with traditional radiation therapy. Because of this, IMRT treatments are verified individually prior to being delivered to the patient. This is called "patient specific QA."

IMRT patient specific QA has several purposes. First, IMRT consists of the addition of many small fields delivered using precise positioning of the MLC, and the treatment planning system may have difficulty accurately modeling this kind of complexity. Patient specific QA ensures that the treatment planning system has accurately calculated the dose for the planned treatment. Second, patient specific QA verifies that the large amount of treatment data involved has been faithfully transferred from the treatment planning system to the record and verify system. Third, patient specific QA ensures that the delivery system is capable of delivering the fields as planned.

The most accurate QA possible would be performed by taking dosimetric measurements inside of the patient during the treatment delivery. However, this is not a practical method. Instead, treatment plans are typically copied onto a phantom geometry in which dosimetric measurements can be taken. The treatment is delivered to the phantom and measured doses are compared to calculated doses from the treatment planning system. The assumption is made that if the planning system can accurately predict the dose to a phantom, it can also accurately predict the dose to a patient.

Figure 1.4: The composite delivery method for patient specific IMRT QA. The entire treatment is delivered to the film or diode array in exactly the same manner as it is delivered to the patient.

The QA of fixed-beam IMRT treatments generally consists of two major parts: an absolute dose measurement to a reference point, and at least one measured plane of dose distribution (Létourneau et al. 2004). There are two widely used methods of performing the second of these parts:

(1) The first method is to deliver the entire treatment plan to the phantom while the composite dose distribution is measured (see Fig. 1.4). Film (radiographic or radiochromic) has been the typical dosimeter of choice for this method (Zeidan et al. 2006; Zhu et al. 2002), although recently diode arrays have been developed that can also perform adequately (Bedford et al. 2009; Jursinic, Sharma, and Reuter 2010). The advantage of this method is that the actual treatment is being delivered to the phantom exactly as it is delivered

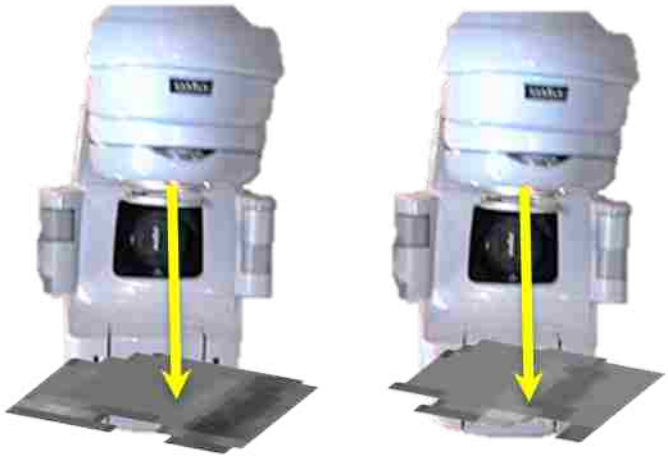

Figure 1.5: The field-by-field delivery method for patient specific IMRT QA. Each beam is delivered one at a time to film or a 2D diode array. The gantry remains in the same position for each beam, and each beam is analyzed separately.

to the patient. Effects such as gantry sag and couch attenuation are incorporated into the QA delivery. A historical disadvantage of this method has been a greater time and resource commitment, as the technique has been performed using film. However, with the increased use of diode based systems, this could become less of an issue. Another potential drawback is that it may be more difficult to pinpoint the sources of error when disagreement is found.

(2) The second method of verifying dose distributions is to deliver the IMRT beams one at a time in a field-by-field manner to the phantom from a single gantry angle (see Fig. 1.5); each beam is measured and compared separately (Van Esch et al. 2002). This can be done using film, but it has become increasingly common to perform the measurements using a 2D diode or ion chamber array (Buonamici et al. 2007; Létourneau et al. 2004). This method has the advantage of being more comprehensive than the composite dose method, meaning that errors may be more readily traced to their cause. Historically, it has also been easier and quicker to perform this kind of QA when using an array setup. A disadvantage of this method is that the gantry is not rotated during the treatment delivery; every field is delivered from a single gantry angle. This removes effects that will be present during

treatment such as gantry sag and couch attenuation. Also, the argument can be made that the composite dose distribution is what actually matters, and errors in a single field are less important as long as the full dose distribution is accurate. Finally, it has recently been shown that the field-by-field method can mask important dosimetric errors (Kruse 2010), and that it may not be predictive of clinically relevant dosimetric errors (Nelms, Zhen, and Tome 2011).

1.2.1 IMRT Point Dose Analysis

For absolute point dosimetry, the QA comparison is relatively simple. The percent difference between calculated and measured doses is determined, and the QA passes if the difference is within some predetermined threshold (3%, for example).

1.2.2 IMRT Planar Analysis

The QA performed on planar measurements is more complicated than for a single point dose. One method that can be used is to overlay a measured isodose distribution on top of a calculated distribution and visually inspect the agreement. This method gives qualitative information on the agreement between the calculated and measured distributions.

A more quantitative method of planar analysis is to simply consider the planar dose as a collection of point doses and find the percent difference between the calculated and measured distribution at every point. The percentage of points passing a predetermined criterion (3%, for example) is reported. This method has the advantage of being straightforward and easy to perform. However, it is generally reliable only in regions where the dose gradient is low. Figure 1.6 shows a profile of such an analysis between artificial measured and calculated distributions. The measured distribution is shifted 1.5 mm to the left and the dose is reduced by 1.5%. A very small spatial error leads to a disproportionately large percent difference in high gradient regions.

In high gradient regions, the percent difference metric can be discarded in favor of the distance to agreement (DTA) metric (see Fig. 1.7). For every dose point in some distribution A, the surrounding area in distribution B is searched for a point of matching

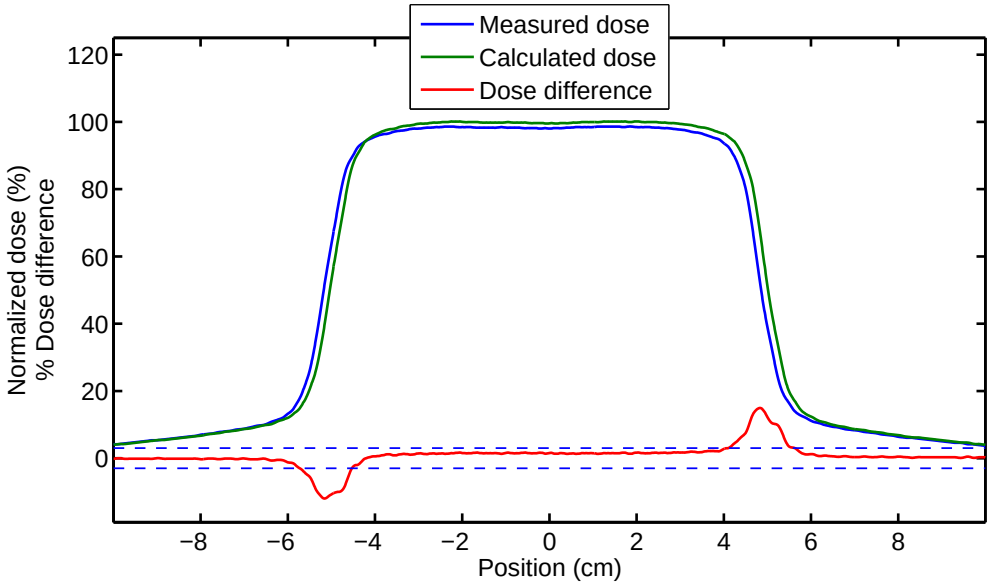

Figure 1.6: Sample percent dose difference profile comparison. The measured and calculated doses are shown, along with the percent dose difference. The measured profile is shifted 1.5 mm to the left and the dose is reduced by 1.5%. A ±3% dose difference pass/fail criteria is also shown as the blue dotted lines. A small spatial error leads to a large percent dose difference in high gradient regions.

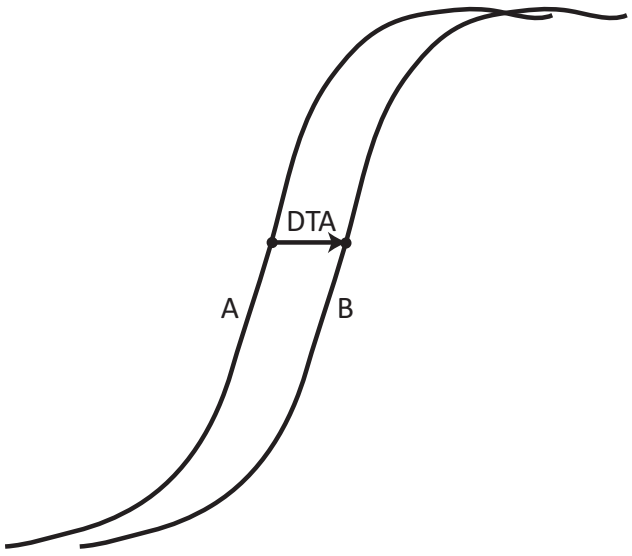

Figure 1.7: The distance to agreement method. For each point in some distribution A, the surrounding region in distribution B is searched for points of matching dose. The distance to the closest such point is the distance to agreement.

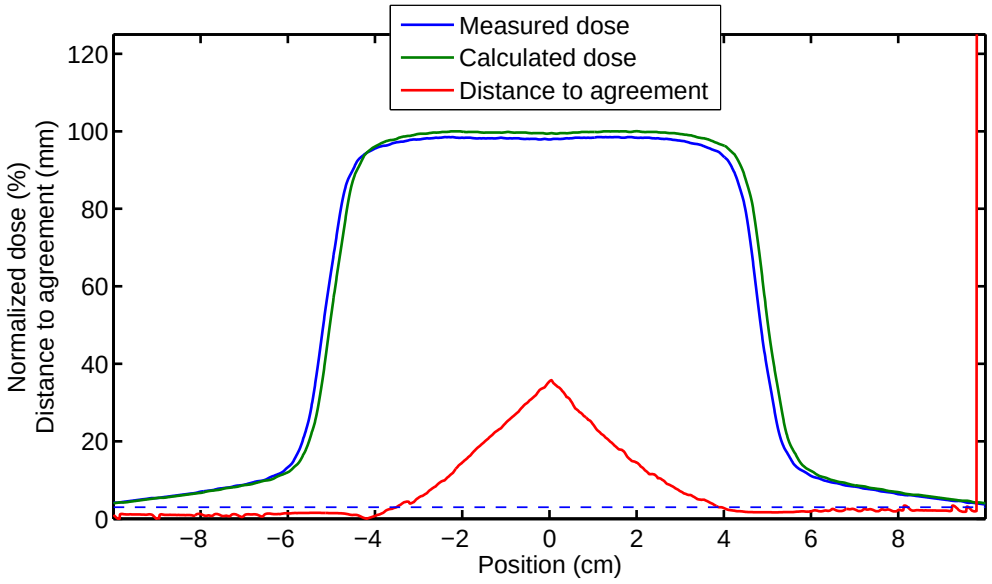

Figure 1.8: Sample DTA profile comparison. The measured and calculated doses are shown, along with the DTA. Here, the entire profile was searched for a matching dose, but in typical practice, only a small area around each point is searched. The measured profile is shifted 1.5 mm to the left and the dose is reduced by 1.5%. A 3 mm pass/fail criteria is also shown as the blue dotted line. A small dose difference can lead to a large DTA in low gradient regions.

dose. The distance from the point of interest to the closest point of matching dose is called the DTA. Like the percent difference metric, the percentage of points passing a predetermined criterion (3 mm, for example) can be reported. This metric is well suited for regions of high gradient, but poorly suited for regions of low gradient (see Fig. 1.8). A composite of the DTA and percent difference metrics can be used to give a more robust method of analysis of planar dose distributions.

One method of combining the two metrics was discussed by Harms et al. (1998). In this method, both the DTA and percent difference analyses are performed on a distribution. Any point that passes either metric is considered a passing point, and the percent of points passing is reported. Figure 1.9 illustrates how this composite method produces a binary pass/fail result for any given point.

Low et al. (1998) suggested that such a metric is limited by its pass/fail nature. A binary distribution does not lend itself well to display; therefore, the quantity displayed

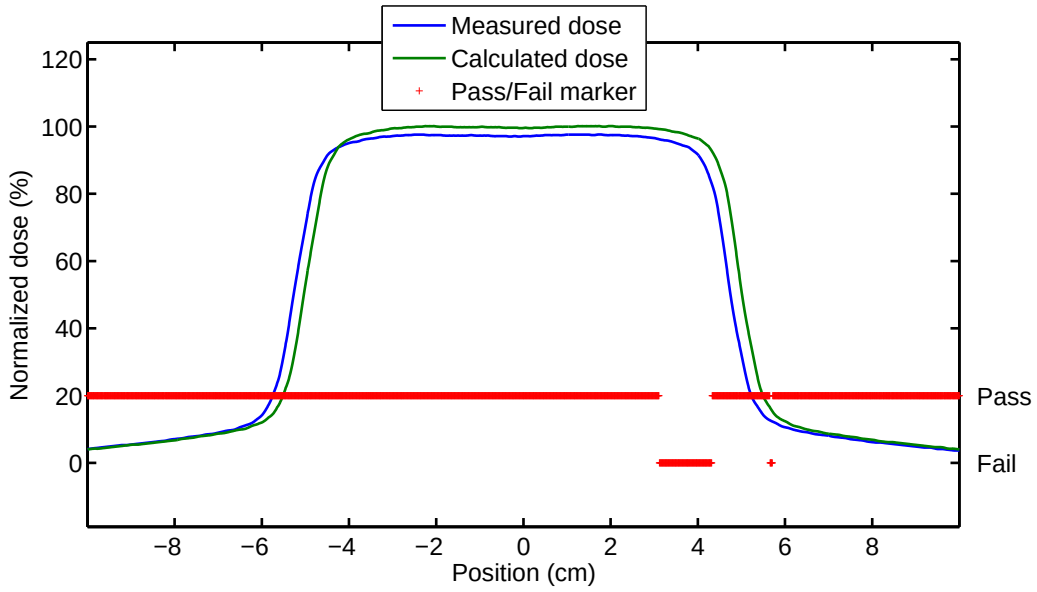

Figure 1.9: Sample binary DTA and dose difference composite comparison. The measured profile has been shifted 2.5 mm to the left and the dose has been reduced by 2.5%. Passing criteria are 3%/3 mm. Points where either the dose difference or DTA pass their respective criteria are considered to pass the composite test.

is typically the dose difference. This yields a display that may show large disagreement in high gradient regions. Also, a numerical metric may have more utility. For example, consider the case shown in Fig. 1.10 of two different distribution pairs, each having 100% of points passing the binary test described above. In the example shown, the criteria for passing are 3% and 3 mm. In one case, all the points match up exactly. In the other, the measured profile is shifted by 2.5 mm in one direction. The binary pass/fail test does not detect this shift that, while still within the tolerance of the test, appears to indicate that something is amiss in the second comparison.

Gamma Analysis

To overcome the potential problems with the binary test, a numerical method called "gamma analysis" was put forth by Low et al. (1998) (see also Low and Dempsey (2003)). Consider two dose distributions, a reference distribution and an evaluated distribution.

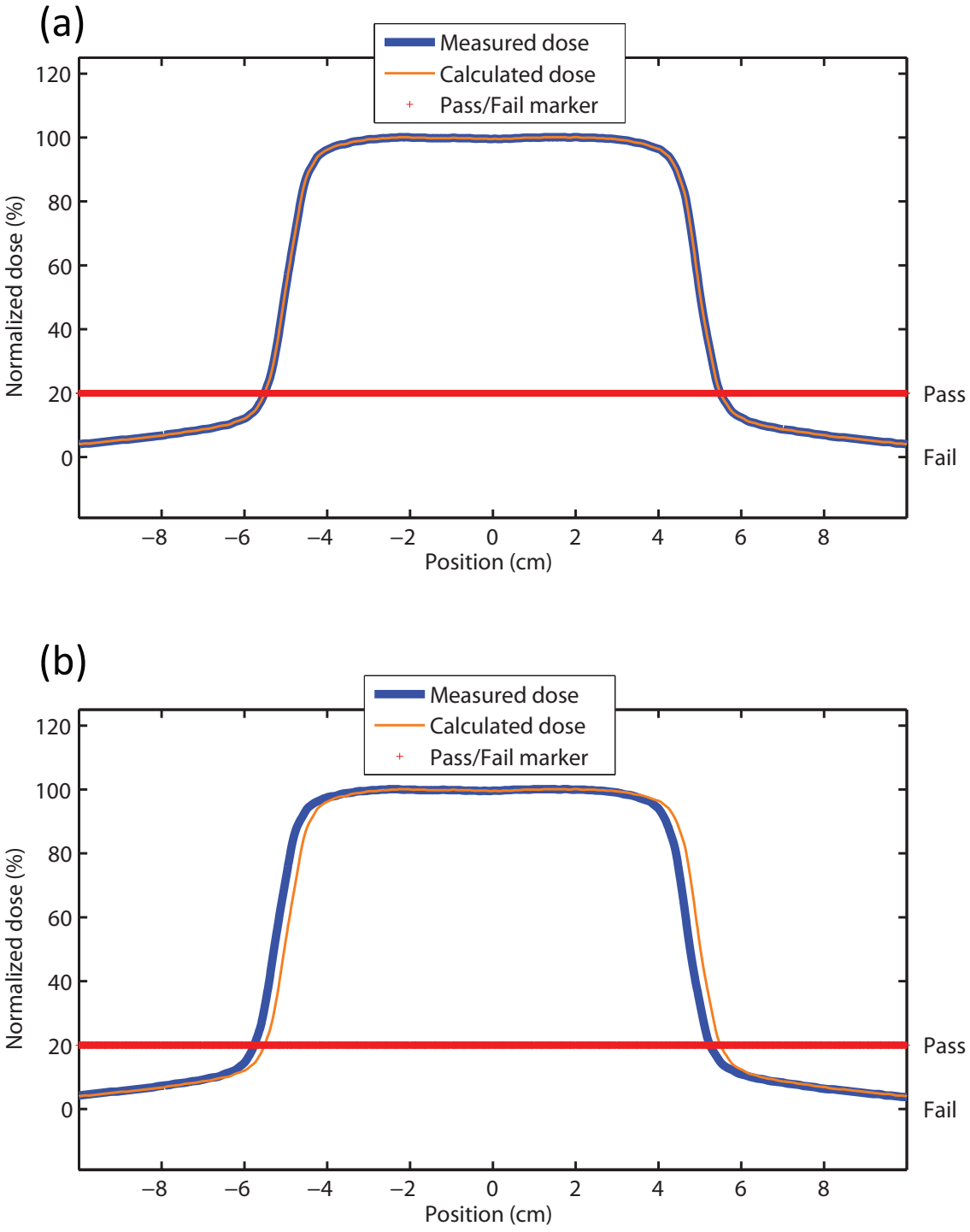

Figure 1.10: Two sets of profiles with 100% of points passing the binary composite test. The criteria used for the test are 3%/3 mm. In (a), the two profiles line up exactly, while in (b), the measured profile is shifted 2.5 mm to the left.

Gamma at every point in the reference is given by the equation

$$\gamma(\mathbf{r}_r) = \min\{\Gamma(\mathbf{r}_r, \mathbf{r}_e)\} \forall \{\mathbf{r}_e\} \tag{1.1}$$

where

$$\Gamma(\mathbf{r}_r, \mathbf{r}_e) = \sqrt{\frac{r^2(\mathbf{r}_r, \mathbf{r}_e)}{\Delta d_M^2} + \frac{\delta^2(\mathbf{r}_r, \mathbf{r}_e)}{\Delta D_M^2}}. \tag{1.2}$$

Here, the terms $\mathbf{r}_r$ and $\mathbf{r}_e$ are the reference and evaluated points, respectively. The terms Δd_M^2 and ΔD_M^2 are the DTA and dose difference criteria, respectively. The terms

$$r(\mathbf{r}_r, \mathbf{r}_e) = |\mathbf{r}_e - \mathbf{r}_r| \tag{1.3}$$

and

$$\delta(\mathbf{r}_r, \mathbf{r}_e) = D_e(\mathbf{r}_e) - D_r(\mathbf{r}_r) \tag{1.4}$$

are, respectively, the distance and dose difference between the reference and evaluated points. The symbols $D_r(\mathbf{r}_r)$ and $D_e(\mathbf{r}_e)$ denote, respectively, the reference and evaluated doses at the points $\mathbf{r}_r$ and $\mathbf{r}_e$. Considering a single point in the reference distribution, Γ is found for each point in the evaluated distribution (although in practice only a small region around each point needs to be calculated). The smallest of these values becomes the γ at that reference point. This is done for each reference point.

Like the binary pass/fail method, the gamma method uses a set of criteria for testing (3%/3 mm, for example). A point is said to pass gamma if the gamma value at the point is less than one. Figure 1.11 is a profile showing the results of a gamma test on the same profiles as shown in Fig. 1.9. Also shown are the percent difference and DTA analyses. Note that the area where both the DTA and percent difference tests fail corresponds to the area where gamma is greater than one. Gamma analysis has been shown to be a suitable quantitative method of determining the level of agreement between two dose distributions (Low and Dempsey 2003; Stock, Kroupa, and Georg 2005).

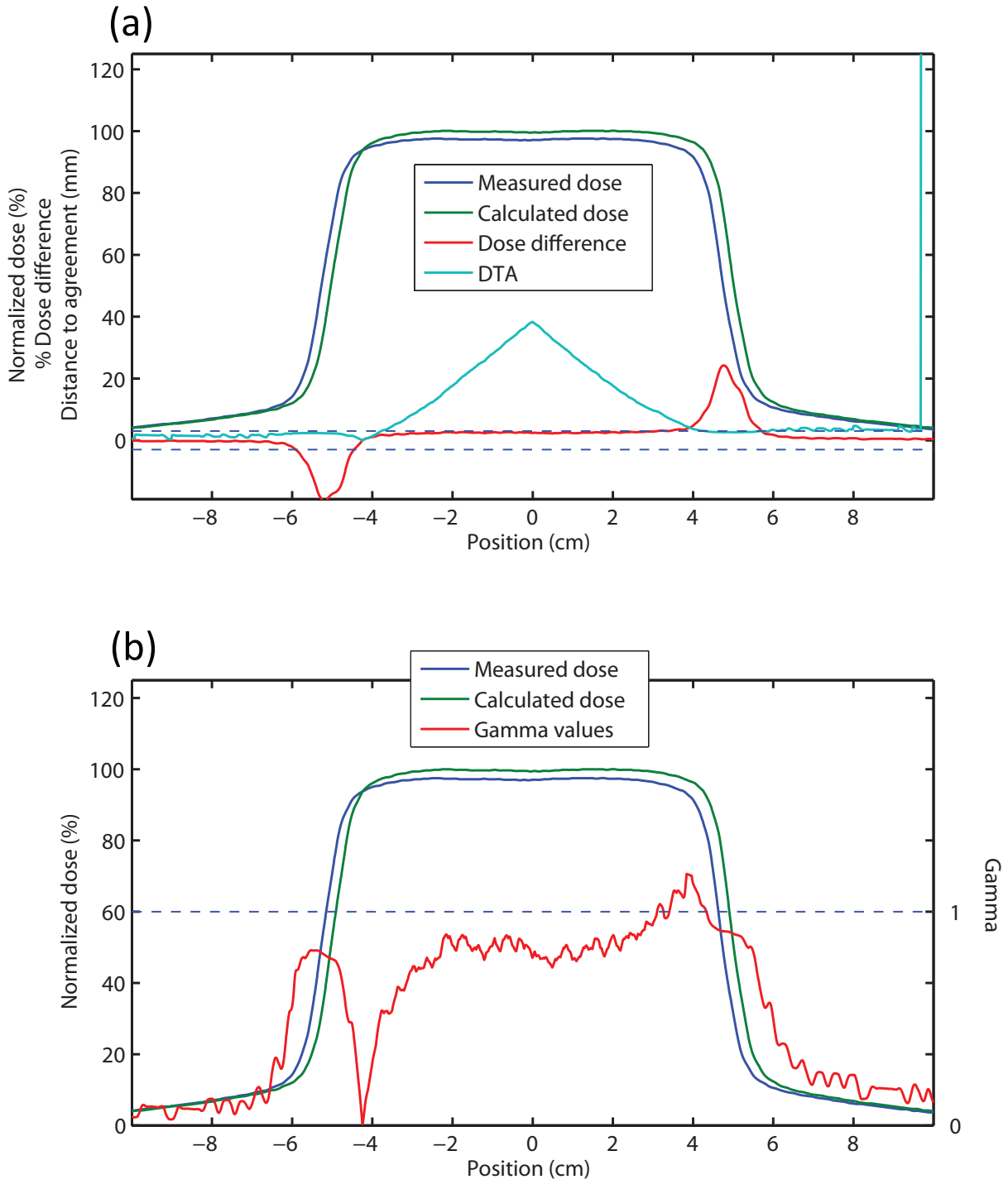

Figure 1.11: Sample gamma analysis. The profiles are shown in (a), along with the dose difference and DTA analyses for reference. Plot (b) shows the profiles again, along with gamma for each point. The criteria used for the gamma test were 3%/3 mm.

1.2.3 AAPM Task Group 119

An important issue in any QA process is to determine a tolerance or action level. When a QA result falls outside of this tolerance, some appropriate action is taken. During the gradual development of IMRT patient specific QA, institutions generally determined their own action levels based on their results. However, institutions had limited access to patient specific QA results from other institutions to serve as a reference. To address this issue, the American Association of Physicists in Medicine (AAPM) commissioned a task group (TG) to gather data on QA results from several institutions performing IMRT QA. The results were published as a report from AAPM TG 119 (Ezzell et al. 2009).

Each institution involved in TG 119 was given a common set of geometries for which IMRT treatments were planned and on which QA was performed. (See Sec. 2.1 for more information on the geometries.) For each treatment plan, point dose and planar film measurements were taken for the full treatment plan. Also, field-by-field measurements were taken, with most institutions using a 2D diode array. Point doses were analyzed using the following formula:

$$\%_{diff} = \frac{D_{measured} - D_{calc}}{D_{prescrip}} \times 100\%. \tag{1.5}$$

$D_{measured}$, D_{calc}, and $D_{prescrip}$ are the measured, calculated, and prescribed doses, respectively. Gamma was calculated for the planar measurements using criteria of 3%/3 mm. The means and standard deviations of the results from TG 119 are shown in Table 1.1.

These structures give a sampling of typical IMRT treatments. As such, the results from planning and performing QA on these structure sets can be generalized to draw conclusions about a large number of individual treatment plans. Institutions can also use these common geometries to perform their own tests and compare the results to those obtained in the TG report. For this reason, the structure sets from TG 119 were chosen for use in the present work.

Table 1.1: TG 119 results. Shown are the means and standard deviations of the four different types of QA tests performed by the institutions involved in TG 119.

Test	Metric	Mean	Standard deviation
High dose point	Percent difference	−0.2%	2.2%
Low dose point	Percent difference	0.3%	2.2%
Composite film	Percent passing gamma (3%/3 mm criteria)	96.3%	4.4%
Field-by-field	Percent passing gamma (3%/3 mm criteria)	97.9%	2.5%

1.3 Motivation for Research

Because VMAT is a form of IMRT, clinics that have been using VMAT have been performing patient specific QA on VMAT plans prior to delivery (Rao et al. 2010; Schreibmann et al. 2009). Due to the rotational nature of VMAT treatment, it is not practical to perform field-by-field QA on VMAT treatments. Therefore, the composite delivery method is typically employed, using either film and ion chamber or 2D or 3D array of diodes (Bedford et al. 2009; Jursinic, Sharma, and Reuter 2010; Korreman, Medin, and Kjaer-Kristoffersen 2009; Masi et al. 2011).

Those performing VMAT QA are typically using QA methods and action levels taken from fixed-beam IMRT QA methods. Despite this, there has not yet been a study comparing the results of such QA. As such, it is not yet clear that it is appropriate to apply fixed-beam IMRT QA methods and action levels to VMAT QA. This study aimed to perform such a comparison by systematically planning and performing QA on treatments using both the fixed-beam IMRT and VMAT modalities, then analyzing the results.

1.4 Hypothesis and Specific Aims

Our hypothesis was that the results of VMAT and fixed-beam IMRT QA are not significantly different. This hypothesis was tested using the following specific aims:

1.4.1 Specific Aim 1: Develop IMRT and VMAT Plans for TG 119 Structures That Meet Specified Dose Objectives

The TG 119 report provided four structure set geometries: a multitarget geometry, a mock prostate geometry, a mock head and neck geometry, and a C-shape geometry. Using a commercial treatment planning system, VMAT and fixed-beam IMRT plans were constructed that either (a) met dose objectives specified in TG 119 or (b) fell within one standard deviation of the results reported by institutions participating in TG 119.

1.4.2 Specific Aim 2: Deliver Planned Treatments to a Cylindrical Phantom and to a 2D Diode Array

For each test structure, VMAT and fixed-beam IMRT treatment plans were delivered to a cylindrical water-equivalent phantom. Absolute dose measurements were made at low and high dose points using a calibrated ion chamber. Planar dose measurements were made in the phantom in the sagittal and coronal planes using film. The plans were also delivered to a 2D diode array.

1.4.3 Specific Aim 3: Analyze the Collected Data and Test for Significance

The collected data was analyzed using the same methods as in TG 119. The film and diode array measurements were compared to calculated planar doses using gamma analysis with criteria of 3%/3 mm. Point dose data was analyzed using the percent difference between the measured and predicted value. For each QA method and modality, the results were averaged and tested for significance.

Chapter 2

Methods and Materials

2.1 Experimental Geometry

The institutions participating in AAPM TG 119 were provided a set of four geometrically distinct structure sets (see Fig. 2.1); these structure sets were used for this work. These structure sets contained both avoidance and target structures. Each institution constructed IMRT treatment plans for each of these structure sets in accordance with pre-specified dose objectives. The structure sets are described below.

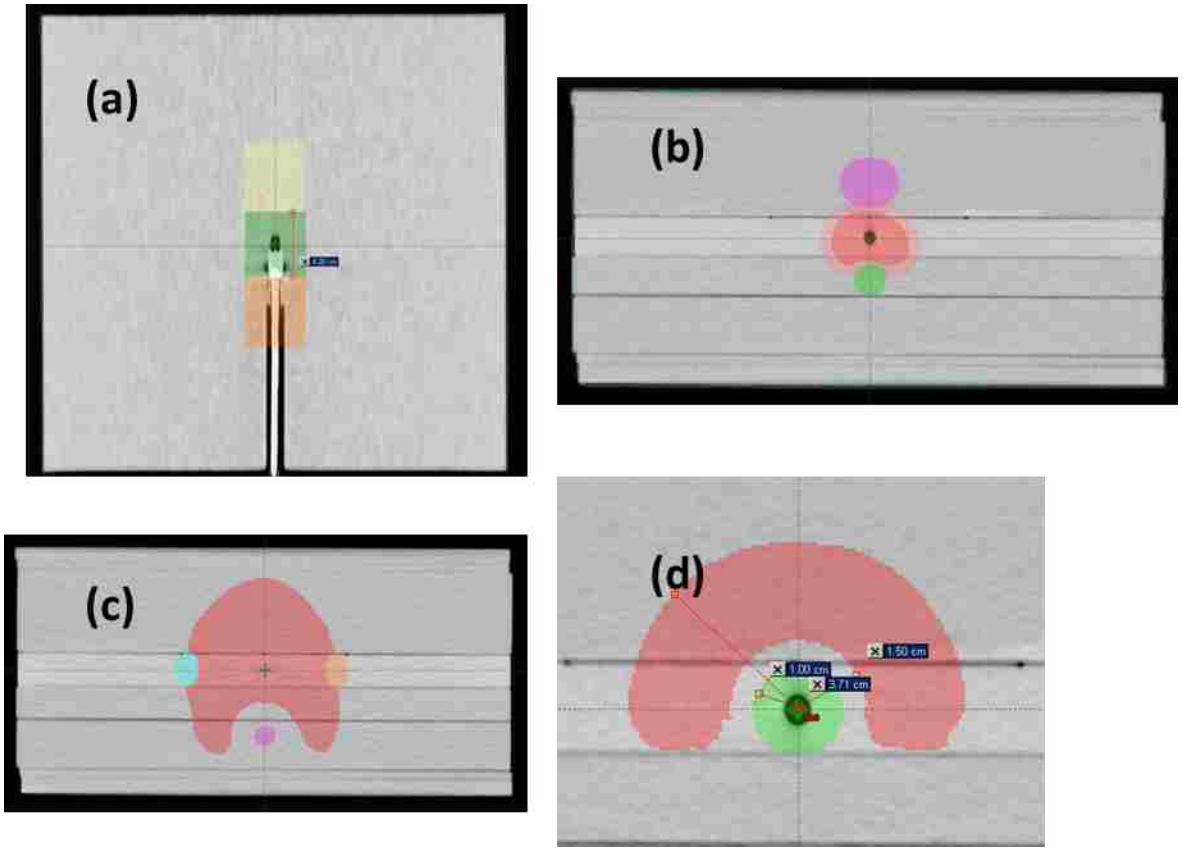

Figure 2.1: The four structure sets given to the AAPM 119 institutions included (a) a multitarget geometry, (b) a mock prostate geometry, (c) a mock head and neck geometry, and (d) a C-shape geometry.

Figure 2.1(a) shows the multitarget geometry, which consists of three abutting cylindrical targets, each with a length of 4 cm and a diameter of 4 cm. Each of these targets has a different dose objective. Figure 2.1(b) shows the mock prostate geometry. The prostate is approximately ellipsoidal and is $4.0 \times 2.6 \times 6.5$ cm^3 in the right-left (RL), anterior-posterior (AP), and superior-inferior (SI) dimensions, respectively. The PTV is defined as a uniform expansion of 0.6 cm around the prostate. The rectum is a cylinder of diameter 1.5 cm, and the bladder is $5.0 \times 4.0 \times 5.0$ cm^3 in the RL, AP, and SI dimensions, respectively. Figure 2.1(c) shows the mock head and neck geometry, which consists of a large central PTV with parotid glands on either side and a spinal cord. The gap between the PTV and the spinal cord is 1.5 cm. Finally, Fig. 2.1(d) shows the C-shape geometry, which consists of only two structures, an outer target with an outer radius of 3.7 cm, and a central OAR with a 1 cm radius. The gap between the two structures is 0.5 cm.

A set of dose objectives or goals for each geometry was provided to the institutions participating in TG 119 (see Table 2.1). With one exception, the dose objectives consist of a minimum or maximum dose to be received by a specified fraction of a structure. For example, one of the dose objectives for the prostate PTV was $D_{95} > 7560$ cGy. This means that 95% of the prostate PTV should receive at least 7560 cGy. (The lone exception is the maximum dose objective given for the spinal cord in the head and neck structure set.) In addition to the dose objectives shown, a more difficult version of the C-shape plan was also constructed by the TG 119 institutions that had a lower dose goal for the central core. This version was not used in this work.

Many of these objectives were achievable by some or all of the institutions. However, some dose goals were difficult to meet, most notably the high dose PTV in the multitarget geometry. For that geometry, the mean values of both dose parameters failed to meet the specified dose objectives.

Table 2.1: Dose goals for the TG 119 structures. The means and standard deviations of the planning results of the institutions involved in TG 119 are also reported.

Planning parameter	Plan goal (cGy)	Mean (cGy)	Standard deviation (cGy)	Coefficient of variation
Multitarget				
Central target D_{99}	>5000	4955	162	0.033
Central target D_{10}	<5300	5455	173	0.032
Superior target D_{99}	>2500	2516	85	0.034
Superior target D_{10}	<3500	3412	304	0.089
Inferior target D_{99}	>1250	1407	185	0.132
Inferior target D_{10}	<2500	2418	272	0.112
Prostate				
Prostate D_{95}	>7560	7566	21	0.003
Prostate D_5	<8300	8143	156	0.019
Rectum D_{30}	<7000	6536	297	0.045
Rectum D_{10}	<7500	7303	150	0.020
Bladder D_{30}	<7000	4394	878	0.200
Bladder D_{10}	<7500	6269	815	0.130
Head and neck				
PTV D_{90}	5000	5028	58	0.013
PTV D_{99}	>4650	4704	52	0.011
PTV D_{20}	<5500	5299	93	0.018
Cord maximum	<4000	3741	250	0.067
Parotid D_{50}	<2000	1798	184	0.102
C-shape				
PTV D_{95}	5000	5010	17	0.003
PTV D_{10}	<5500	5440	52	0.010
Core D_{10}	<2500	2200	314	0.141

2.2 Treatment Planning

2.2.1 Objectives

The first specific aim of this work was to develop IMRT and VMAT plans for the TG 119 structure sets. The dose objectives provided in TG 119 were used as guidelines in the treatment planning process in order to create plans that had complexity and modulation similar to the TG 119 institutions' plans. As previously stated, however, some of the dose goals were difficult for various institutions to meet. It was thus deemed sufficient to either meet the dose objectives specified in TG 119 or to fall within one standard deviation of the mean results achieved by the TG 119 institutions. This ensured that the plans created in this work achieved modulation similar to the plans constructed by the TG 119 institutions.

2.2.2 Planning Overview

The four structure sets and an accompanying CT image set were downloaded as DICOM files from the AAPM website. These were imported into the Pinnacle^3 treatment planning system (Philips, Fitchburg, WI). A new patient was created in a research institution, and the CT image set was added to the patient. A plan was created with the TG 119 CT set as the primary image set using version 9.0 of the Pinnacle^3 software. This plan was opened, and the four structure sets were imported using the Import DICOM option. The plan was exited and copied four times onto the CT image set of a cylindrical solid water phantom using the QA Tools option. Each of these plans was named for one of the structure sets. Each was then opened and all of the structures not corresponding to the plan's structure set were deleted, leaving only the structure set for which the particular plan was named.

The cylindrical phantom was used for the planar and point dose measurement portions of this work (see Sec. 2.3.1 for more information on the cylindrical phantom). The cylindrical phantom CT set contains a phantom boundary contour, inside of which the density is overridden to 1.014 g/cm^3, as this was the average density measured in the phantom. A slice of the CT image is shown in Fig. 2.2. The head and neck structure set has been imported and can be seen in the image.

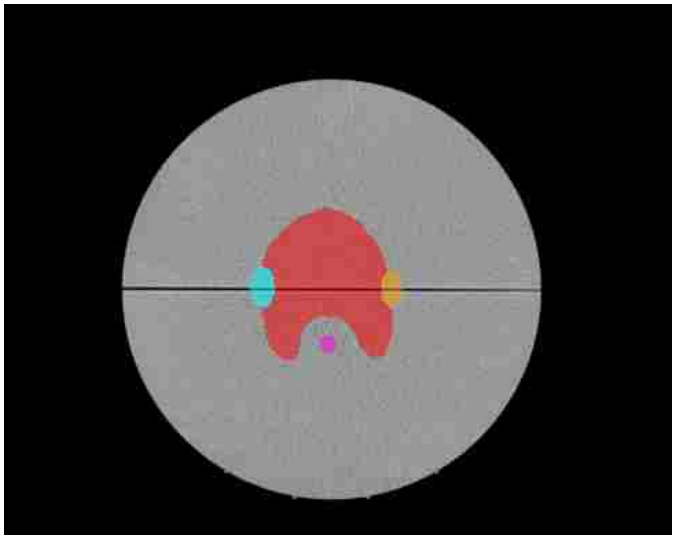

Figure 2.2: CT image of a slice of the cylindrical phantom. The head and neck structure set has been imported onto the CT data set. Shown are the red PTV, the right and left parotids in light blue and orange, and the cord in pink.

The treatments were planned directly on this phantom scan. All treatment planning was performed using version 9.0 of the Pinnacle[3] software. Both a fixed-beam IMRT treatment and a VMAT treatment were planned for each of the four geometries. The general method of planning is described below.

2.2.3 Initial Setup

When each plan was first opened, the CT couch was removed from calculation using Pinnacle[3]'s Remove Couch tool. A dose grid was drawn to encompass the entire phantom. A calculation point was placed inside the primary target to be used for plan renormalization. Finally, a prescription was created for the calculation point, and the per-fraction dose and the number of fractions were set to meet the prescription implied by the TG 119 dose objectives.

Beams from the Elekta Infinity were placed onto the phantom using the machine BR1 Elekta (commission date: 23 April 2010 at 10:02 AM), with their isocenters located at the center of the phantom. For both IMRT and VMAT treatments, 6 MV beams were used. Table 2.2 lists the beam arrangements for each of the four geometries. For the IMRT plans, step-and-shoot beams were added, using the number of beams specified in TG 119. An

Table 2.2: Beam setup overview for each plan. The number and arrangement of the IMRT beams followed the direction in TG 119, while for VMAT the number of arcs was determined by how easy or difficult it was to meet the dose goals with one arc.

	Number of beams/arcs	Beam arrangement	Collimator angle
IMRT			
Multitarget	7	50° from anterior	90°
Prostate	7	50° from anterior	0°
Head and neck	9	40° from anterior	0°
C-Shape	9	40° from anterior	0°
VMAT			
Multitarget	1	CCW 175° → 185°	45°
Prostate	1	CCW 175° → 185°	45°
Head and neck	2	CCW 175° → 185°, CW 185° → 175°	15°
C-Shape	2	CCW 175° → 185°, CW 185° → 175°	0°

anterior beam was always present, and the remaining beams were distributed relatively evenly around the arc. The collimator was originally set to 0° for all of the IMRT plans, but was rotated as needed to better achieve the dose objectives. For VMAT plans, dynamic arc beams were used. One beam with the gantry traveling counterclockwise from 175° to 185° was used initially; if this was found to be insufficient for meeting the plan goals, a second beam traveling clockwise from 185° to 175° was added. A 45° collimator angle is often used for VMAT (Otto 2009; Verbakel et al. 2009); the collimator was thus originally set at 45°. As with the IMRT plans, the collimator was rotated as needed to better achieve the dose goals.

2.2.4 General Optimization

IMRT plans were optimized using direct machine parameter optimization (DMPO). The settings used for the IMRT plans are summarized in Table 2.3. These parameters were chosen based on clinical practice at Mary Bird Perkins Cancer Center (MBPCC). The maximum number of iterations was set, but optimization was stopped periodically to make changes. Thus more or less iterations were executed as needed.

Table 2.3: Optimization settings for IMRT plans. Plans were optimized using DMPO. Exceptions to these settings are listed as footnotes.

Setting	Value
Max iterations	45[a]
Convolution dose iteration	15[b]
Stopping tolerance	1e−05[c]
Apply tumor overlap function	Unchecked
Allow jaw motion	Checked
Split if necessary	Unchecked
Max number of segments	90[d]
Min segment area	2 cm^2 [e]
Min segment MUs	2
Compute final dose	Checked
Use SVD for dose calculation	No
Min number of leaf pairs	2
Min leaf end separation	0.2 cm[f]
Min overlap distance	2 cm
Max overlap distance	4 cm

[a] Multitarget=50
[b] Multitarget=20
[c] Multitarget=1e−06
[d] Multitarget=50, Prostate=70
[e] Multitarget=4 cm^2
[f] Multitarget=1.5 cm

VMAT plans were optimized using the SmartArc option in Pinnacle^3, which also uses DMPO mechanics. The parameters used are summarized in Table 2.4. Again, the parameters were chosen based on clinical practice. VMAT plans sometimes take a large number of iterations to converge, so the optimization process was repeated as necessary, without resetting the beams. Thus the number of iterations was generally more than the maximum number given here.

The main objective in each plan was to get a uniform dose to the target volume. In general, this was achieved by using Pinnacle^3's region of interest (ROI) type "Uniform Dose" for the target volume objective. The target dose was set to the prescription dose for the structure. A weight of around 20 was given to the target ROI. In some cases, minimum or maximum dose or dose volume histogram (DVH) objectives were added if

Table 2.4: Optimization settings for VMAT plans. Plans were optimized using SmartArc. Exceptions to these settings are listed as footnotes. For plans with two arcs, the second arc traveled clockwise from 185° to 175°.

Setting	Value
Max iterations	70
Convolution dose iteration	20
Stopping tolerance	1e−05[a]
Apply tumor overlap function	Unchecked
Allow jaw motion	Checked
Final gantry spacing	4°
Max delivery time	90 sec[b]
Rotation direction	CCW
Start angle	175
Stop angle	185
Constrain leaf motion	0.4 cm/deg
Compute intermediate dose	Unchecked
Compute final dose	Checked
Fine resolution ODM	No

[a] Prostate=1e−06
[b] C-shape=100 sec

it was deemed necessary to push the system harder than simply using the uniform dose option alone.

Avoidance structures were typically optimized using the "Max DVH" type of ROI. This allowed shaping of the DVH to achieve the dose goals. Maximum DVH doses were generally set below the actual dose objectives to allow for renormalization of the plan. Weights were generally set to one, and increased as needed during the optimization process. In some cases a "normal tissue" ROI was added with a max dose of around half of the prescription dose, but in general little effort was put into reducing hot spots outside of the treatment area.

After the initial objectives were set, the optimization process was started. The plan was evaluated mainly using the dynamic DVH in Pinnacle[3] during optimization. Depending on how close the DVH appeared to achieve the dose goals, the optimization was either

Table 2.5: Optimization parameters for the multitarget plans

ROI	Objective type	Target cGy	% Volume	Weight
IMRT				
Central target	Uniform dose	5000		20
Central target	Max DVH	5200	10	5
Superior target	Min DVH	2600	99	1
Superior target	Max DVH	3100	10	5
Inferior target	Min DVH	1350	99	1
Inferior target	Max DVH	2100	10	5
VMAT				
Central target	Uniform dose	5000		10
Superior subvolume	Uniform dose	2500		1
Inferior subvolume	Uniform dose	1250		10
Central target	Min dose	5000		25
Superior target	Min dose	2500		25
Inferior target	Min dose	1250		50

allowed to finish or was paused for adjustments to the dose objectives. Specific techniques for achieving the dose goals for each structure set follow.

2.2.5 Plan Specific Optimization

Multitarget

The optimization objectives for the multitarget plans are shown in Table 2.5. For the IMRT plan, a uniform dose objective was created for the central target as well as a max DVH objective. The two abutting targets were given min DVH and max DVH objectives.

For the VMAT plan, the central target was given a uniform dose objective. However, the system struggled to meet the objectives on the other two targets using the same method as the IMRT plan. The technique employed here is one way to deal with secondary targets that abut the primary target. A subvolume was created for each of the secondary targets using the "ROI Expansion/Contraction" tool. This subvolume was separated from the primary target by 7 mm. It was then given a uniform dose objective in the optimization

Table 2.6: Optimization parameters for the prostate IMRT plan. The VMAT parameters were identical except that the smaller volume rectum weight was set to 40.

ROI	Objective type	Target cGy	% Volume	Weight
Prostate PTV	Uniform dose	7560		20
PTV ring	Max dose	7400		1
Rectum	Max DVH	6600	30	10
Rectum	Max DVH	7100	10	20
Urinary bladder	Max DVH	5000	30	1
Urinary bladder	Max DVH	6800	10	1
Unspecified tissue	Max dose	3750		1

window. All of the targets were given minimum dose objectives to help reduce the presence of soft shoulders in the DVH.

Prostate

The optimization parameters for the IMRT prostate plan are shown in Table 2.6. The VMAT parameters were identical to the IMRT parameters, except that the weight of the smaller volume rectum objective was changed to 40. The PTV ring structure was a 9 mm thick ring surrounding the PTV. Applying a "max dose" objective to this ring helped prevent hot spots in the rectum, and allowed the rectal goal to be achieved. An unspecified tissue structure was used to reduce hot spots outside of the treatment area.

Head and Neck

The parameters for the head and neck plans are shown in Table 2.7. The IMRT plan goals were met with relatively little difficulty in optimization and the parameters were fairly basic.

The VMAT plan required modifications of the initial objectives. A 1 cm ring was expanded around the PTV and was given a max dose objective. Subvolumes were created for the parotid glands, and rings were created around these subvolumes. These rings cut into the PTV, and a PTV subvolume called 50only2 was created that did not include the parotid rings. Finally an expanded cord contour was used to help lower dose to the cord.

Table 2.7: Optimization parameters for the head and neck plans

ROI	Objective type	Target cGy	% Volume	Weight
IMRT				
PTV	Uniform dose	5000		10
PTV	Min dose	5000		50
Cord	Max dose	3500		50
Left parotid	Max DVH	1500	50	25
Right parotid	Max DVH	1500	50	25
VMAT				
50only2	Max DVH	5400	5	50
50only2	Min DVH	5000	100	100
PTV	Min dose	5000		25
PTV ring	Max dose	5000		1
Cord	Max dose	3700		25
Cord + 5 mm	Max dose	3900		1
Left parotid sub	Max DVH	1500	50	25
Right parotid sub	Max DVH	1500	50	25
Parotid sub ring	Max dose	5100		1
Unspecified tissue	Max dose	3500		0.5

C-shape

The parameters for the C-shape plans are shown in Table 2.8. The IMRT plan employed an 8 mm PTV ring to provide an area for the dose to decrease between the PTV and the core. An unspecified tissue contour helped avoid hot spots outside of the treatment area. The VMAT plan included a minimum dose objective for the target to help reduce the soft shoulder. A 7 mm ring around the core was added to push the system further in reducing the core dose.

2.2.6 Evaluation of the Plan

When optimization was complete, the final dose was computed using the adaptive convolution algorithm. However, immediately following optimization, the plans generally required renormalization to meet the dose goals. A tabular DVH was used to quantitatively evaluate the dose parameters during normalization. An example of a tabular DVH is shown in Fig. 2.3. For every ROI, the volume receiving a given dose can be read off. This

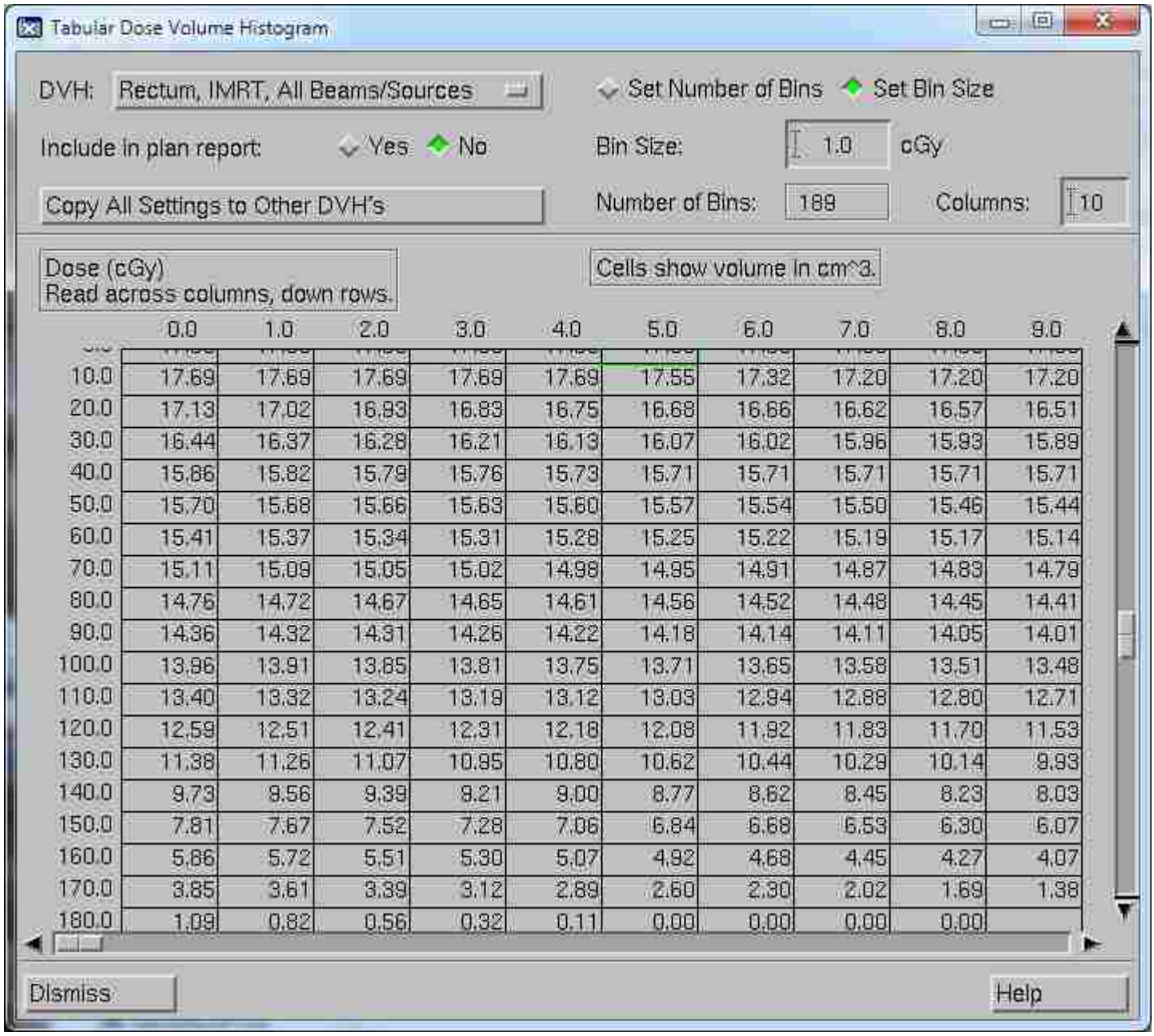

Figure 2.3: Tabular DVH example. The row and column headings are in cGy, and the cells are in cm^3.

Table 2.8: Optimization parameters for the C-shape plans

ROI	Objective type	Target cGy	% Volume	Weight
IMRT				
PTV	Uniform dose	5000		20
PTV ring	Max dose	4800		1
Core	Max DVH	2100	10	50
Unspecified tissue	Max dose	2500		0.5
VMAT				
PTV	Uniform dose	5000		20
PTV	Min dose	5000		20
Core	Max DVH	2000	10	20

information was used to determine the values of the parameters of interest. By adjusting the plan normalization in the prescription dose window (shown in Fig. 2.4), the plan was normalized until the primary target volume just achieved the dose goal. At that point, if any organs at risk did not achieve their dose goals, the plan was returned to the optimization process for further work.

2.2.7 Data Export

Point and Planar

Once all of the dose goals were met for a given plan, it was ready to be delivered. Both planar and point dose measurements were made, so planar dose and point dose calculations were extracted from Pinnacle[3].

For every plan, several calculated point doses were recorded. Table 2.9 lists the positions for each point dose calculation. These were chosen based on the recommended point dose measurements in TG 119. In general, a point dose was measured in each target and in at least one OAR. Locations of calculated point doses corresponded to the location of the center of the ion chamber inside the phantom (see Sec. 2.3.1 for more information on the phantom used).

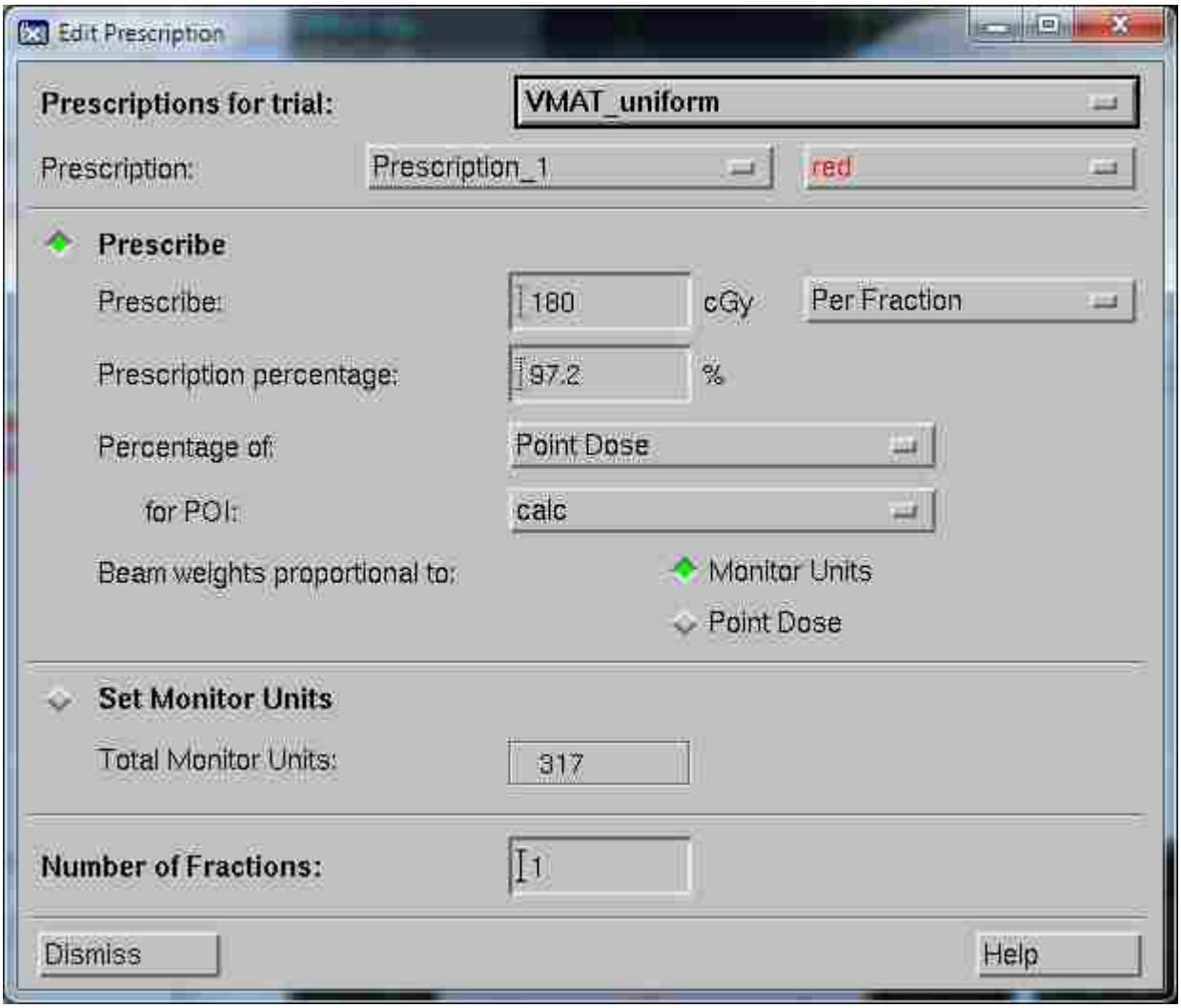

Figure 2.4: Prescription dose window. The normalization was adjusted to achieve the desired dose goal in the primary target.

Table 2.9: Point dose calculation and measurement locations

Geometry	Number of points	Point descriptions
Multitarget	3	One point located within each of the three targets
Prostate	3	One point located in the prostate PTV, one in the bladder, and one in the rectum
Head and neck	2	One point in the PTV, and one in the cord
C-Shape	2	One point in the PTV, and one in the central core

Table 2.10: Settings used for exporting planar dose files

Setting	Value
Medium	Primary data
SPD	100 cm
Beams	Sample trial
Resolution	0.1 cm
X Dimension	230
Y Dimension	230
Format	ASCII

Before extracting the calculated doses, the prescription was reduced to a single fraction, as only a single fraction was delivered for each measurement. For each plan, the calculated doses were recorded from Pinnacle^3's "Point Of Interest dose" table.

Planar doses in Pinnacle^3 were calculated using a separate beam. For each plan, two static beams were added with the center of the phantom at isocenter. One beam was placed at 0° for a coronal plane and one at 90° for a sagittal (note that the Elekta defines 0° as a top down beam). They were given 20×20 cm^2 square fields, and zero monitor units. The beams were calculated prior to calculating the planar dose. The planar dose tool in Pinnacle^3 was used to create planar dose files, and the settings used are shown in Table 2.10. The planar dose files were exported from Pinnacle^3, then retrieved via FTP.

MapCHECK and MapPHAN

In addition to using a phantom for measurements, a 2D diode array was used (see Sec. 2.3.1). Planar dose files were also required for this device. To accomplish this, every plan was copied to a CT scan of the MapCHECK with MapPHAN combination. The same steps were followed to obtain a planar dose as described in the previous section, with a few exceptions. First, the number of monitor units was set to be the same as what was used for the original plan. This meant that the exact same treatment would be delivered to MapCHECK as to the cylindrical phantom. Also, only a coronal planar dose file was created for each geometry.

Figure 2.5: Elekta Infinity linear accelerator

MOSAIQ

The plans were exported from Pinnacle^3 and imported into MOSAIQ (Elekta AB, Stockholm, Sweden) for treatment delivery. The plans were exported from Pinnacle^3 using the "Export DICOM" tool. A research patient named "Mancuso, Thesis" was created in the MOSAIQ system with the same MR# as the patient in Pinnacle^3 (MR#: A101477). Then the treatments were imported into MOSAIQ using the "RTP Import" tool.

2.3 Experimental Measurements

For each planned geometry, several types of measurements were taken, using film, ion chamber, and a 2D diode array. Coronal and sagittal film planes were measured three times each, and each point dose was measured five times. Diode array measurements were also taken five times in the coronal plane for each geometry. This section details the materials and procedures used for each of the measurement methods.

2.3.1 Measurement Materials

The treatments were all delivered using an Elekta Infinity linear accelerator system (Elekta AB, Stockholm, Sweden) (see Fig. 2.5) located at MBPCC in Baton Rouge, Louisiana. The Infinity can deliver both fixed-beam IMRT and VMAT treatments. It includes on-board kV cone beam CT imaging and MV planar imaging. The particular unit used can deliver

Figure 2.6: Cylindrical "cheese" phantom

Figure 2.7: Cylindrical phantom separated into semicylinders

photon energies of 6, 10, and 15 MV, and electron energies of 7, 9, 10, 11, 13, 16, and 20 MeV. The nominal dose rates available are 500, 250, 125, 65, and 30 MU per minute.

The phantom used for planar film and point dose measurements was a cylindrical solid water phantom, or "cheese" phantom (Tomotherapy, Inc., Madison, WI), shown in Fig. 2.6. The cylinder has a radius of 15 cm and a height of 18 cm. The phantom splits in half to allow film placement between the two semicylinders (see Fig. 2.7). It is held in place on a

Figure 2.8: Exradin A1SL ion chamber

small stand that allows the phantom to be rotated about its central axis, thus allowing both sagittal and coronal film measurements. A linear series of holes extends along one face of the phantom. These holes are designed to hold an A1SL ion chamber. The holes are 1 cm apart, except for at the split where there is no hole. The hole directly below the split is 0.5 cm from the split, and the next hole is 1.5 cm below that (the intention being to allow point measurements as close as possible to the film plane). When not filled with an ion chamber, these holes are plugged with solid water.

Point dose measurements were acquired using a 0.057 cc Exradin A1SL ion chamber (Standard Imaging, Inc., Middleton, WI), shown in Fig. 2.8 (serial number 330320). The chamber was connected to a Keithley 614 electrometer (Keithley Instruments, Inc., Cleveland, OH) (see Fig. 2.9) for all data collection (serial number XW100989).

Planar dose measurements were made using film. Initially, radiographic EDR2 film was used (Eastman Kodak, Rochester, NY), but after numerous tests, it was determined that the available processor did not develop the film uniformly. Therefore, film measurements were made using radiochromic film, which requires no processor as it is self-developing. Gafchromic EBT2 film (International Specialty Products [ISP], Wayne, NJ, shown in Fig. 2.10) was tested and determined to be sufficient for the film measurements in this work. EBT2 film consists of a radiosensitive active layer sandwiched between two layers of polyester.

Figure 2.9: Keithley 614 electrometer

Figure 2.10: EBT2 film

The active layer darkens when exposed to radiation, and can be used to read doses up to 40 Gy when it is read using the green channel, although the typical range of measurements is 1 cGy–10 Gy. The yellow appearance of the film is due to a marker dye included in the active layer. This marker dye distinguishes EBT2 film from EBT film, and has two benefits. One, it allows measurements of the film response independent of thickness changes in the active layer, and two, it absorbs lower wavelength visible light, making EBT2 significantly less sensitive to ambient light than EBT film (Andrés et al. 2010; International Specialty Products 2009).

2D diode array measurements were taken using the MapCHECK with MapPHAN combination (Sun Nuclear, Melbourne, FL) (see Fig. 2.11). The MapCHECK is a 2D diode

Figure 2.11: MapCHECK device and MapPHAN phantom. The MapCHECK slides into the MapPHAN for rotational delivery measurements.

array with 445 diodes in a 22×22 cm^2 plane. The active detector area is 0.8×0.8 mm^2.The minimum diode spacing in the central 10×10 cm^2 region is 7.07 mm and in the outer region is 14.14 mm. The MapPHAN is a water equivalent case designed to house the MapCHECK for rotational delivery measurements. The MapCHECK device is connected to a computer during delivery, and the MapCHECK software records the data collected.

2.3.2 Point and Planar Dose Calibration

For point dose measurements, the ion chamber was calibrated for each measurement session. The calibration procedure recommended in TG 119 was used, and its description follows. In Pinnacle^3, a plan was made using 10×10 cm^2 parallel opposed AP:PA fields on the cylindrical phantom. A dose of 200 cGy was prescribed to the chamber location closest to the geometric center of the phantom. This plan was exported to MOSAIQ. With the phantom aligned (alignment procedure described in Sec. 2.3.3) and the chamber inserted into the phantom in the appropriate hole, the plan was delivered to the phantom, and

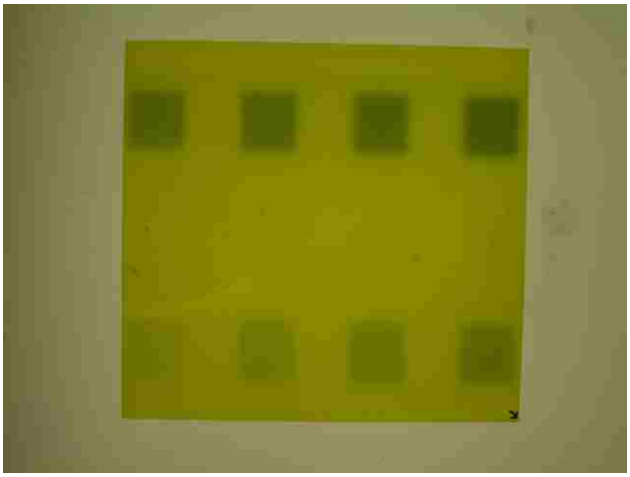

Figure 2.12: Calibration film with eight 3×3 cm^2 squares of varying doses

the electrometer reading was recorded. This gave a cGy/reading ratio, r. For subsequent measurements, r was used to obtain measured dose, D_m, using the equation

$$D_m = E_m \times r \ . \tag{2.1}$$

Here, E_m is the electrometer reading corresponding to the measurement m. This method was recommended in TG 119 to reduce the effect of daily linac output variations. For each dose calibration measurement, the ion chamber dose was also calculated using the $N_{D,w}$ of the chamber and the P_{elec} of the electrometer, with a temperature and pressure correction. In all measurement sessions, the dose calculated using the temperature/pressure correction was within 0.6% of the 200 cGy calculated dose to the chamber.

For each session of film data collection, a calibration film was irradiated following the procedure described by Childress, Dong, and Rosen (2002). A blank film was irradiated at isocenter in the portrait orientation with 5 cm backscatter and 10 cm buildup of solid water. The delivered calibration fields resulted in a series of eight dose squares of regularly spaced known doses, as shown in Fig. 2.12. The following doses (in cGy) were delivered to their respective squares: 35.6, 66.6, 97.5, 129.3, 161.8, 191.3, 222.2, 256.1. In addition, a point at the center of the calibration film had a measured dose of 5.4 cGy. These covered

the full range of doses used in this study. The calibration film was used along with a blank film to calibrate all the films from a session.

2.3.3 Point and Planar Dose Measurements

This section describes the methods of measuring the point and planar doses in the cheese phantom. The basic method of setting up the cheese phantom was very similar for both film and point dose measurements, and is described first. The collimator, gantry, and couch rotation were all set to 0° prior to alignment, and the treatment field was opened to make sure the light field crosshairs were visible. The phantom was placed on the treatment couch and aligned to the treatment room lasers such that the geometric center of the phantom coincided with the isocenter of the linear accelerator. The machined grid on the phantom was aligned to the light field crosshairs of the linear accelerator. With the phantom in the correct lateral and longitudinal position, the top semicylinder was carefully removed to expose the flat surface of the phantom. The optical distance indicator (ODI) was then used to bring the cylinder center to 100 cm SSD, thus bringing the phantom to the correct vertical position. The top semicylinder was then placed back into position.

For each point dose measurement, the following procedure was followed. The ion chamber was placed in the appropriate hole in the phantom for the current measurement. All point dose measurement locations were located along the vertical line on which the holes fell (except for two measurements in the multitarget structure set, which presented a unique challenge that is discussed below). The phantom was checked to ensure it was in the correct location, and the entire treatment was delivered. The electrometer reading was recorded after each delivery. In between repeated measurements at the same point, the treatment couch was perturbed and realigned to simulate inter-treatment positional variations that occur in clinical practice.

The multitarget structure set consists of three abutting cylindrical targets. TG 119 called for point dose measurements in each target. The targets are oriented in the superior-inferior direction, which is perpendicular to the chamber position line in the phantom. The ion

chamber could not be simply moved to a new hole for measurement; instead, the entire phantom had to be translated to place the chamber in the correct location. To compensate for the changed treatment setup, new plans were created in Pinnacle^3 that simulated the new setup. The beams were moved 4.3 cm either superior or inferior, depending on the target being measured, and the new chamber dose was recorded. During measurement, the couch was shifted the appropriate 4.3 cm after the initial alignment to place the chamber at the correct location.

It was noted after taking all of the multitarget point dose data that the phantom had been rotated 180° from its nominal orientation. As such, point dose measurement locations were displaced by 0.5 cm. To compensate for the measurement shift, the point doses were moved in Pinnacle^3 and dose was recalculated.

For film measurements, the following procedure was followed. With the phantom fully intact, the alignment with the light field was rechecked. The top semicylinder was removed from the phantom and set aside. A piece of EBT2 film, labeled with the name of the plan to be delivered, was placed on the phantom in landscape orientation. The film was taped to the phantom and the superior-left corner (from the patient's perspective) was marked with an arrow. The collimator was opened to an 18×18 cm^2 field. For registration purposes, the edges of the field were marked on the film using a fine tipped permanent marker, at the points where the crosshairs intersected the field edge (see Fig. 2.13). (The "field edge" is typically defined at the point where the light field fades completely to dark. However, on the Elekta Infinity used for this work, the lateral field edges are defined in the middle of the fading region. The longitudinal field edges are defined as normal.) The top semicylinder was carefully placed back into position, and the phantom was checked to make sure that its location had not been disturbed. If the film was a sagittal film, the phantom was then rotated 90° to place the film in the correct orientation.

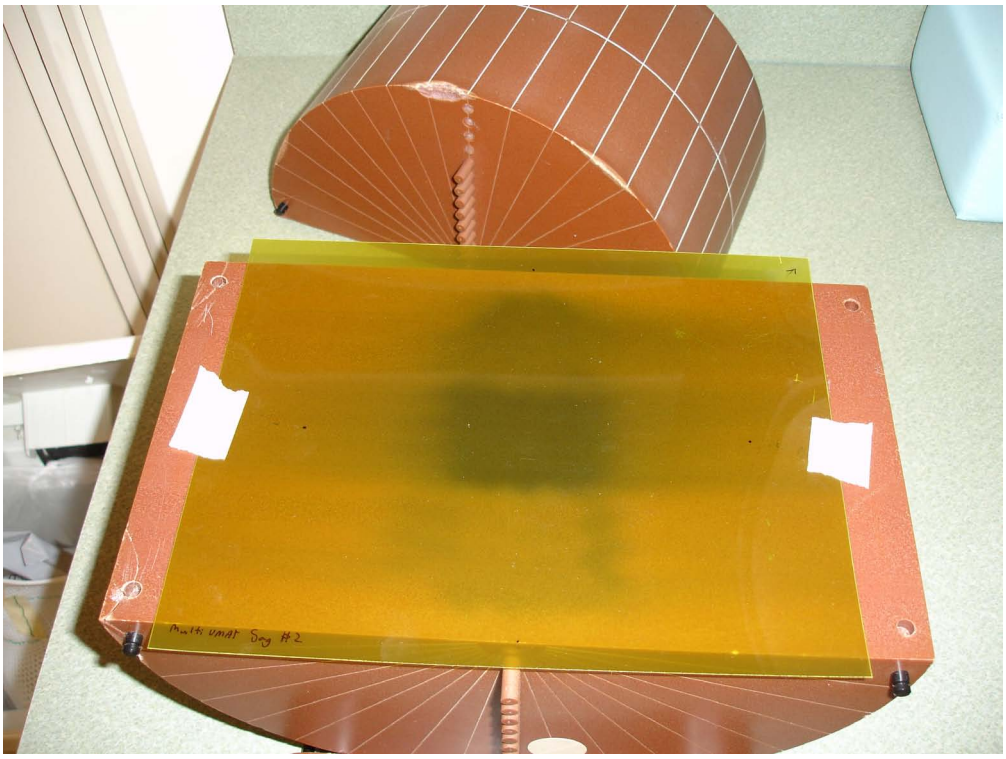

Figure 2.13: EBT2 film in place on the cylindrical phantom. An arrow marks the in-left position, and registration dots mark the edges of an 18×18 field.

The treatment plan was then delivered to the film-phantom setup. The film was removed and stored for later digitization, and the process was repeated for the next measurement.

The cheese phantom allows ion chamber and film measurements to be taken at the same time. The point dose measurements in the central PTVs of the multitarget, prostate, and head and neck geometries were performed with EDR2 film in place, as these point dose measurements were taken prior to the switch to EBT2 film. Three of the point dose measurements in the core of the C-shape geometry were taken with EBT2 film in place. The rest of the point dose measurements were taken without film in place.

2.3.4 MapCHECK Measurements

The MapCHECK device requires two calibration types. One is the dose calibration, which is performed before every MapCHECK session. The central diode is calibrated to a known dose, which minimizes the effect of daily linac output variation. The other

calibration is the array calibration, which determines the ratio of each diode's reading to the central diode reading. By combining this with the dose calibration, the dose at each diode can be calculated. This work used the array calibration used for clinical work at MBPCC.

The dose calibration was performed prior to measurements using the procedures of MBPCC. The MapCHECK, without the MapPHAN, was placed on the treatment couch and the light field crosshairs were aligned to the diode array. The electronics portion of the device was placed inferior to the diode array, away from the gantry. 3 cm of solid water was placed on top of the diode array portion of the device. The ODI was activated and the top of the solid water was set to 95 cm SSD. The MapCHECK has 2 cm of water equivalent buildup built in, so the radiological depth was 5 cm. The MapCHECK program was set to collect a calibration dose, and a 10×10 cm^2 field delivered 100 MU to the device. The dose delivered during the calibration was 95.4 cGy, which was entered into the MapCHECK program.

With the MapCHECK device and program calibrated, the system was ready to take measurements. The MapCHECK device was placed inside the MapPHAN phantom and placed on the treatment couch. The device was aligned in the following manner. The gantry crosshairs were aligned to the crosshairs on the top of the MapPHAN. To put the detector plane at isocenter, the ODI on the top of the MapPHAN was set to 95.7 cm, since the distance from the top surface to the detector plane is 4.3 cm. Only coronal measurements were acquired with the MapCHECK device.

For each diode array measurement, data collection was started in the MapCHECK software. The treatment was delivered, and the data collection was stopped. The measured dose was saved, and the process was repeated for the next plan. Array and dose calibrations were saved in the collected data file. Similar to the point dose data collection, the couch was perturbed in between consecutive deliveries of each plan.

2.4 Data Analysis

2.4.1 Point Dose Analysis

The measured point doses were compared to the point doses calculated in the treatment planning system. A simple percent difference calculation was used. Based on the recommendation in TG 119, this was calculated using the formula

$$\%_{diff} = \frac{D_{measured} - D_{calc}}{D_{prescrip}} \times 100\%. \tag{2.2}$$

$D_{measured}$, D_{calc}, and $D_{prescrip}$ are the measured, calculated, and prescribed doses, respectively. TG 119 recommends using the prescribed dose rather than the local predicted dose in the denominator to avoid overstating the differences in low dose areas.

2.4.2 Film Scanning

The EBT2 films were digitized using a 16-bit Vidar DosimetryPro Advantage scanner (Vidar Systems Corporation, Herndon, VA) (see Fig. 2.14). Film is transported past a line of detectors which capture the image. MBPCC owns both a white light scanner and a red scanner. An initial investigation of the red scanner revealed that it exhibited excessive nonuniformity (approximately a 10% variation in recorded light response) across a uniformly blank film, as shown in Fig. 2.15. By contrast, Fig. 2.16 shows the same film scanned on the white scanner, which showed an approximate 3% variation across the film. Therefore, the white scanner was chosen for this work.

Radiochromic film has been shown to respond differently depending on whether the film is scanned in the portrait or landscape orientation (Zeidan et al. 2006). According to ISP documents included with the film, EBT2 film also responds differently depending on the particular face of the film that is facing the scanner. The reason for this is that EBT2 film is not symmetrical; the polyester outer layers are of differing thicknesses depending on the face, as seen in the film cross section shown in Fig. 2.17. Because of these issues,

Figure 2.14: Vidar DosimetryPro Advantage scanner with white light source

care was taken to scan all films in a consistent manner. The procedure that was used is described below.

Each film has a small slit in one corner that identifies the orientation of the film. Each film was irradiated as described in Sec. 2.3.3, with the slit in the same corner as the arrow marking the in-left position. This placed the thinner polyester laminate facing up. Each film was scanned in landscape orientation, with the arrow in the upper left corner of the film during scanning. This kept the scanning orientation consistent. This particular orientation was chosen because the resulting scanned image was in the correct orientation with respect to the calculated planar dose from the treatment planning system, without requiring any rotating or reflection of the image.

To further suppress scanner nonuniformity using the white light Vidar scanner, film was placed in the center of the scanning area, rather than up against the built in film guide.

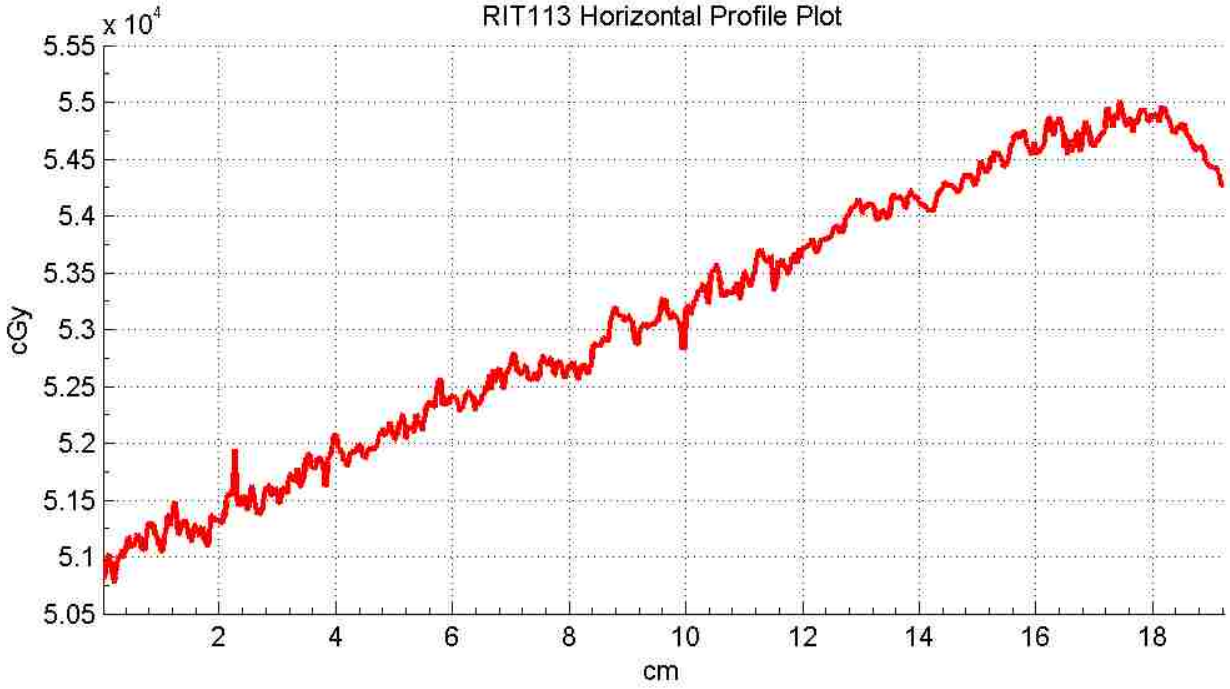

Figure 2.15: Horizontal profile of EBT2 film scanned on the red Vidar scanner. The y-axis is in pixel values (the cGy text notwithstanding), and the x-axis is in cm.

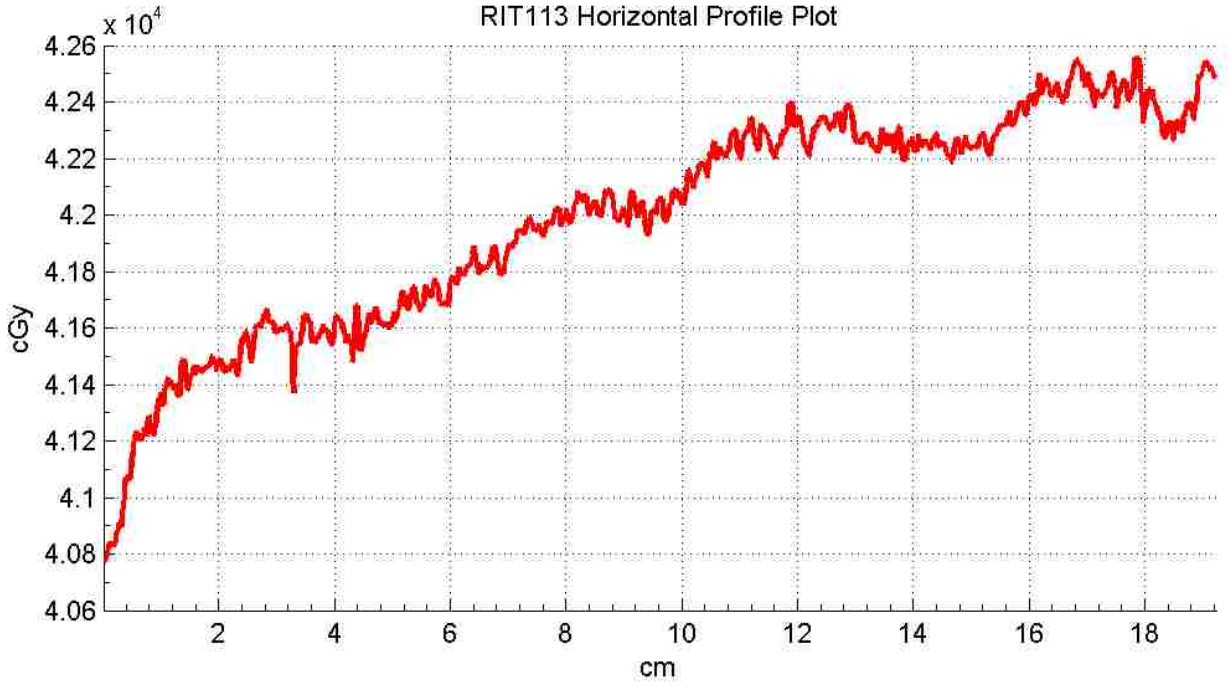

Figure 2.16: Horizontal profile of EBT2 film scanned on the white Vidar scanner. The y-axis is in pixel values (the cGy text notwithstanding), and the x-axis is in cm.

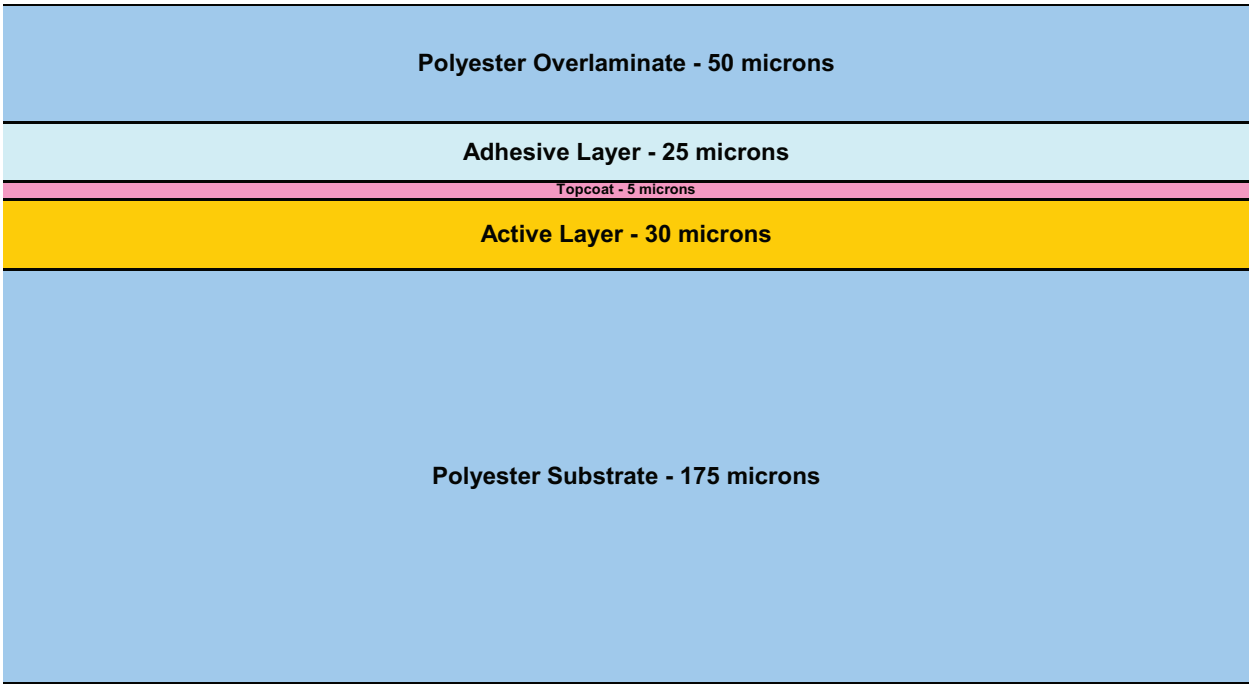

Figure 2.17: Cross section of EBT2 film. Image from International Specialty Products (2010).

A replacement film guide was constructed using a ruler affixed to the scanner to ensure that films were placed in the same location for each scan.

To further reduce the effect of scanner nonuniformity on the calibration films, they were scanned four times, once for each of the four rows of two dose squares. For each scan, the row being focused on was placed as close as possible to the center of the scanner, where the majority of the film data of interest was also located. This allowed each calibration row to be scanned by the same detectors and reduced the nonuniformity effect on the calibration films.

The Vidar scanner was controlled using version 5.2 of the RIT113 film analysis software (Radiological Imaging Technology, Inc., Colorado Springs, CO). Films were scanned at a resolution of 0.178 mm per pixel, and a 5×5 pixel median filter was applied to the data. The files were saved in a proprietary RIT format.

2.4.3 Film Analysis

Films were converted to dose, registered, and normalized using the RIT software. Gamma calculations were performed using in-house software.

Each film was converted from pixel value to dose using the calibration film from its measurement session. Using the scans of the calibration film and a blank film, a calibration file was created using the RIT "Perpendicular Dose Calibration" tool. This file consisted of 10 points of scanner response versus dose—eight from the calibration film squares, one from the center of the calibration, and one from the blank film. The calibration file used a piecewise polynomial interpolation.

Each film was opened as the reference image in the RIT software. The appropriate calibration file was applied and embedded into each film scan. Embedding simply added the calibration information to an ASCII header file associated with each film scan file; it did not change the original scanned data.

The film scan was moved to the target image spot in RIT, and the corresponding ASCII planar dose file from Pinnacle^3 was opened as the reference image. The registration tool was selected, and a saved registration was applied. The saved registration placed four registration points onto both the calculated and measured data fields. The points on the calculated image were defined to be at the points corresponding with the crosshair edges of an 18×18 cm^2 field. The saved registration was defined in terms of pixels and allowed subpixel registration. RIT has an option to apply a template to the reference or target that is defined in terms of centimeters. However, this option has an error in coding that incorrectly placed the points one half of a pixel away from their true locations in each direction. This resulted in a 0.5 mm error in both the x and y directions, and was deemed unacceptable.

With the registration points in their correct location on the calculated image, the points on the film image were moved manually to the marked spots visible on the film

Table 2.11: Crop dimensions used in RIT before IMRT analysis

	Orientation	X1 (cm)	X2 (cm)	Y1 (cm)	Y2 (cm)
IMRT					
Multitarget	Coronal	4.5	18.5	2	20
	Sagittal	4.5	18.5	2	20
Prostate	Coronal	5.5	17.5	4	16
	Sagittal	4.5	19	4	16
Head and neck	Coronal	2.5	20.5	1.5	16
	Sagittal	2.5	20.5	1.5	16
C-Shape	Coronal	5	18.5	4	18
	Sagittal	5	20	4	18
VMAT					
Multitarget	Coronal	4.5	18.5	1.5	21
	Sagittal	4.5	18.5	1.5	21
Prostate	Coronal	5.5	18	4	16
	Sagittal	5.5	18	4	16
Head and neck	Coronal	4	20	1.5	16
	Sagittal	4	21	1.5	16
C-Shape	Coronal	5	18.5	4	18
	Sagittal	5	20	4	18

(corresponding to the 18×18 cm^2 field edges). The registration was then applied and saved.

When the images were registered, RIT automatically resampled the target image to the same grid as the reference image. This is the reason that the film image was placed as the target; if the high resolution film were the reference, the analysis calculation time became prohibitively long. Each film was then cropped to a smaller area of interest. Table 2.11 lists the crop dimensions for each treatment and orientation. The images were then normalized to each other using the "Normalize to Area" option. A box covering a majority of the high dose PTV was used for normalization.

With the images registered, normalized, and cropped, the image set was ready for gamma analysis. The RIT software has the ability to perform gamma analysis, but using this capability resulted in a high number of failing pixels in high dose gradient regions (see Fig. 2.18(a)). The source of these artifacts is not immediately clear, as the algorithm

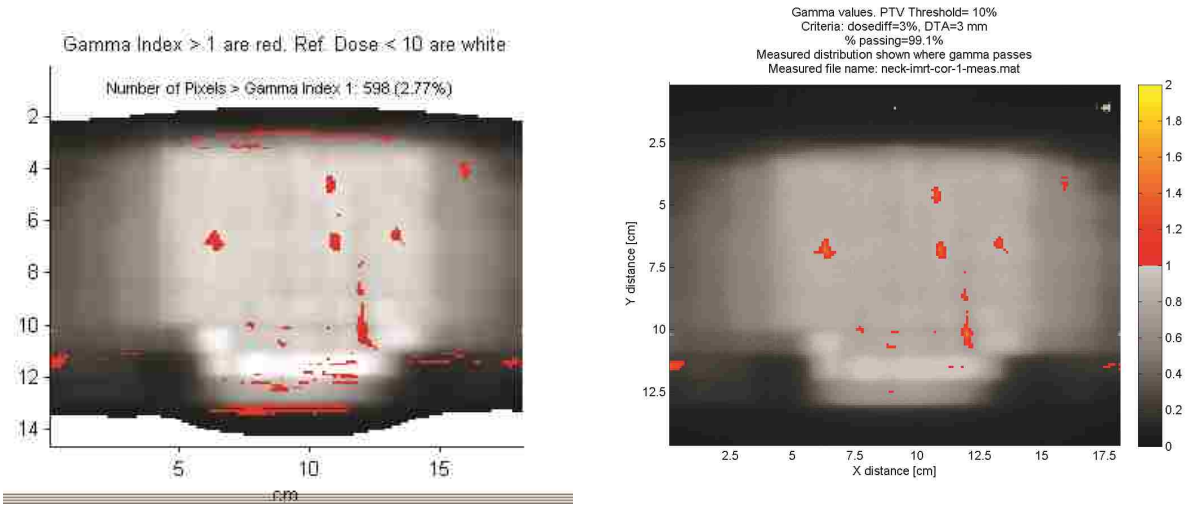

Figure 2.18: Comparison of RIT and in-house gamma analysis results of a coronal head and neck delivery. (a) is from the RIT software, and (b) is the result from the in-house gamma analysis performed in Matlab. Note that in the RIT image there are lines of failing pixels in the high gradient regions. The in-house image does not show these lines of failing pixels, but other areas fail in a fashion similar to the RIT analysis image. Gamma criteria of 3%/3 mm and a threshold value of 10% were used in both cases.

RIT uses to calculate gamma is not available. However, it was noted that if the resolution of the calculated planar dose file was increased (consequently also increasing the film resolution once it was resampled onto the calculated dose grid), the artifacts diminished. It appears that the RIT software doesn't adequately interpolate in its gamma calculation. However, increasing the grid size was undesirable as it greatly increased the calculation time. Therefore, an in-house program was developed using Matlab (MathWorks, Natick, MA) to calculate gamma. This program employed the algorithm described by Ju et al. (2008). Briefly, this algorithm used a geometric interpretation of the gamma metric, allowing interpolation-free calculation. A result from this software is shown in Fig. 2.18(b). The in-house method did not exhibit the high gradient artifacts seen in the RIT gamma analysis.

The in-house gamma analysis program was not able to read the proprietary film data format used by RIT. Therefore, after registration and normalization in RIT, each film and planar dose image were exported from RIT into a Matlab-specific format. These files were read by the in-house software, which calculated gamma and displayed the result

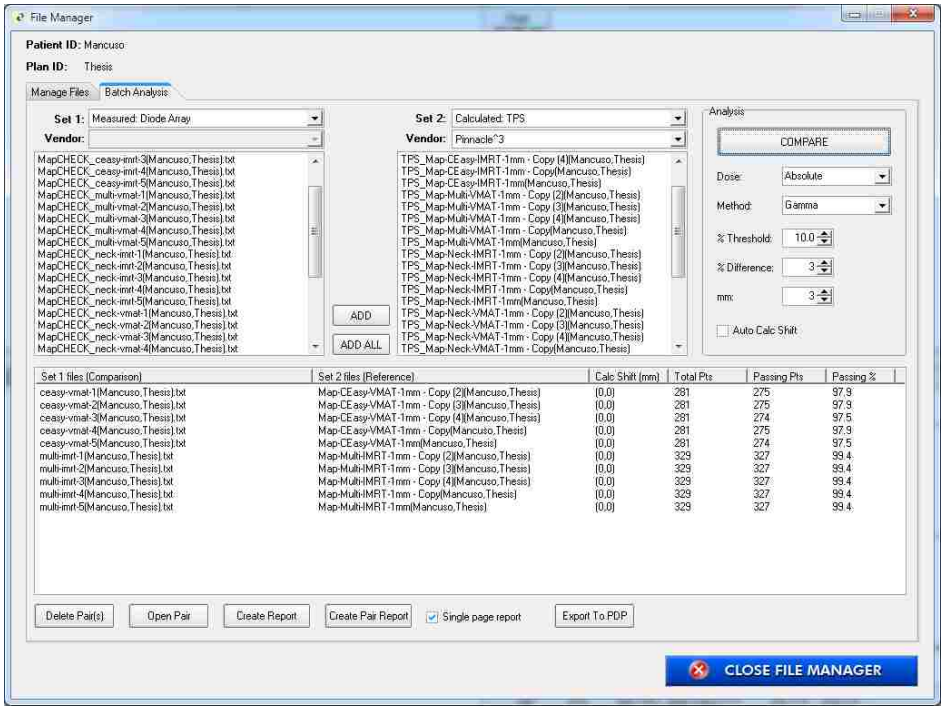

Figure 2.19: Batch analysis window in the MapCHECK software

(see Fig. 2.18(b)), which displayed the film image where gamma passed, and the gamma value where gamma failed. The gamma criteria were set at 3% and 3 mm. The image was thresholded at 10%, meaning that all pixels where the calculated dose was less than 10% of the normalization dose were not included in the gamma calculation.

The in-house program also recorded the percent of pixels passing the gamma test for each comparison in a comma separated value file.

2.4.4 MapCHECK Analysis

The MapCHECK data was analyzed using the MapCHECK software. A gamma analysis using criteria of 3% and 3 mm was performed for each measurement. This was done using the "File Manager" in the MapCHECK software, which has an option to perform batch analysis on several measurements at once. The batch analysis window is shown in Fig. 2.19. The analysis box in the upper right corner allows the user to specify the type of analysis performed. There was no need to perform relative dose measurements so absolute dose was used. Similar to the film analysis, points below the 10% threshold dose were

excluded. The "Auto Calc Shift" option, which attempts to make small shifts in the data to improve agreement, was unchecked for this analysis. In the MapCHECK preferences, the following boxes were checked under "Analysis": "Region Of Interest Analysis," "Van Dyk % Difference," and "Apply Measurement Uncertainty (MapCHECK Only)."

For each measurement, a comparison report like the one seen in Fig. 2.20 was created. This report contained all of the important data about the test performed, including test parameters, the number and percentage of points passing, and the normalization values (even if the data was not actually normalized). The top left image is the contour plot produced from the measured data points, with the diode locations shown. The top right image is the contour plot from the calculated data, again with the diode locations shown. The bottom left image is a contour plot of the calculated data, with passing diodes not shown and failing diodes shown in either red (for overdoses) or blue (for underdoses). The green diode is the normalization diode, which is shown even when no normalization was performed. The green line corresponds to the horizontal dose profile shown in the bottom right image. In the profile, the calculated dose is shown as the black line, passing diodes are yellow, and failing diodes are blue or red. The percent of diodes passing gamma was recorded for each measurement.

The MapCHECK software also includes a correction called the arc calibration matrix. This is meant to correct for an observed directional dependence in MapCHECK measurements for some devices manufactured before 2005. No directional dependence was observed in the MapCHECK device used in this work, so the correction was not used.

2.4.5 Statistical Tests

The Wilcoxon rank-sum test was used to determine if differences between modalities were significantly different. The rank-sum test was chosen over a t-test because the normality of the data distributions was in question (see Sec. 4.2.1), and the rank-sum test does not assume a normal distribution of data. However, this also makes the Wilcoxon rank-sum test less powerful than a t-test. Two different classes of comparisons were made.

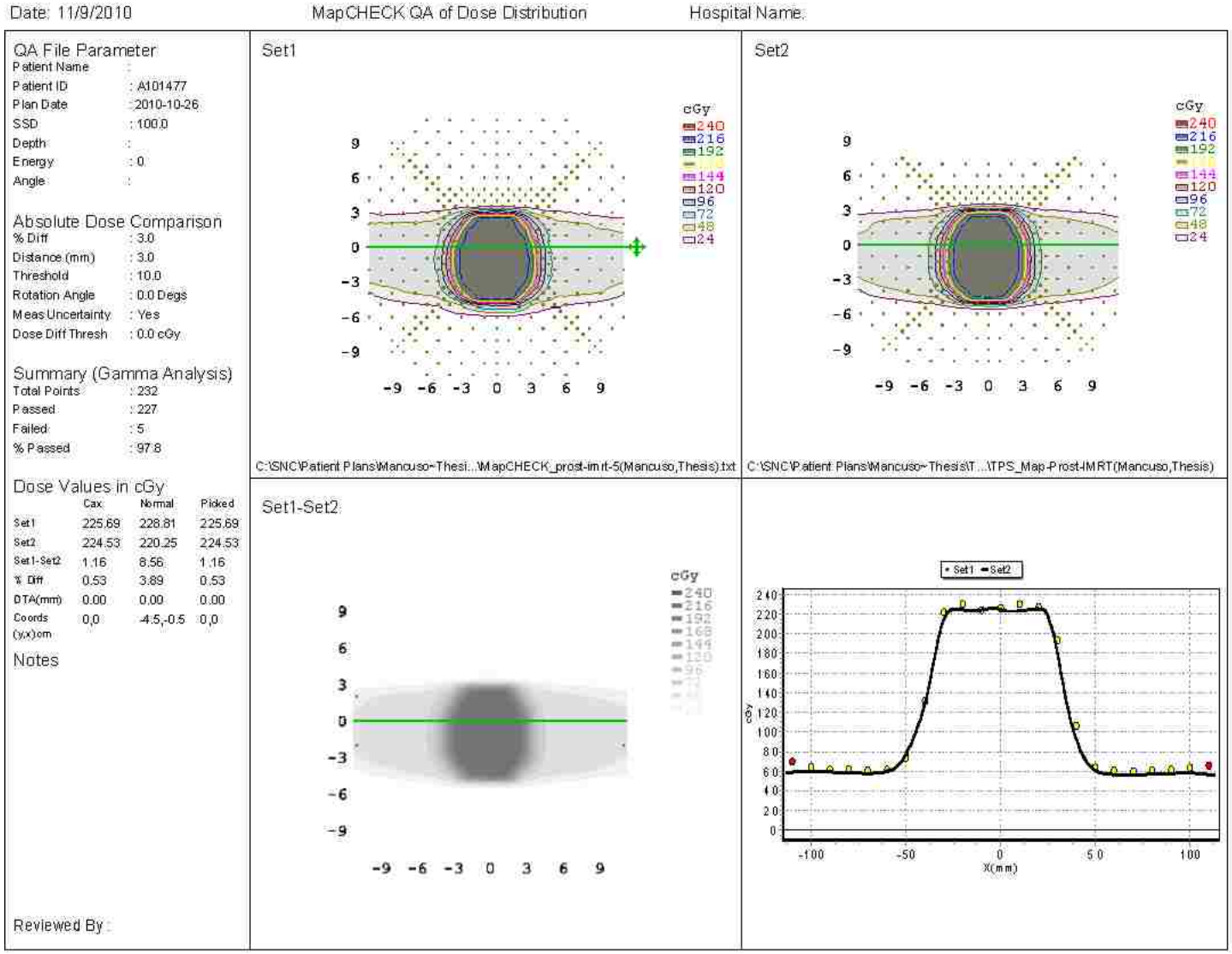

Figure 2.20: Sample comparison report from MapCHECK results

(1) Site-specific comparisons were made between identical measurement setup. For example, the five point dose measurements in the central target of the IMRT multitarget treatment were compared against the five point dose measurements at the same location in the VMAT multitarget treatment. This method of comparison was only used for the point dose data and the MapCHECK data. It was not used for the film data because the film data only took three measurements for each film setup, and the Wilcoxon rank-sum test lacked the power to conclude a statistically significant difference ($p < 0.05$) for such a small sample size.

(2) Global comparisons were performed between all of the IMRT and VMAT data of each measurement type. In each global comparison, the mean values from each set of site-specific measurements were used for the statistical tests, rather than all of the values measured. This was because the individual measurements for each specific site were found to have little variation when compared to the variation of measurements between sites. This means that the individual measurements did not constitute independent measurements for the purposes of a statistical test.

Chapter 3

Results

3.1 Planning Results

Planned dose objectives and treatment planning results for each structure set geometry are displayed in Table 3.1. Results that met the TG 119 dose goals are highlighted in green, and values that did not meet the dose goals but fell within one standard deviation of the mean values reported by the institutions participating in TG 119 are highlighted in yellow. There were no instances in which plan results failed to meet at least one of these standards.

Figures 3.1–3.8 show isodose distributions and DVHs for each of the treatment plans. For the multitarget structures set (Figs. 3.1 and 3.2), a coronal plane is shown; for the others, axial planes are shown.

3.2 Point Dose Results

For each point dose measurement location, dose was measured for five treatment deliveries in the cylindrical phantom. Table 3.2 lists the dose measurements taken for each of the points, along with the dose calculated by Pinnacle[3]. Table 3.3 lists the percent

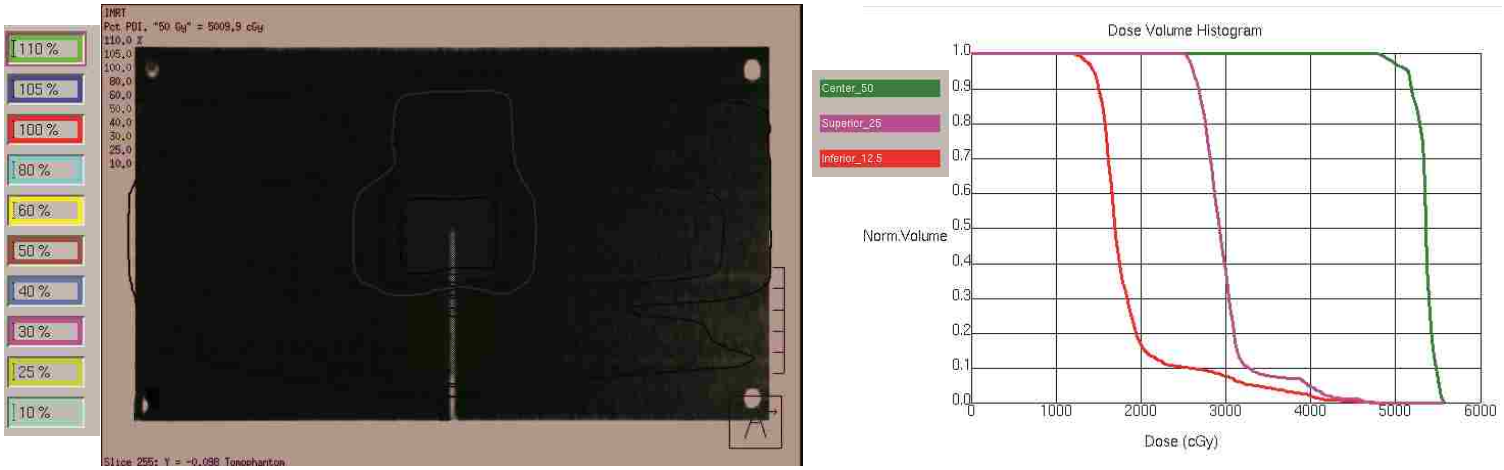

Figure 3.1: Multitarget IMRT isodose distribution and DVH

Table 3.1: Treatment planning results. For each parameter, the TG 119 goals and results are shown, along with the values obtained for the IMRT and VMAT plans created in the current study. Results that met the TG 119 objectives are highlighted in green, while results that did not meet the TG 119 objectives but still fell within one standard deviation of the mean are shown in yellow.

Planning parameter	Plan goal (cGy)	Mean (cGy)	Standard deviation (cGy)	IMRT (cGy)	VMAT (cGy)
Multitarget					
Central target D_{99}	>5000	4955	162	4857	5132
Central target D_{10}	<5300	5455	173	5475	5532
Superior target D_{99}	>2500	2516	85	2543	2648
Superior target D_{10}	<3500	3412	304	3266	3410
Inferior target D_{99}	>1250	1407	185	1277	1255
Inferior target D_{10}	<2500	2418	272	2541	2398
Prostate					
Prostate D_{95}	>7560	7566	21	7609	7560
Prostate D_5	<8300	8143	156	7784	7813
Rectum D_{30}	<7000	6536	297	6846	6830
Rectum D_{10}	<7500	7303	150	7464	7473
Bladder D_{30}	<7000	4394	878	4868	4627
Bladder D_{10}	<7500	6269	815	6930	6941
Head and neck					
PTV D_{90}	5000	5028	58	5203	5147
PTV D_{99}	>4650	4704	52	4763	4755
PTV D_{20}	<5500	5299	93	5385	5439
Cord maximum	<4000	3741	250	3940	3951
Left Parotid D_{50}	<2000	1798	184	1875	1850
Right Parotid D_{50}	<2000	1798	184	1833	1910
C-shape					
PTV D_{95}	5000	5010	17	5001	5007
PTV D_{10}	<5500	5440	52	5330	5463
Core D_{10}	<2500	2200	314	2489	2163

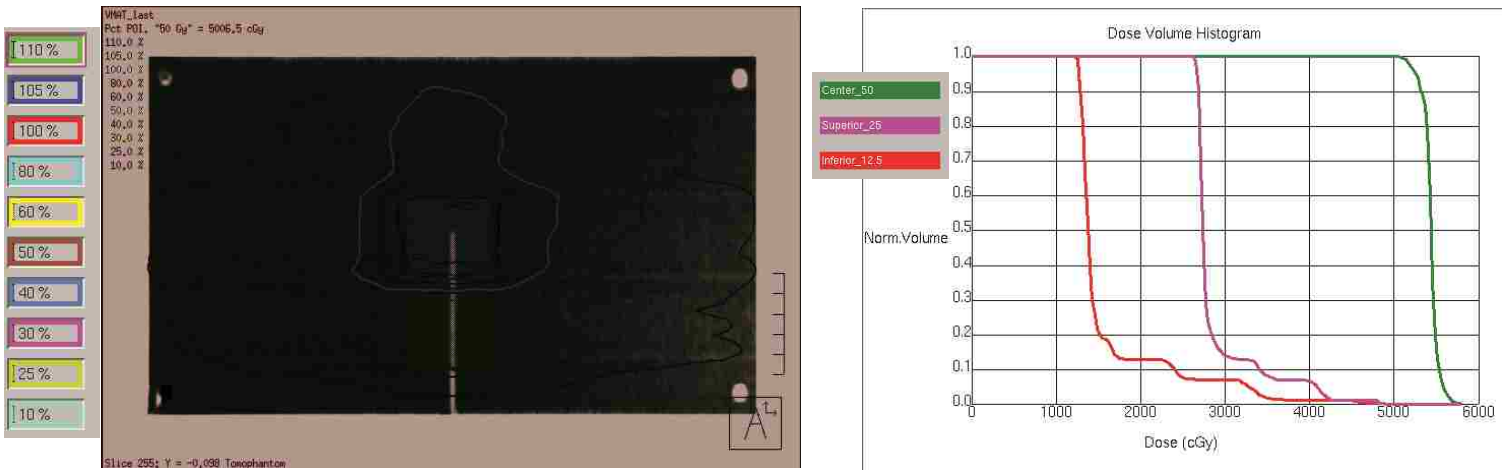

Figure 3.2: Multitarget VMAT isodose distribution and DVH

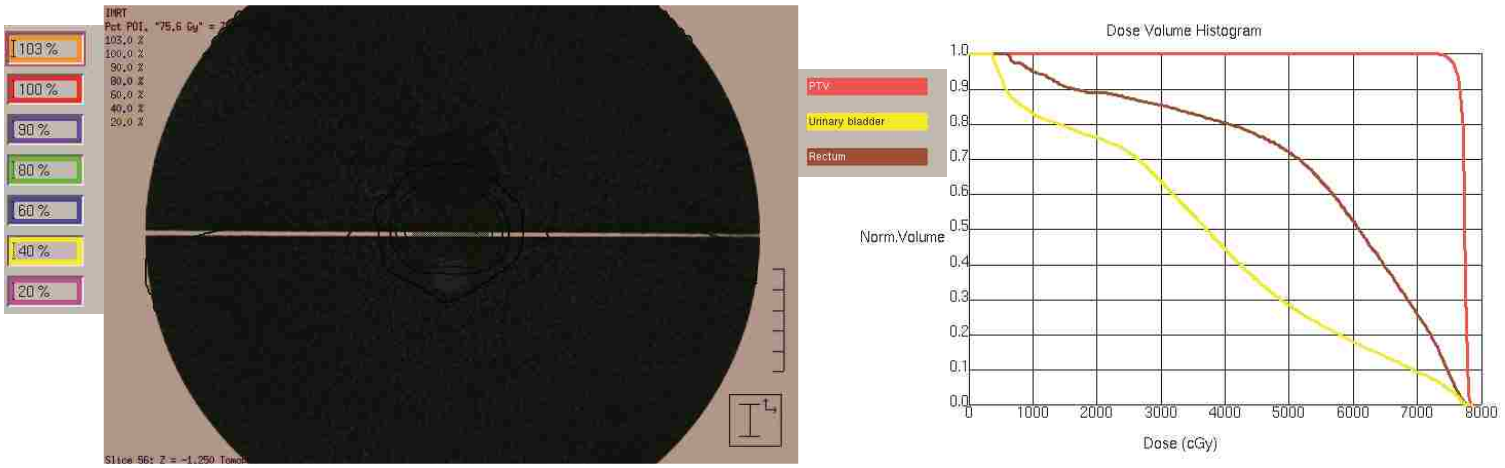

Figure 3.3: Prostate IMRT isodose distribution and DVH

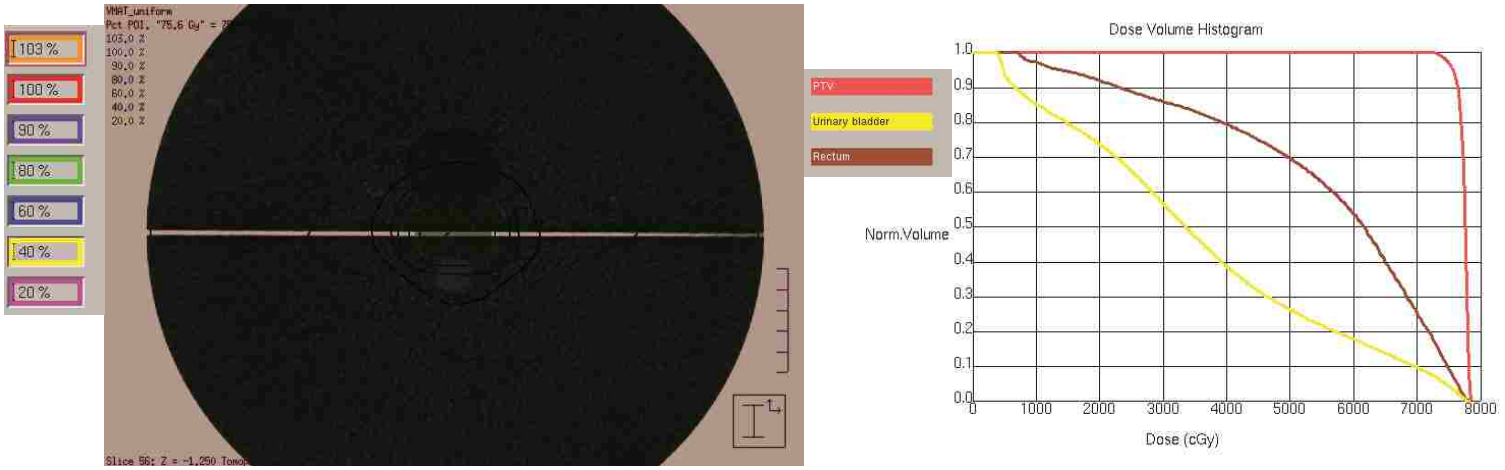

Figure 3.4: Prostate VMAT isodose distribution and DVH

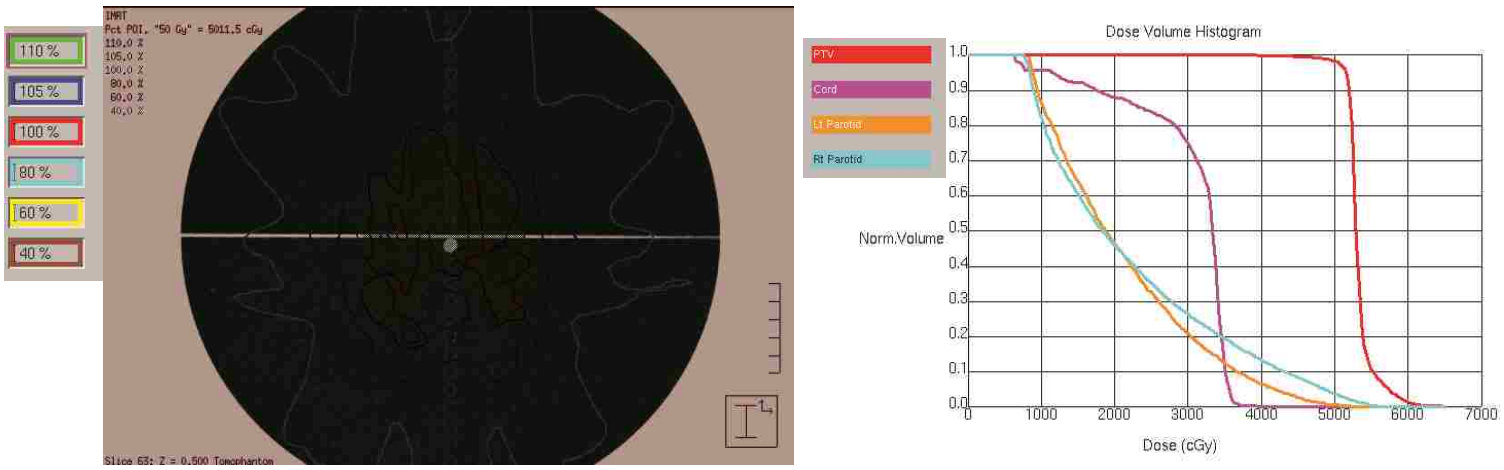

Figure 3.5: Head and neck IMRT isodose distribution and DVH

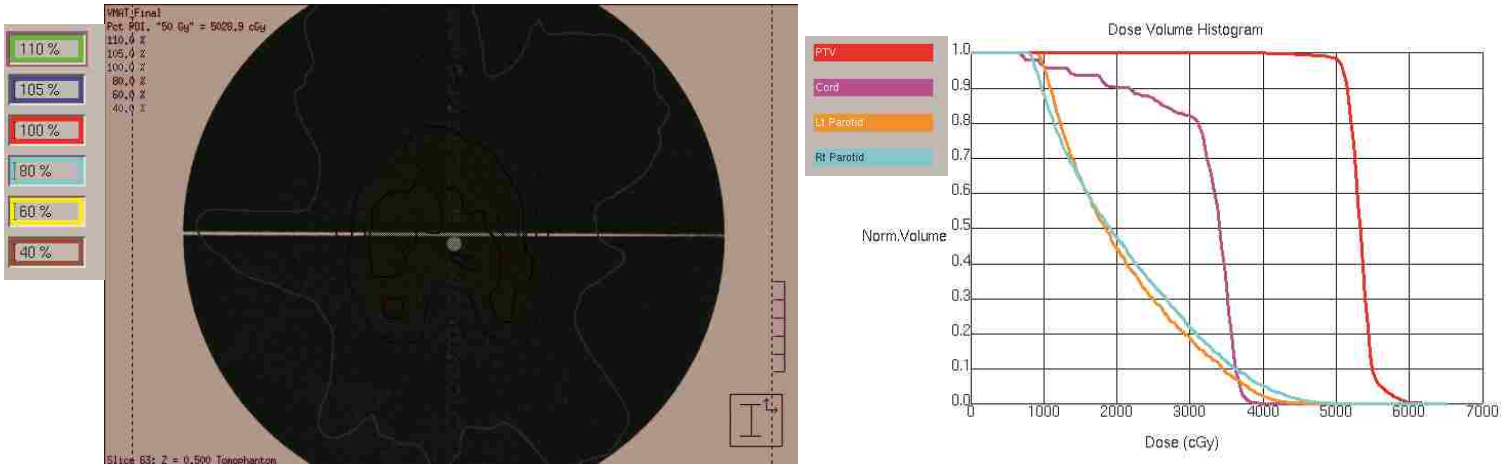

Figure 3.6: Head and neck VMAT isodose distribution and DVH

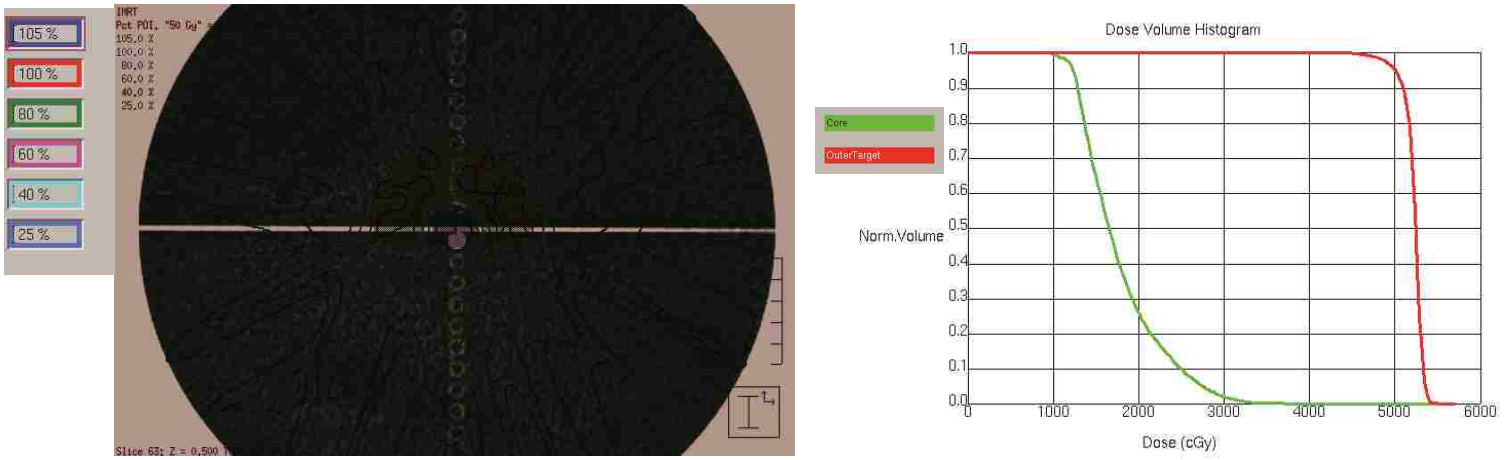

Figure 3.7: C-shape IMRT isodose distribution and DVH

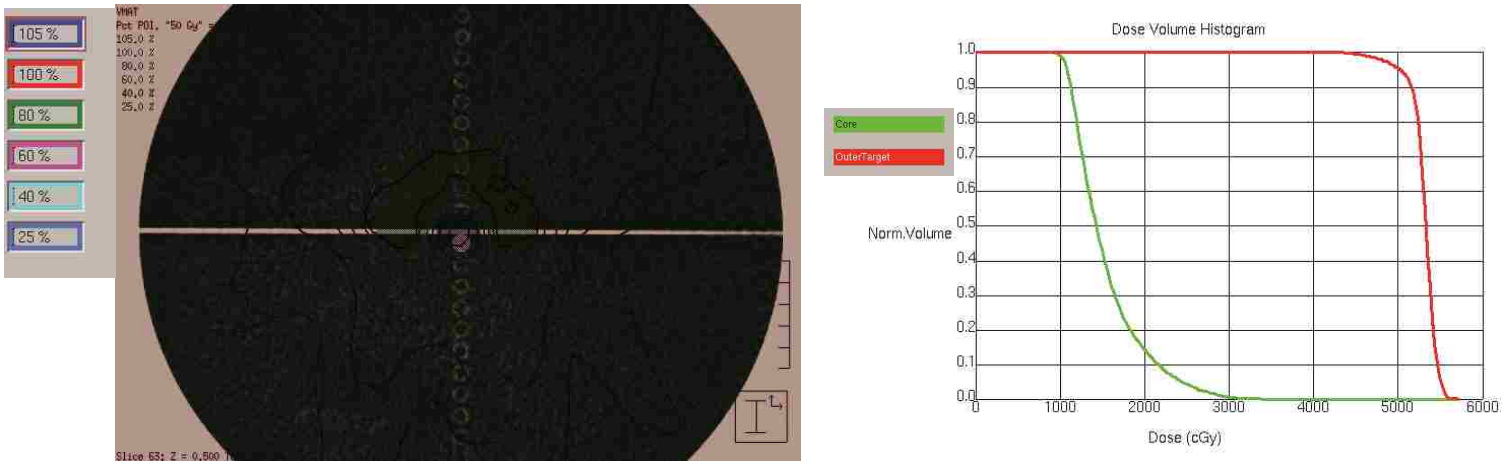

Figure 3.8: C-shape VMAT isodose distribution and DVH

Table 3.2: Point dose measurements: Dose. The measured doses are given for all five measurements taken at each point discussed in Table 2.9. The dose calculated by Pinnacle[3] is included for each point.

Plan	Point description	Calculated dose (cGy)	Dose measurements (cGy)				
IMRT							
Multitarget	50 Gy target	214.7	213.7	213.7	214.2	214.2	213.7
	25 Gy target	121.7	119.6	119.1	118.1	117.6	118.1
	12.5 Gy target	64.2	60.1	60.1	60.1	59.6	59.0
Prostate	PTV	184.0	182.5	182.5	182.5	183.1	182.5
	Rectum	132.9	134.4	133.9	134.9	134.9	133.9
	Bladder	141.3	138.1	139.7	138.1	138.6	139.7
Head and	PTV	213.0	207.1	207.1	207.1	207.1	207.1
neck	Spinal cord	123.3	125.7	124.7	123.6	122.1	124.2
C-shape	Central core	55.6	53.6	52.9	53.5	52.9	52.9
	Outer target	207.9	212.3	212.3	211.7	211.7	212.3
VMAT							
Multitarget	50 Gy target	218.6	218.9	218.9	218.9	219.4	218.9
	25 Gy target	107.8	107.6	108.1	108.1	108.1	108.1
	12.5 Gy target	56.2	53.8	53.3	53.8	53.8	53.8
Prostate	PTV	185.3	184.1	184.1	184.1	184.6	184.6
	Rectum	143.2	144.4	143.8	144.4	143.8	143.8
	Bladder	136.7	128.1	129.7	129.2	129.7	130.2
Head and	PTV	206.2	198.2	197.7	198.2	198.2	197.7
neck	Spinal cord	133.9	127.8	127.8	126.8	126.2	128.3
C-shape	Central core	47.8	44.2	43.7	43.7	44.2	44.2
	Outer target	207.7	202.4	202.4	202.4	200.8	201.9

Table 3.3: Point dose measurements: Percent difference. The percent differences are given for all five measurements taken at each point discussed in Table 2.9. The calculated dose at each point is included for reference.

Plan	Point description	Calculated dose (cGy)	Percent differences (%)				
IMRT							
Multitarget	50 Gy target	214.7	−0.51	−0.51	−0.25	−0.25	−0.51
	25 Gy target	121.7	−1.03	−1.29	−1.81	−2.07	−1.81
	12.5 Gy target	64.2	−2.06	−2.06	−2.06	−2.32	−2.58
Prostate	PTV	184.0	−0.81	−0.81	−0.81	−0.52	−0.81
	Rectum	132.9	0.84	0.55	1.14	1.14	0.55
	Bladder	141.3	−1.79	−0.92	−1.79	−1.50	−0.92
Head and	PTV	213.0	−2.95	−2.95	−2.95	−2.95	−2.95
neck	Spinal cord	123.3	1.21	0.69	0.17	−0.61	0.43
C-shape	Central core	55.6	−1.00	−1.33	−1.07	−1.33	−1.33
	Outer target	207.9	2.18	2.18	1.92	1.92	2.18
VMAT							
Multitarget	50 Gy target	218.6	0.15	0.15	0.15	0.42	0.15
	25 Gy target	107.8	−0.09	0.17	0.17	0.17	0.17
	12.5 Gy target	56.2	−1.19	−1.45	−1.19	−1.19	−1.19
Prostate	PTV	185.3	−0.66	−0.66	−0.66	−0.37	−0.37
	Rectum	143.2	0.64	0.35	0.64	0.35	0.35
	Bladder	136.7	−4.75	−3.88	−4.17	−3.88	−3.59
Head and	PTV	206.2	−3.98	−4.24	−3.98	−3.98	−4.24
neck	Spinal cord	133.9	−3.05	−3.05	−3.57	−3.83	−2.78
C-shape	Central core	47.8	−1.79	−2.05	−2.05	−1.79	−1.79
	Outer target	207.7	−2.65	−2.65	−2.65	−3.43	−2.91

differences of each measurement, using the method described in Sec. 2.4.1.

Table 3.4 lists the means and standard deviations of the dose values and percent differences for each point. A Wilcoxon rank-sum test was performed for each point comparing the IMRT and VMAT percent difference results, the results of which are also displayed in Table 3.4. The five measurements at any given point generally exhibited a small spread of values, leading to the rank-sum test indicating significance ($p < 0.05$) for the majority of comparisons.

Table 3.4: Point dose measurements aggregated by point. For each point, the means and standard deviations of the dose values and the percent differences are shown, as well as the result of a Wilcoxon rank-sum test comparing the IMRT and VMAT results. The calculated point doses are also included for reference.

Point description	Calculated dose (cGy)		Mean dose (cGy) ± St. Dev.		Mean % diff ± St. Dev.		Wilcoxon rank-sum test p
Multitarget	**IMRT**	**VMAT**	**IMRT**	**VMAT**	**IMRT**	**VMAT**	
50 Gy target	214.7	218.6	213.9 ± 0.3	219.0 ± 0.2	−0.40 ± 0.14	0.21 ± 0.12	0.0079
25 Gy target	121.7	107.8	118.5 ± 0.9	108.0 ± 0.2	−1.60 ± 0.43	0.12 ± 0.12	0.0079
12.5 Gy target	64.2	56.2	59.8 ± 0.5	53.7 ± 0.2	−2.22 ± 0.23	−1.25 ± 0.12	0.0079
Prostate							
PTV	184.0	185.3	182.6 ± 0.2	184.3 ± 0.3	−0.75 ± 0.13	−0.55 ± 0.16	0.032
Rectum	132.9	143.2	134.4 ± 0.5	144.0 ± 0.3	0.84 ± 0.29	0.47 ± 0.16	0.063
Bladder	141.3	136.7	138.8 ± 0.8	129.4 ± 0.8	−1.38 ± 0.44	−4.06 ± 0.44	0.0079
Head and neck							
PTV	213.0	206.2	207.1 ± 0.0	198.0 ± 0.3	−2.95 ± 0.00	−4.09 ± 0.14	0.0079
Spinal cord	123.3	133.9	124.1 ± 1.4	127.4 ± 0.9	0.38 ± 0.68	−3.25 ± 0.43	0.0079
C-shape							
Central core	55.6	47.8	53.2 ± 0.3	44.0 ± 0.3	−1.22 ± 0.16	−1.89 ± 0.14	0.0079
Outer target	207.9	207.7	212.0 ± 0.3	202.0 ± 0.7	2.07 ± 0.14	−2.86 ± 0.34	0.0079

Table 3.5: Point dose measurements aggregated by modality. The reported means and standard deviations were calculated using the mean values shown in Table 3.4. Also included is the result of a Wilcoxon rank-sum test comparing the IMRT and VMAT results.

Mean % difference ± St. Dev.		Wilcoxon rank-sum test p
IMRT	**VMAT**	
-0.72 ± 1.50	-1.71 ± 1.77	0.27

Table 3.6: Film gamma calculation results. Gamma analysis was performed using criteria of 3% and 3 mm. The percent of pixels with gamma less than one was reported for each measurement. The results for each of the three films irradiated by each treatment and in each film orientation are given here.

Plan	Film orientation	% pixels passing γ, criteria=3%/3 mm					
		IMRT			**VMAT**		
Multitarget	Coronal	98.68	99.51	99.50	98.89	98.99	99.11
Prostate		99.96	99.99	99.98	100.00	99.97	100.00
Neck		99.07	99.28	99.00	98.00	97.55	97.53
C-shape		98.88	99.41	99.57	99.93	99.89	99.94
Multitarget	Sagittal	98.08	98.74	99.18	98.68	99.45	99.00
Prostate		99.05	99.23	98.50	99.98	100.00	99.97
Neck		96.14	97.07	96.34	98.33	98.28	98.33
C-shape		99.64	99.22	98.92	99.40	98.71	97.63

Table 3.5 lists the means and standard deviations of the results from Table 3.4, aggregated by modality. The result of a Wilcoxon rank-sum test is also displayed. The difference between the IMRT and VMAT point dose results was not statistically significant ($p > 0.05$).

3.3 Film Results

For each plan and film orientation (coronal and sagittal), three films were irradiated and analyzed. Each film was compared to a calculated planar dose distribution from Pinnacle[3] using gamma analysis with criteria of 3%/3 mm, and the percent of pixels with gamma less than one was calculated. Table 3.6 reports the percent of pixels passing for each film

Table 3.7: Film gamma results aggregated by treatment setup. The mean percent of pixels passing for each setup is shown with its standard deviation.

Plan and film orientation	Mean % of pixels passing ± St. Dev.	
Multitarget	**IMRT**	**VMAT**
Coronal	99.23 ± 0.48	99.00 ± 0.11
Sagittal	98.67 ± 0.55	99.04 ± 0.39
Prostate		
Coronal	99.98 ± 0.02	99.99 ± 0.02
Sagittal	98.93 ± 0.38	99.98 ± 0.02
Head and neck		
Coronal	99.12 ± 0.15	97.69 ± 0.27
Sagittal	96.52 ± 0.49	98.31 ± 0.03
C-shape		
Coronal	99.29 ± 0.36	99.92 ± 0.03
Sagittal	99.26 ± 0.36	98.58 ± 0.89

analysis. The mean and standard deviation of all the films from each treatment setup are shown in Table 3.7. Like the point dose results, the film results showed little variation between films from the same treatment setup. No statistical tests were performed on the site-specific film data because the Wilcoxon rank-sum test lacked sufficient statistical power for the given sample size to distinguish significant differences at the 5% level.

Table 3.8 lists the means and standard deviations found from the means listed in Table 3.7, aggregated by the two modalities, including the result of the Wilcoxon rank-sum test. The difference between the IMRT and VMAT results was not significant ($p > 0.05$).

Figures 3.9–3.12 show representative gamma distributions for each of the structure sets, modalities, and orientations. The other film results were similar to these results (see Appendix A).

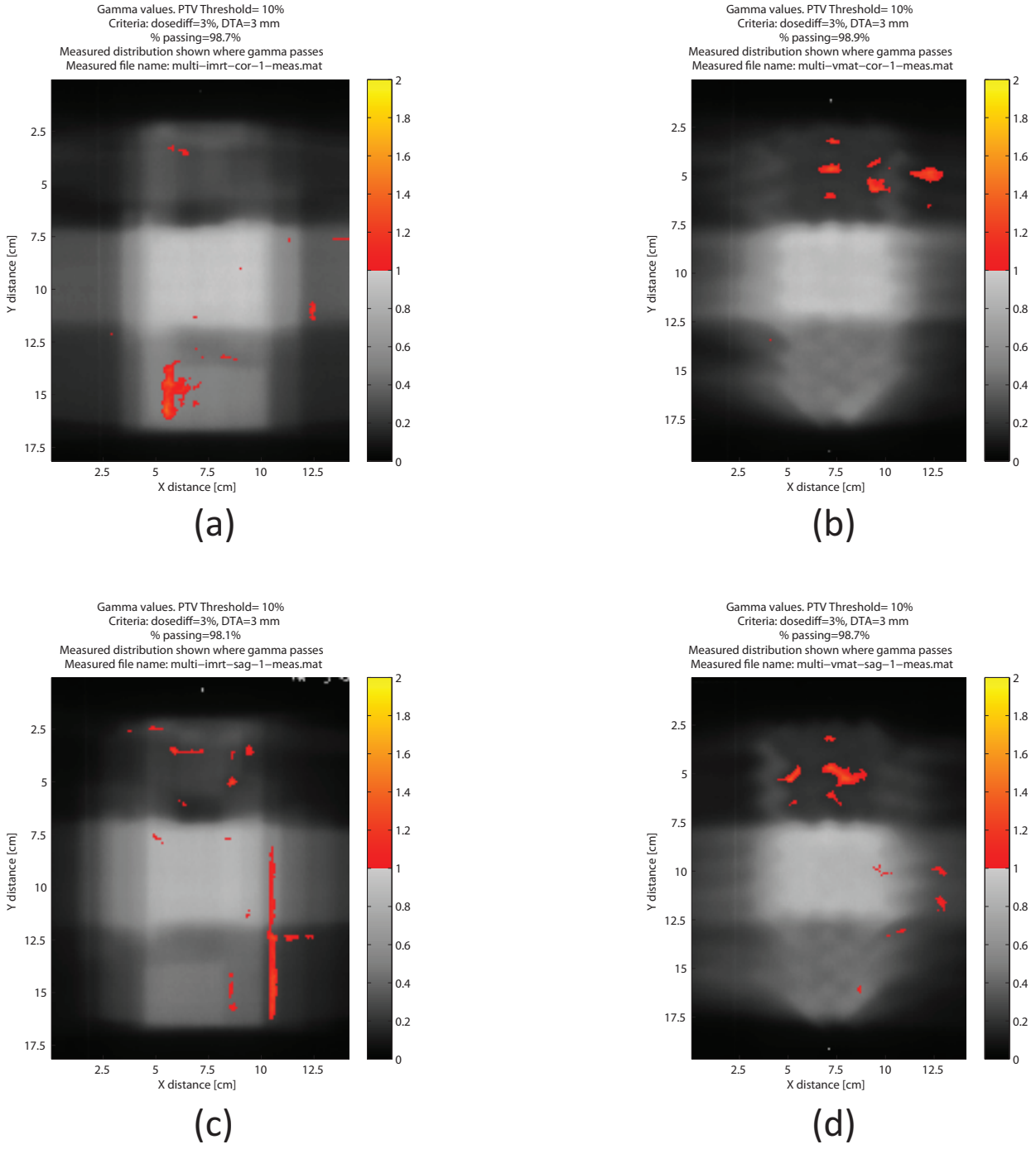

Figure 3.9: Representative gamma results for the multitarget film data. (a) and (b) are the coronal measurements for IMRT and VMAT, respectively; (c) and (d) are the sagittal measurements for IMRT and VMAT, respectively.

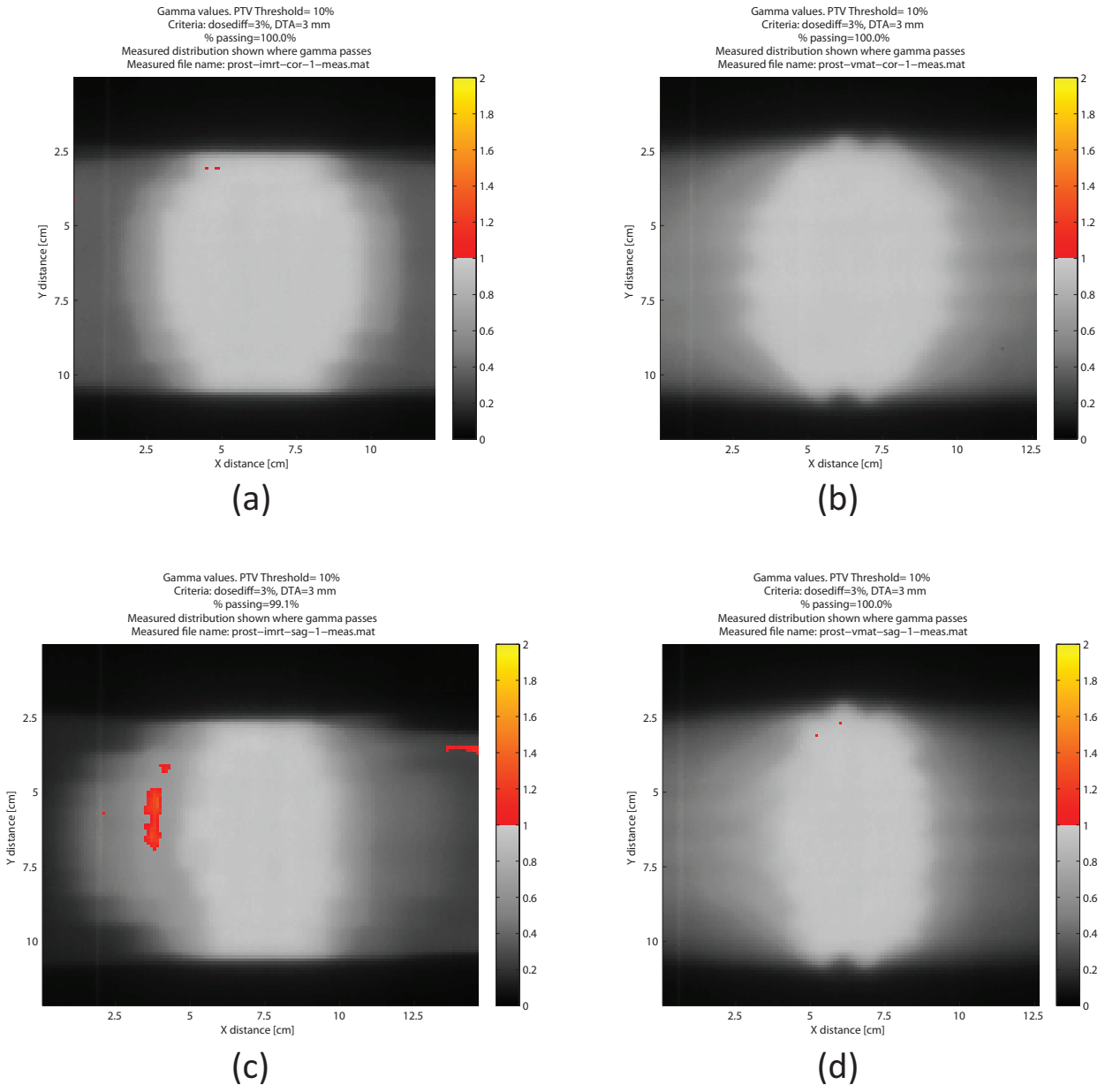

Figure 3.10: Representative gamma results for the prostate film data. (a) and (b) are the coronal measurements for IMRT and VMAT, respectively; (c) and (d) are the sagittal measurements for IMRT and VMAT, respectively.

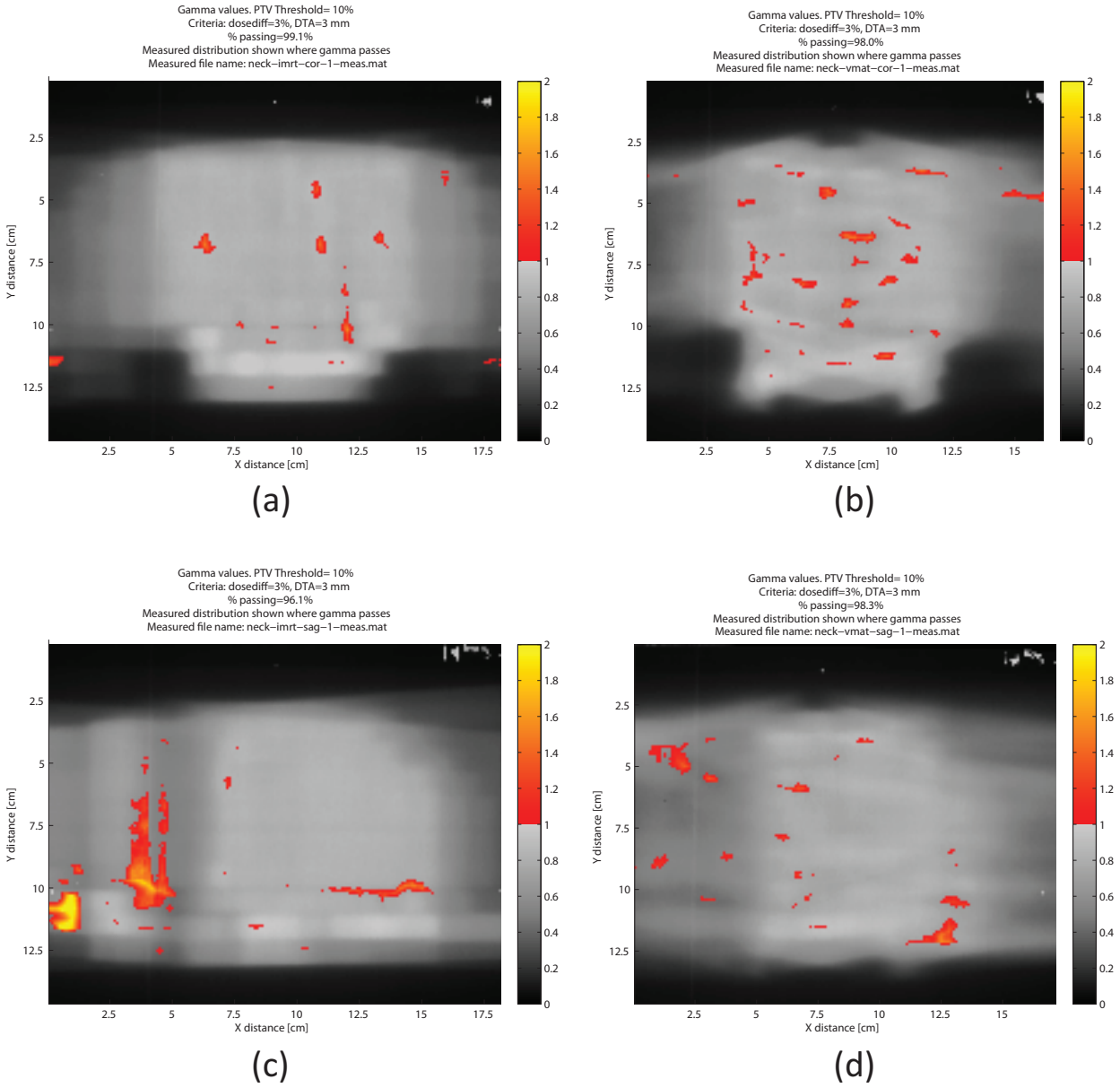

Figure 3.11: Representative gamma results for the head and neck film data. (a) and (b) are the coronal measurements for IMRT and VMAT, respectively; (c) and (d) are the sagittal measurements for IMRT and VMAT, respectively.

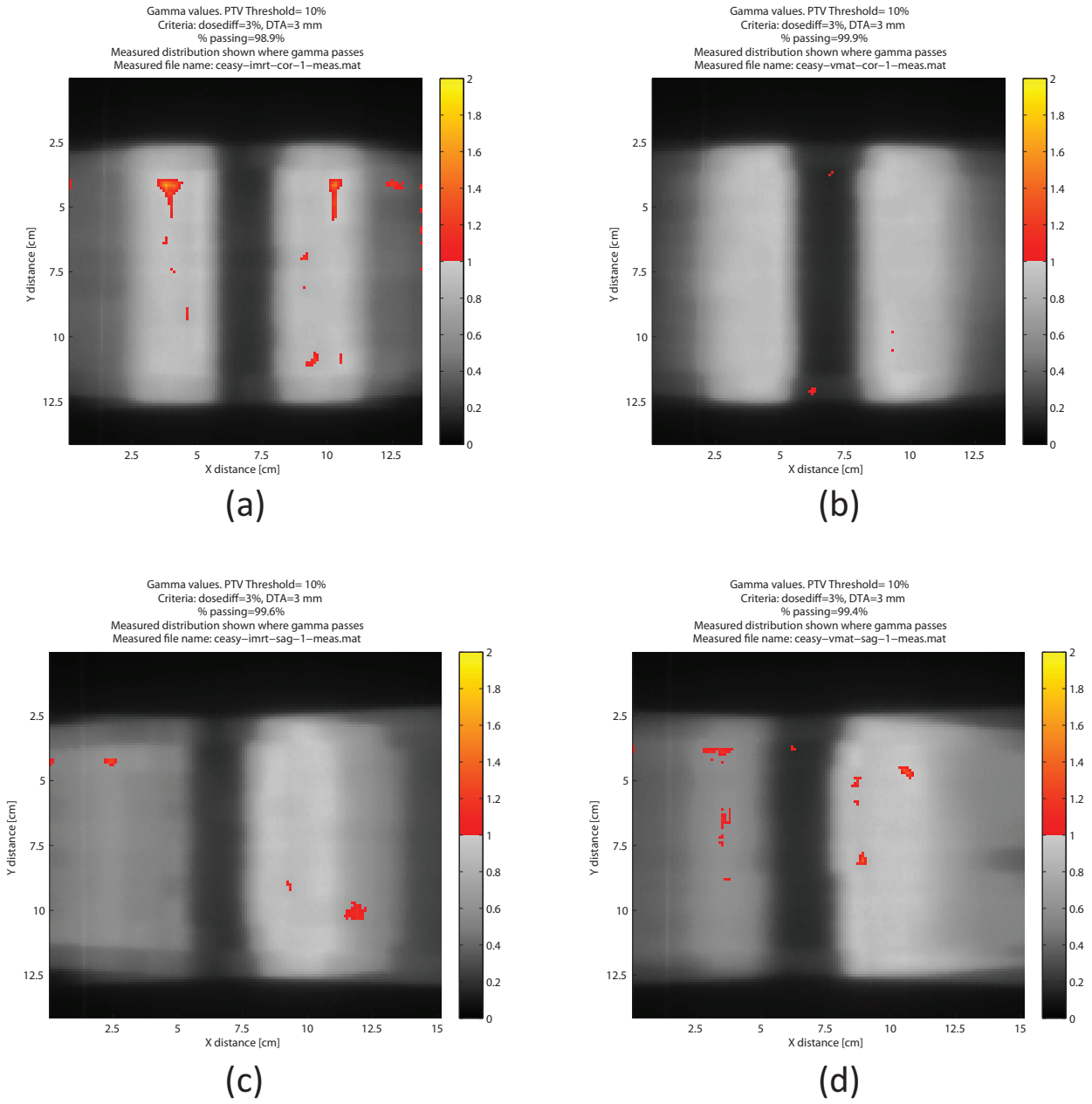

Figure 3.12: Representative gamma results for the C-shape film data. (a) and (b) are the coronal measurements for IMRT and VMAT, respectively; (c) and (d) are the sagittal measurements for IMRT and VMAT, respectively.

Table 3.8: Film gamma results aggregated by modality. The reported means and standard deviations were calculated using the mean values shown in Table 3.7. Also included is the result of a Wilcoxon rank-sum test comparing the IMRT and VMAT results.

Mean % of pixels passing ± St. Dev.		Wilcoxon rank-sum test p
IMRT	**VMAT**	
98.87 ± 1.02	99.07 ± 0.85	1.00

Table 3.9: MapCHECK gamma calculation results. Gamma analysis was performed using criteria of 3% and 3 mm. The percent of diode measurements with gamma less than one was reported. The results for each of the five MapCHECK measurements irradiated by each treatment are given here.

Plan	% diodes passing γ criteria=3%/3 mm				
IMRT					
Multitarget	99.39	99.39	99.39	99.39	99.39
Prostate	98.71	98.71	98.71	98.71	98.71
Head and neck	98.47	98.85	98.47	98.47	98.09
C-shape	98.87	97.74	98.50	97.74	97.74
VMAT					
Multitarget	98.70	98.37	98.70	98.37	99.02
Prostate	100.00	99.59	99.59	99.59	99.59
Head and neck	98.21	98.21	98.57	98.57	98.21
C-shape	97.86	97.86	97.51	97.86	97.51

3.4 MapCHECK Results

Each treatment plan was delivered five times to the MapCHECK device. The recorded distribution was analyzed in the MapCHECK software using gamma analysis with criteria of 3%/3 mm. Each measurement was compared to the calculated planar dose distribution from Pinnacle[3]. The percent of diode measurements passing gamma is reported for each MapCHECK measurement in Table 3.9. Each treatment type was aggregated and the means and standard deviations are listed in Table 3.10, with the results of Wilcoxon rank-sum

Table 3.10: MapCHECK gamma results aggregated by treatment. The mean percent of diodes passing for each treatment is shown with its standard deviation, along with a Wilcoxon rank-sum test comparing the IMRT and VMAT results.

Plan	Mean % of diodes passing ± St. Dev.		Wilcoxon rank-sum test p
	IMRT	VMAT	
Multitarget	99.39 ± 0.00	98.63 ± 0.27	0.0079
Prostate	98.71 ± 0.00	99.67 ± 0.19	0.0079
Head and neck	98.47 ± 0.27	98.35 ± 0.20	0.77
C-shape	98.12 ± 0.53	97.72 ± 0.19	0.57

Table 3.11: MapCHECK gamma results aggregated by modality. The reported means and standard deviations were calculated using the mean values shown in Table 3.10. Also included is the result of a Wilcoxon rank-sum test comparing the IMRT and VMAT results.

Mean % of diodes passing ± St. Dev.		Wilcoxon rank-sum test p
IMRT	**VMAT**	
98.67 ± 0.54	98.59 ± 0.81	0.89

tests comparing the VMAT and IMRT results. The head and neck and C-shape differences were not significant ($p > 0.05$), and the prostate and multitarget differences were ($p < 0.05$). Similar to the film and point dose results, the MapCHECK results showed little variation between measurements. Table 3.11 contains the means and standard deviations of the mean IMRT and VMAT results listed in Table 3.10, aggregated for each treatment modality, along with the result of the Wilcoxon rank-sum test. The difference between modalities was not significant ($p > 0.05$).

Figures 3.13–3.20 are representative results from the MapCHECK measurements for each structure set and modality, as output by the MapCHECK software. The other MapCHECK results were similar to these results (see Appendix B).

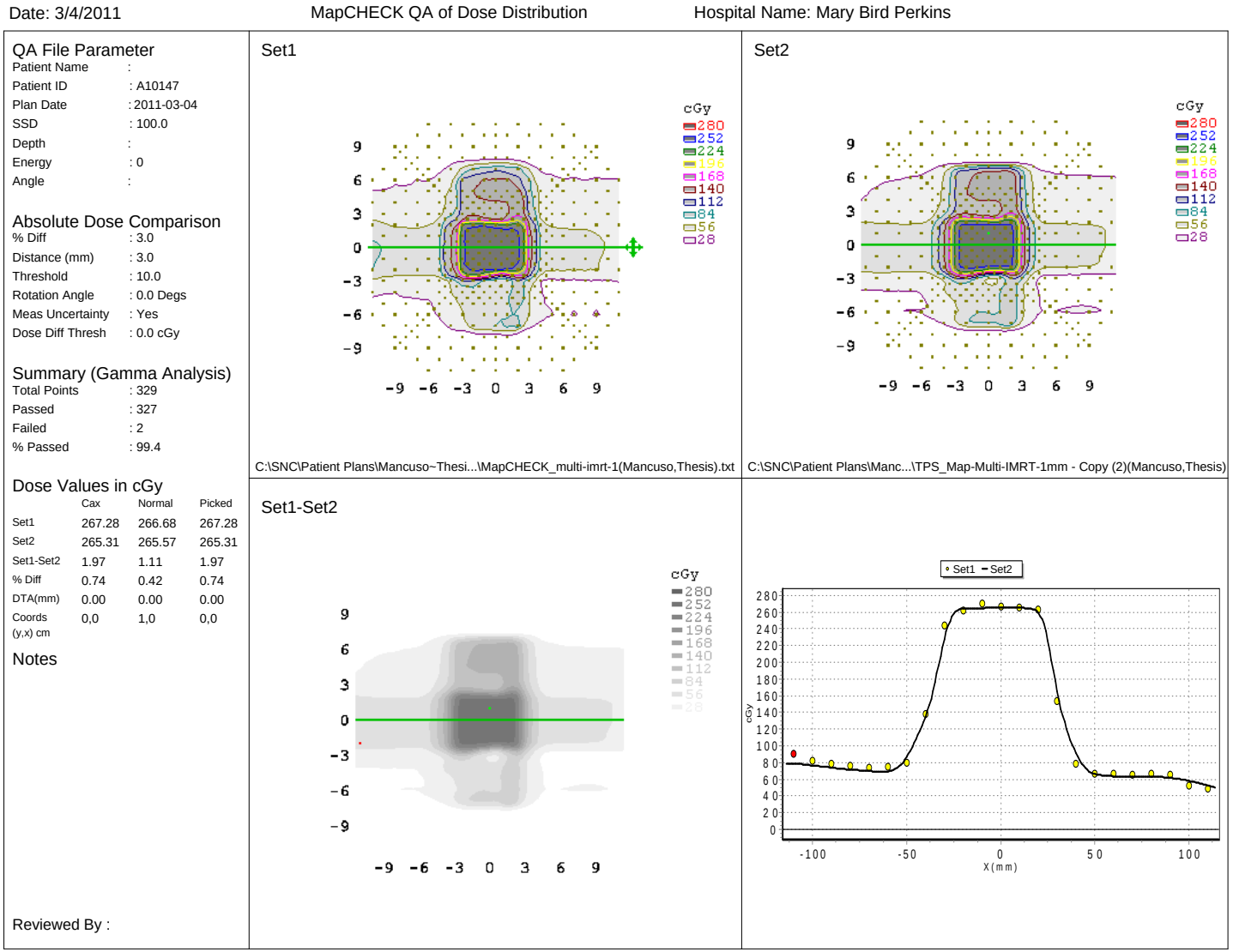

Figure 3.13: Representative MapCHECK output for a multitarget IMRT delivery.

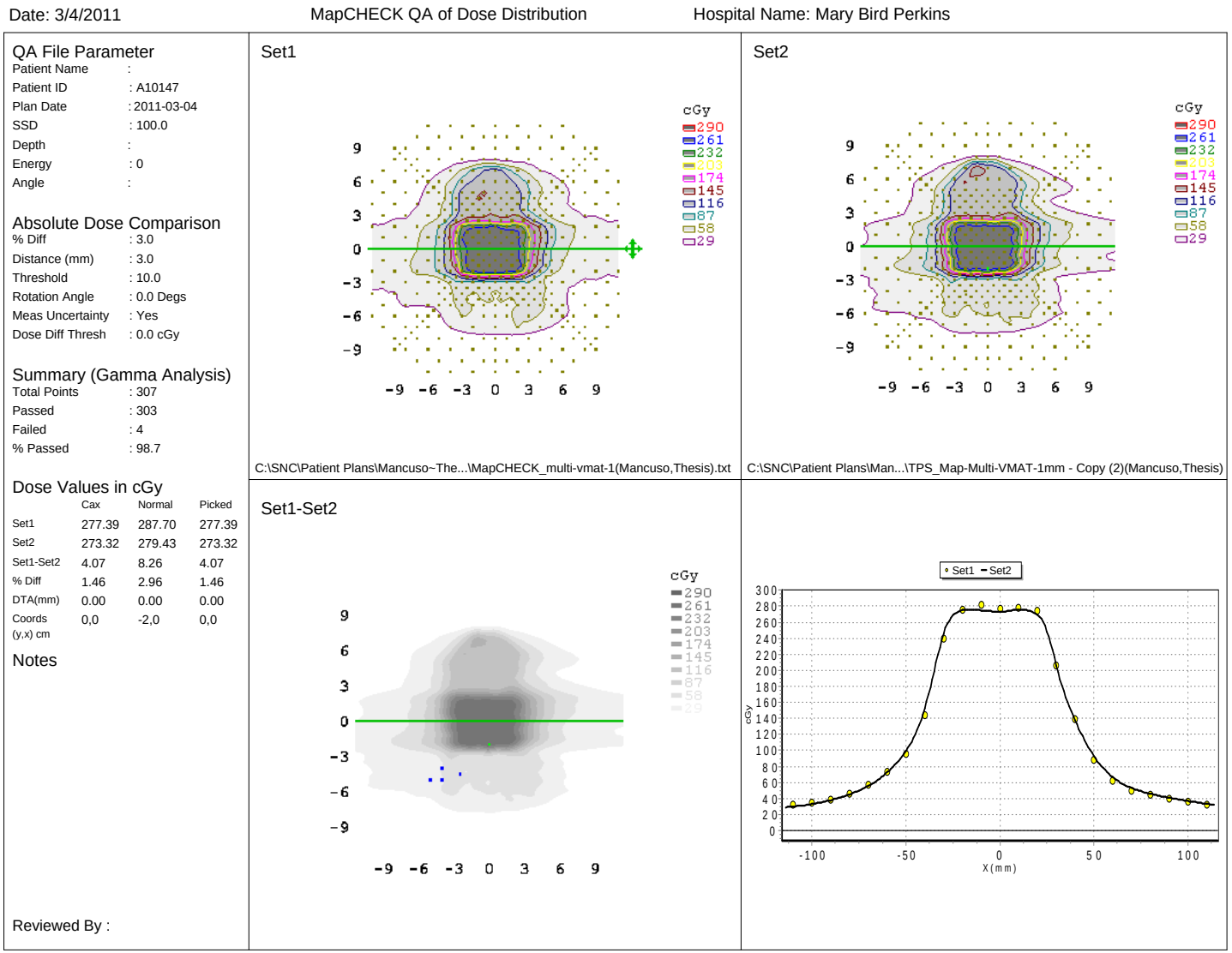

Figure 3.14: Representative MapCHECK output for a multitarget VMAT delivery.

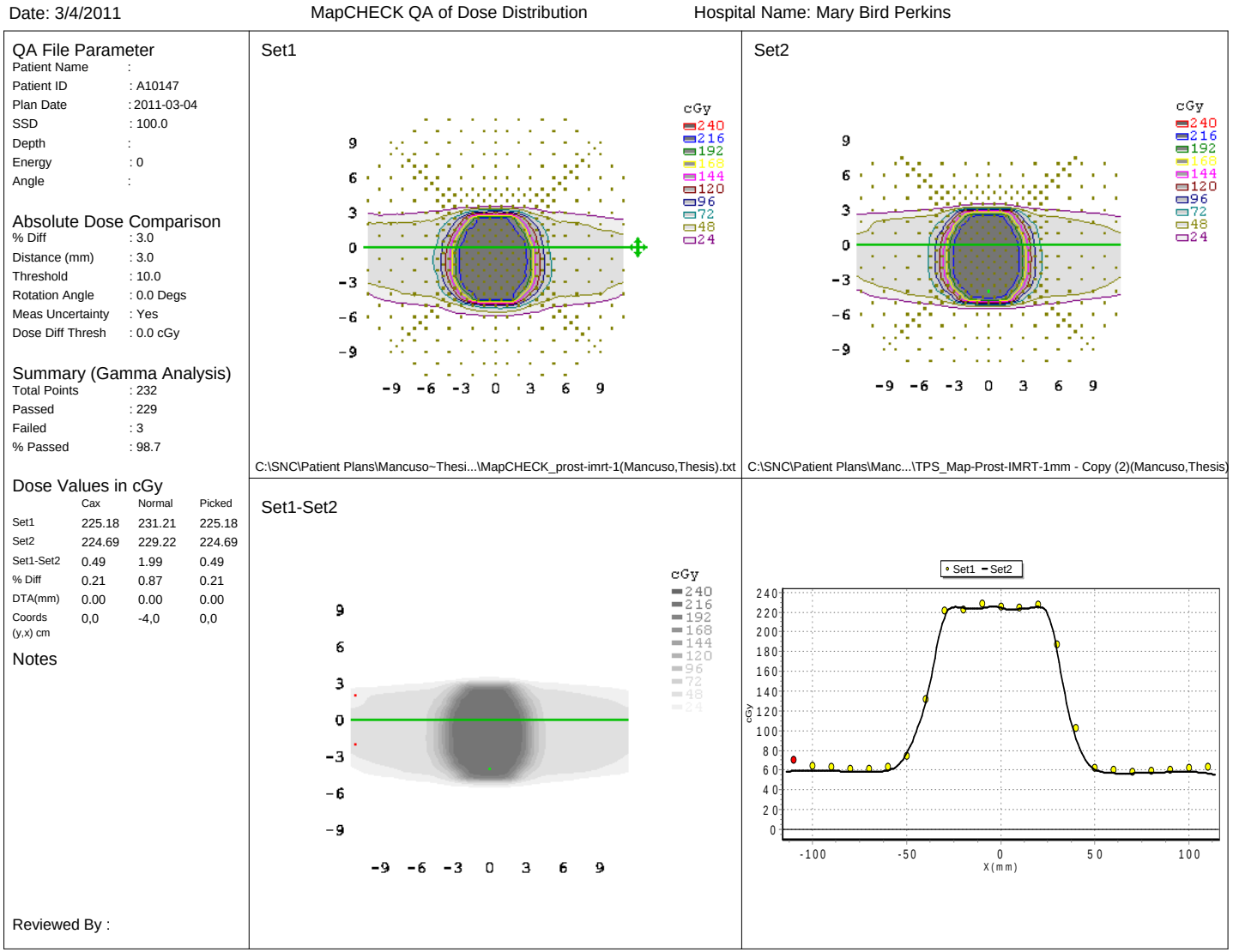

Figure 3.15: Representative MapCHECK output for a prostate IMRT delivery.

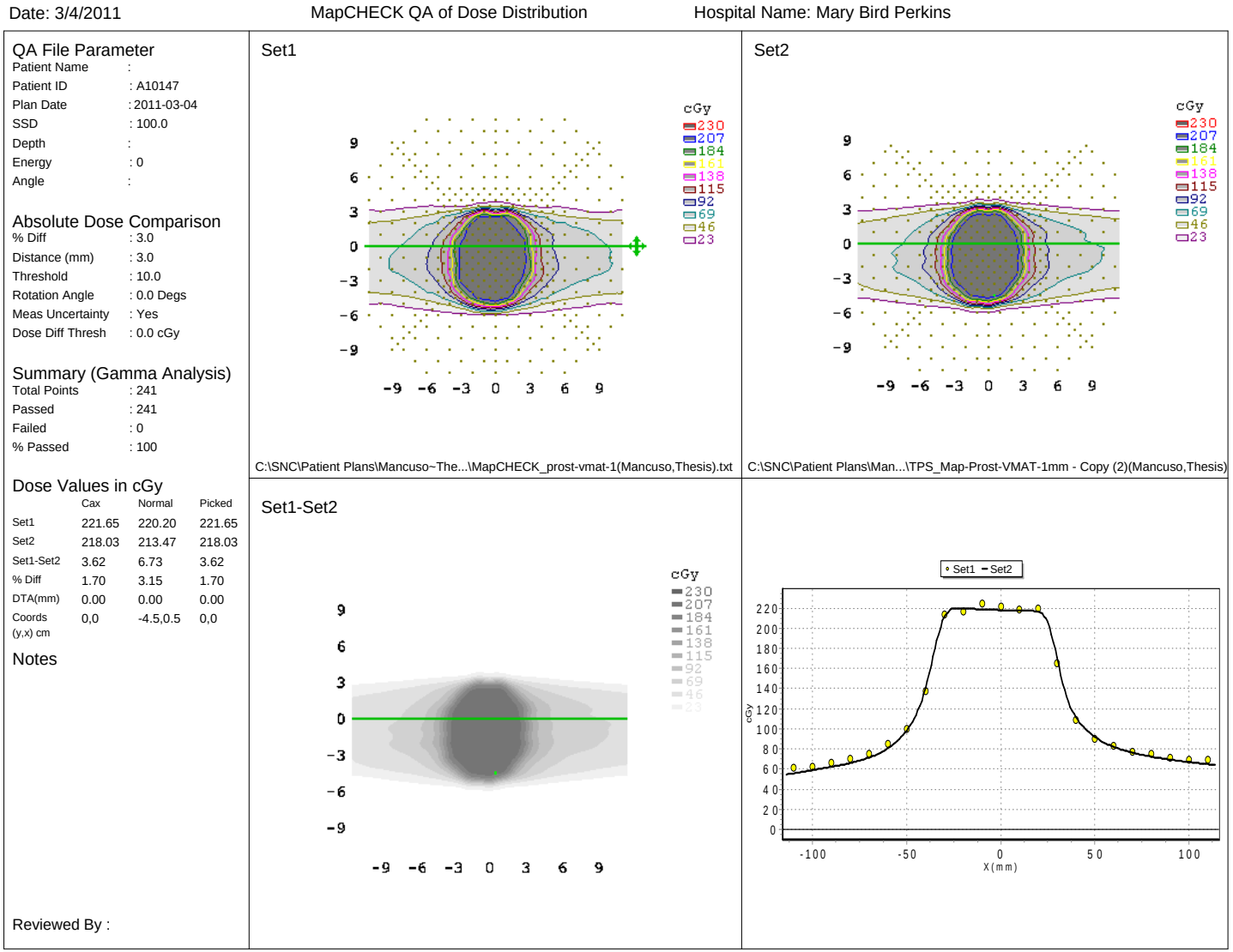

Figure 3.16: Representative MapCHECK output for a prostate VMAT delivery.

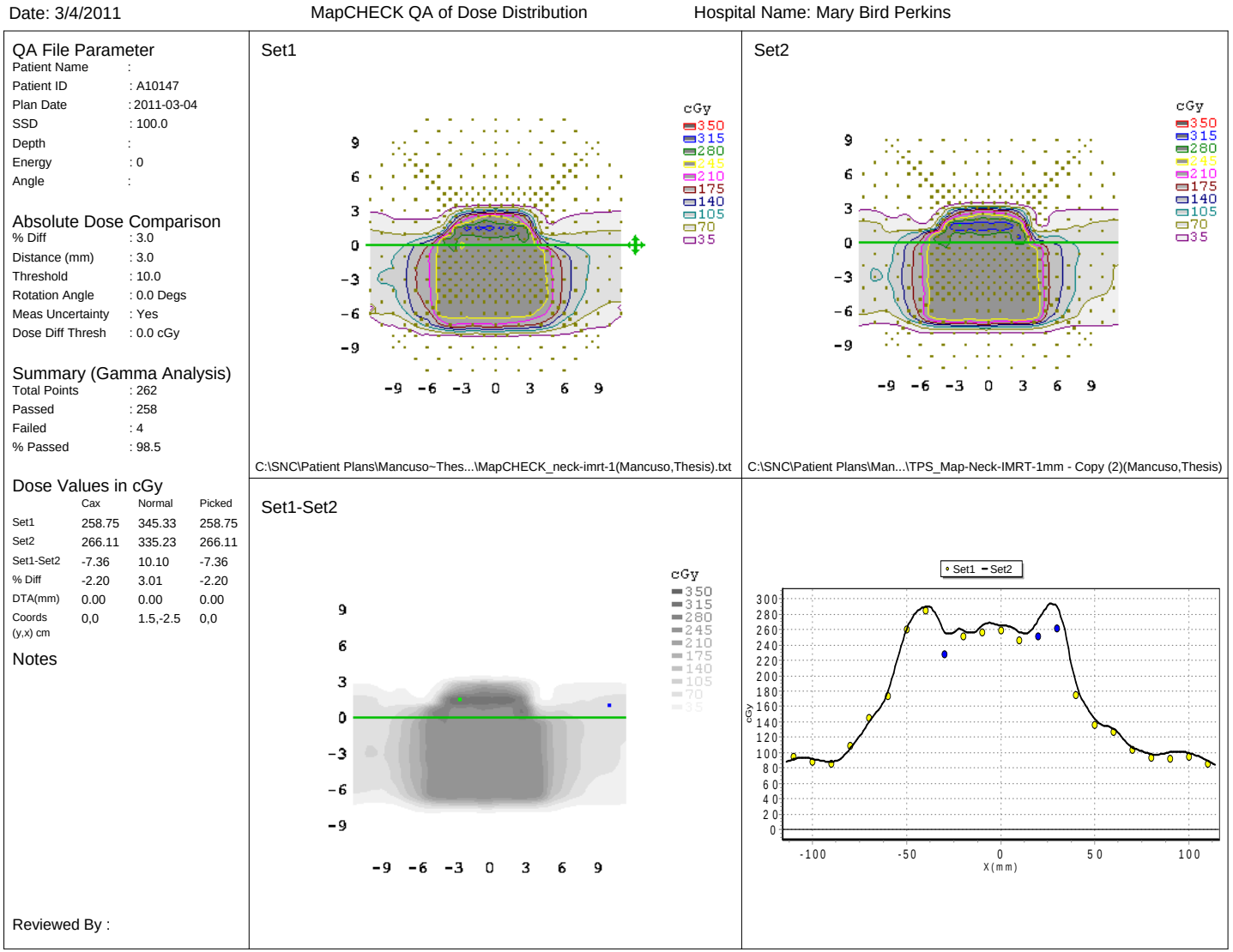

Figure 3.17: Representative MapCHECK output for a head and neck IMRT delivery.

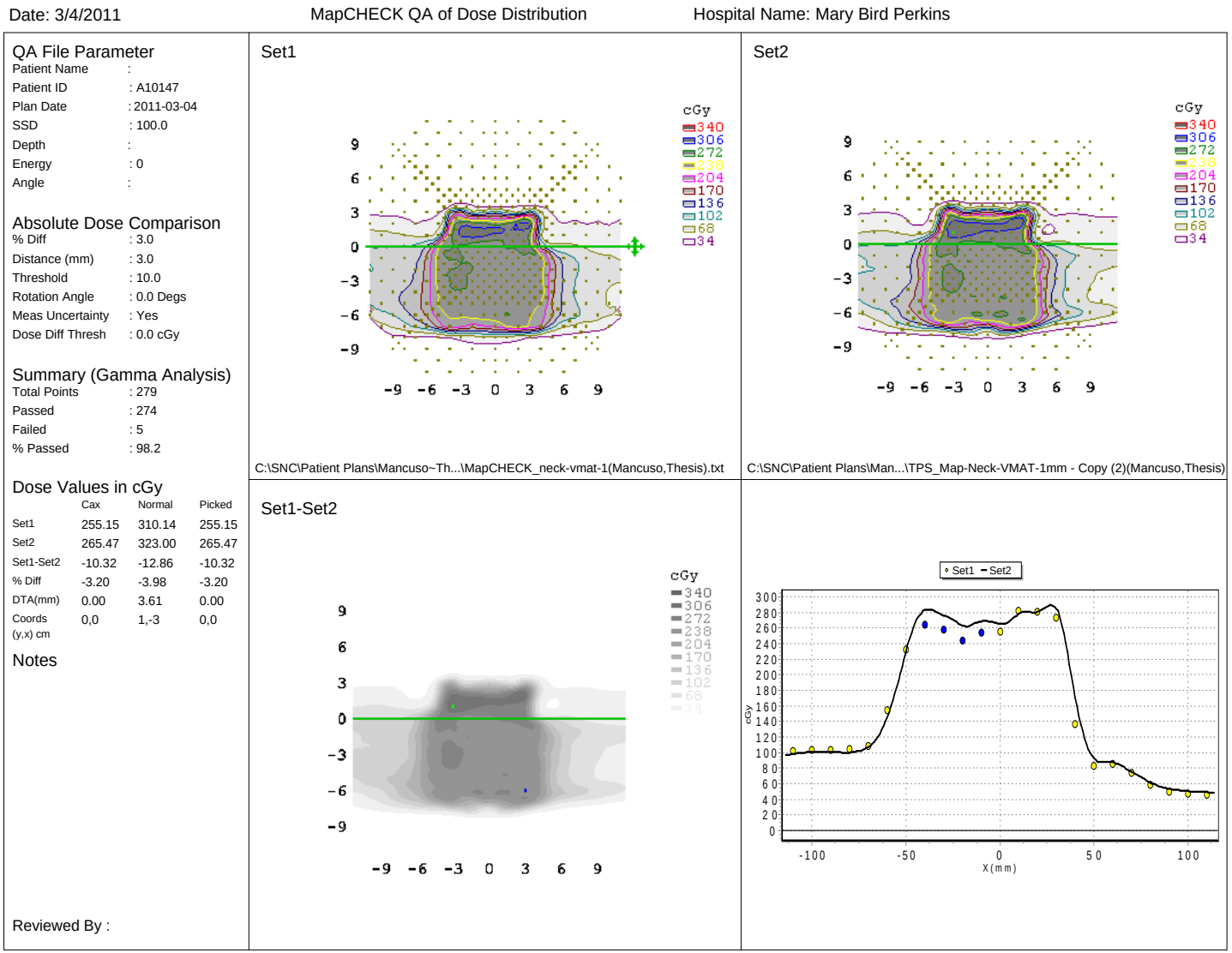

Figure 3.18: Representative MapCHECK output for a head and neck VMAT delivery.

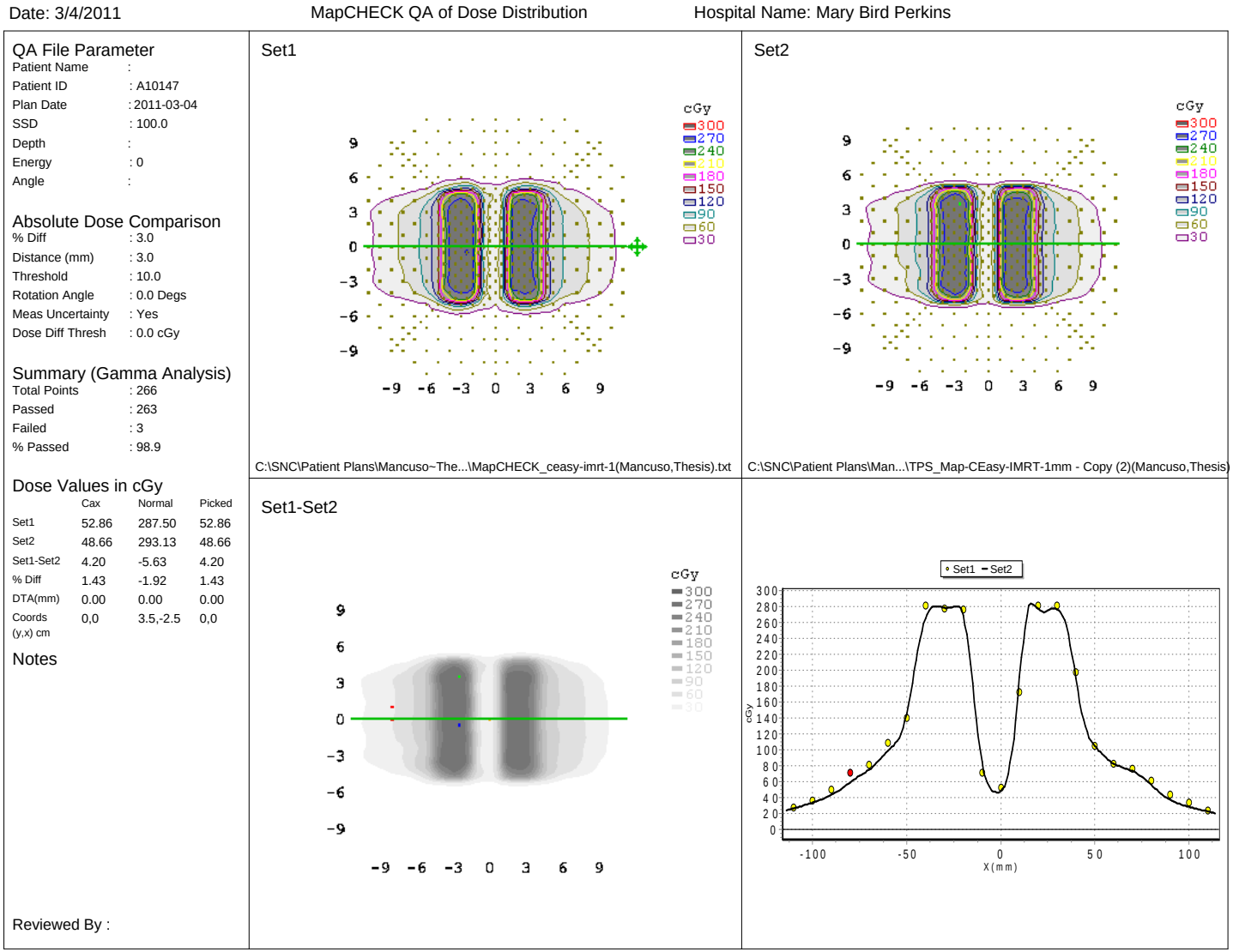

Figure 3.19: Representative MapCHECK output for a C-shape IMRT delivery.

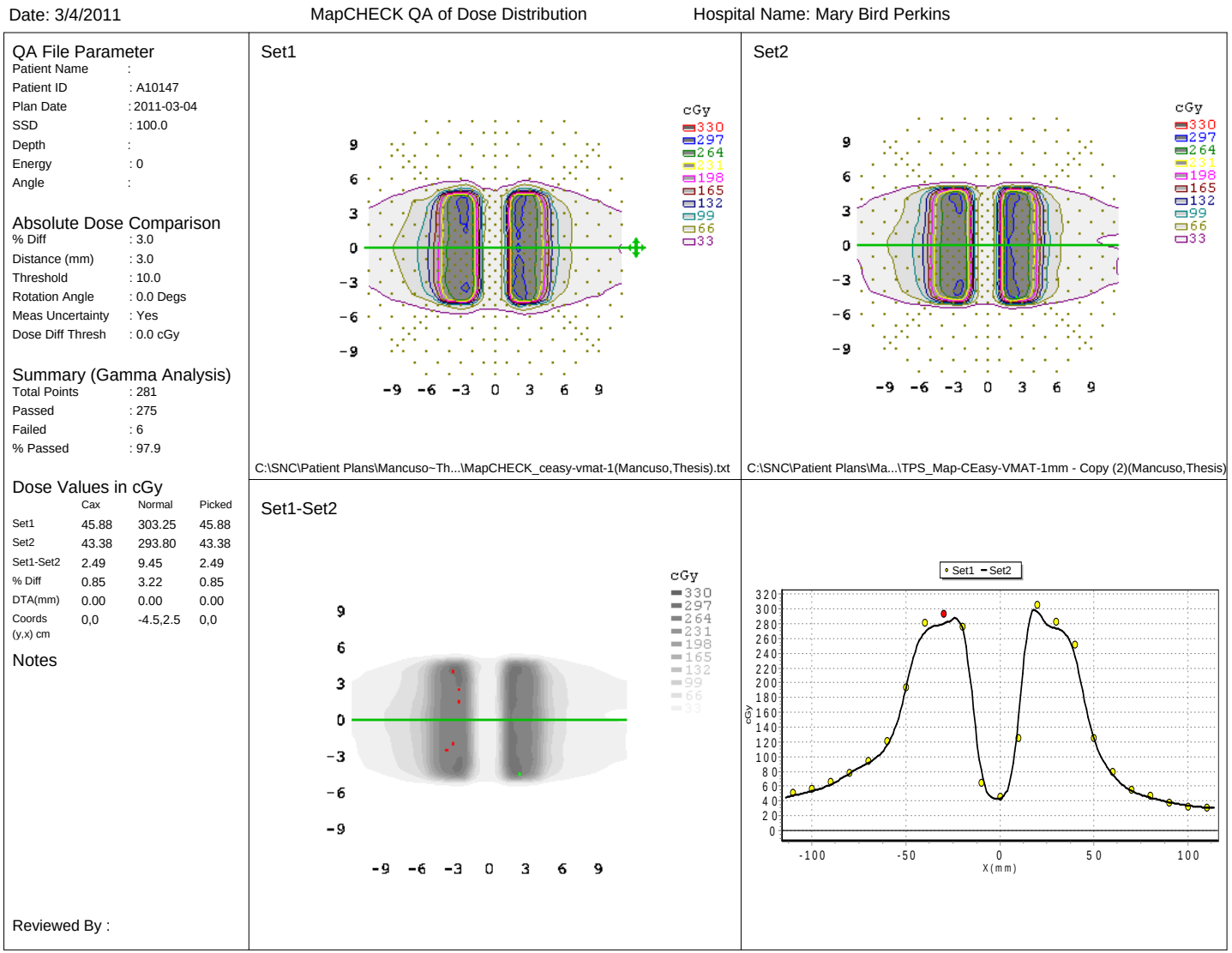

Figure 3.20: Representative MapCHECK output for a C-shape VMAT delivery.

3.5 Data Summary

For all three types of measurements, the global comparisons between IMRT and VMAT QA results showed statistically insignificant differences ($p > 0.05$).

For site-specific point dose measurements, IMRT QA showed significantly better agreement in five cases, VMAT QA showed significantly better agreement in four cases, and VMAT showed insignificantly better agreement in one case. For site-specific diode array measurements, IMRT QA showed significantly better agreement in one case, VMAT QA showed significantly better agreement in one case, and IMRT showed insignificantly better agreement in two cases. In sum, IMRT QA showed statistically better agreement in six cases, VMAT QA showed statistically better agreement in five cases, and three tested cases gave statistically insignificant differences. For site-specific film measurements, IMRT QA showed better agreement in three cases, and VMAT QA showed better agreement in five. Statistical tests were not performed on the film site-specific cases.

Chapter 4

Discussion

In this work, we performed a comprehensive investigation comparing VMAT and IMRT patient specific QA using film, ion chamber, and 2D diode array measurements. Global comparisons between IMRT and VMAT QA results showed no statistically significant differences. The largest observed difference was in the point dose data, but even that difference was not statistically significant ($p > 0.05$). The film and MapCHECK data showed very little difference between the IMRT and VMAT QA results. These results support the hypothesis that IMRT and VMAT QA results are not significantly different.

Although we did not observe significant differences between global IMRT and VMAT QA results, we did observe statistically significant differences for some site-specific measurements, as seen in Tables 3.4 and 3.10. However, if we further examine the number of cases in which each modality had better agreement, we find that roughly half of the data points demonstrated IMRT as having better agreement and roughly half showed VMAT as having better agreement. This suggests that, while one modality may show better agreement in specific cases, on the whole, neither IMRT nor VMAT QA shows better agreement than the other.

One of the important concepts in this work is the idea of clinical significance. Statistical significance is easily defined by choosing an appropriate significance level for a given statistical test. Clinical significance, however, is a more subjective determination of whether a difference has an impact on the day-to-day workings in the clinic. Clinical significance may be present even if no statistical significance is found, and vice versa. This is important because our data showed a difference between the IMRT and VMAT point dose means. The result was not statistically significant ($p > 0.05$), but additional measurement locations could possibly increase the statistical significance. However, the mean results of the IMRT and VMAT point dose measurements differed by less than 1%, which is a small

value compared to the standard deviations of the measurements associated with the two modalities. In addition to this, the typical action level for point dose measurements in our clinic is a 3% difference, and can be even larger in the case of complex treatments. Our measured mean IMRT and VMAT point dose measurements were well below this 3% level. This suggests that there was not a clinically significant difference between the IMRT and VMAT point dose measurements. This same argument can be applied to the film and diode array data, which showed even less of a difference between modalities than the point dose data.

4.1 Comparison to Previous Work

As stated in the introduction, this work was the first comprehensive comparison of IMRT QA and VMAT QA. Other investigators have performed QA on IMRT and VMAT plans, but this work focused on verifying the repeatability of the measurements and on standardizing the QA methods to be as similar as possible for each modality.

Jursinic, Sharma, and Reuter (2010) reported MapCHECK and MapPHAN passing rates of 99.5% for a fixed-beam IMRT plan and 99.8% for RapidArc plans, using criteria of 3%/3 mm. These results are similar to our MapCHECK results of 98.67% and 98.59% for IMRT and VMAT, respectively.

Masi et al. (2011) examined two different planning systems and several different measurement devices for VMAT QA. The mean passing rates for 36 EBT2 film measurements and 25 MapCHECK in MapPHAN measurements were 91.3% and 96.9%, respectively. The passing rates in our study were higher than these, especially for the EBT2 QA. We may attribute this to our method of digitization and normalization of the EBT2 film, which differed from Masi et al, who used a flatbed scanner and absolute dose calibration for their film. They also measured point doses using an Exradin A16 ion chamber for 50 VMAT plans, and reported a mean point dose difference and standard deviation of 1.1% ± 1.0%. The magnitude of this mean difference is similar to the mean dose difference of −1.71% that we found in our study.

Table 4.1: Individual institution point dose results from TG 119. Percent differences for high and low dose locations reported by each institution are included, along with their standard deviations.

Institution	High dose mean (%)	High dose St. Dev. (%)	Low dose mean (%)	Low dose St. Dev. (%)
A	−0.4	2.3	−0.6	0.7
B	−1.2	2.1	−1.0	1.8
C	−0.6	1.1	0.6	3.4
D	−0.7	0.4	1.3	0.6
E	−1.7	1.4	−0.5	1.3
F	0.2	1.2	n/a	n/a
G	−1.3	4.4	−0.5	0.5
H	−1.4	0.4	0.8	2.4
I	−0.9	3.0	−0.8	1.4
J	0.8	1.9	4.5	2.1

The TG 119 results were reported in Table 1.1 (Ezzell et al. 2009). We noticed a few differences when comparing our results to the TG 119 results. First, the mean point dose differences we found for IMRT and VMAT were both somewhat less than zero (−0.72% and −1.71% for IMRT and VMAT, respectively), while the mean point dose differences from TG 119 were nearer zero (−0.2% and 0.3% for high and low dose points, respectively). This may be explained by examining the individual institution results shown in the TG 119 report (see Table 4.1). Some institutions showed mean point dose results above or below zero, similar to ours. However, when results from all the institutions were averaged together, the mean difference converged to zero. Moreover, the standard deviations of our point dose results (1.50% and 1.77% for IMRT and VMAT, respectively) were similar to the standard deviations reported by other institutions. Thus, we conclude that our point dose results are consistent with those of the TG 119 institutions.

Second, our film results and diode array results had higher passing rates and smaller standard deviations than the TG 119 composite film results. We observed passing rates of 98.9% ± 1.0% and 99.1% ± 0.8% for IMRT and VMAT film results, and 98.7% ± 0.5% and 98.6% ± 0.8% for IMRT and VMAT MapCHECK results, while the mean composite

Table 4.2: Individual institution composite film results from TG 119. The mean percent of pixels passing gamma using 3%/3 mm criteria is reported for each institution that took composite film measurements. The standard deviation reported by each institution is also shown.

Institution	Mean % passing γ	St. Dev.
A	99.5	0.4
B	92.6	4.3
D	99.9	0.3
E	97.6	2.3
F	98.0	1.1
G	93.0	6.5
I	95.8	3.6
J	97.5	2.9

film passing rate from TG 119 was 96.3% ± 4.4%. Like the point dose results, our results exhibited characteristics similar to the film results reported by individual institutions in TG 119 (see Table 4.2).

4.2 Possible Limitations of the Work

There were some limitations in this work, which are discussed here. One limitation of this work was that it focused on one specific institution's implementations of IMRT and VMAT. It is possible that other institutions may find larger differences between IMRT and VMAT QA (Kisling 2010). However, the results found here show that it is reasonable for IMRT and VMAT QA to give comparable results. Further work by other institutions may increase the confidence of this assessment.

Another limitation arises from the finite size of the ion chamber used for point dose measurements. The A1SL ion chamber has a volume of 0.057 cc, which corresponds to dimensions of roughly 4 mm on a side. This is a non-negligible size when striving for millimeter placement accuracy. To investigate the potential effect of volume averaging, planar dose files were exported from Pinnacle[3] at the locations of the different dose points, in both coronal and sagittal orientations. We examined the area surrounding the point dose measurement locations to observe the approximate dose gradients. In high dose, low

gradient regions, the observed dose gradients were on the order of 1 cGy/mm. However, in the lower dose regions (specifically, at the points in the OAR structures), dose gradients of 3–5 cGy/mm were observed. These gradients are significant, and mean that different parts of the chamber likely received significantly different doses when measuring those point doses.

These significant dose gradients also have the potential to cause larger dose errors in the associated point dose measurements, because very small positional errors can cause large dose differences. Table 3.4 shows that the standard deviations for some of the low dose points were larger than the standard deviations for the high dose points, which could be due to the higher dose gradient at those points. However, the standard deviations were still much smaller than the observed dose gradients of 3–5 cGy/mm, which indicates that the inter-measurement ion chamber placement positional error was less than 1 mm. This indicates a high precision of ion chamber placement. However, the high dose gradient might still be responsible for the lower agreement seen in some of the low dose points if there were systematic errors in the placement of the chamber.

One other possible limitation may have been a systematic shift seen in the film data when compared to the exported planar dose data. This shift can be seen in Fig. 4.1. Looking at the dose profiles for these film measurements, a 1–2 mm shift in the y-direction can be seen. This may suggest a limitation in the registration procedure for the irradiated films. A similar shift was observed in almost every film analyzed. We investigated several possible causes for this shift, but did not find a source of the error. One possible remaining explanation is that the shift was due to the CT scan slice size. The CT scan of the cylindrical phantom was taken with a 2.5 mm slice size. The center of the cylindrical phantom is defined by a set of intersecting lines machined onto the phantom (see Fig. 2.6). To indicate the location of the center line on the CT scan, three radiopaque markers were placed on the cylindrical phantom before the CT scan. These markers were visible on the CT scan and indicated the location of the isocenter. Since these markers could be located anywhere in

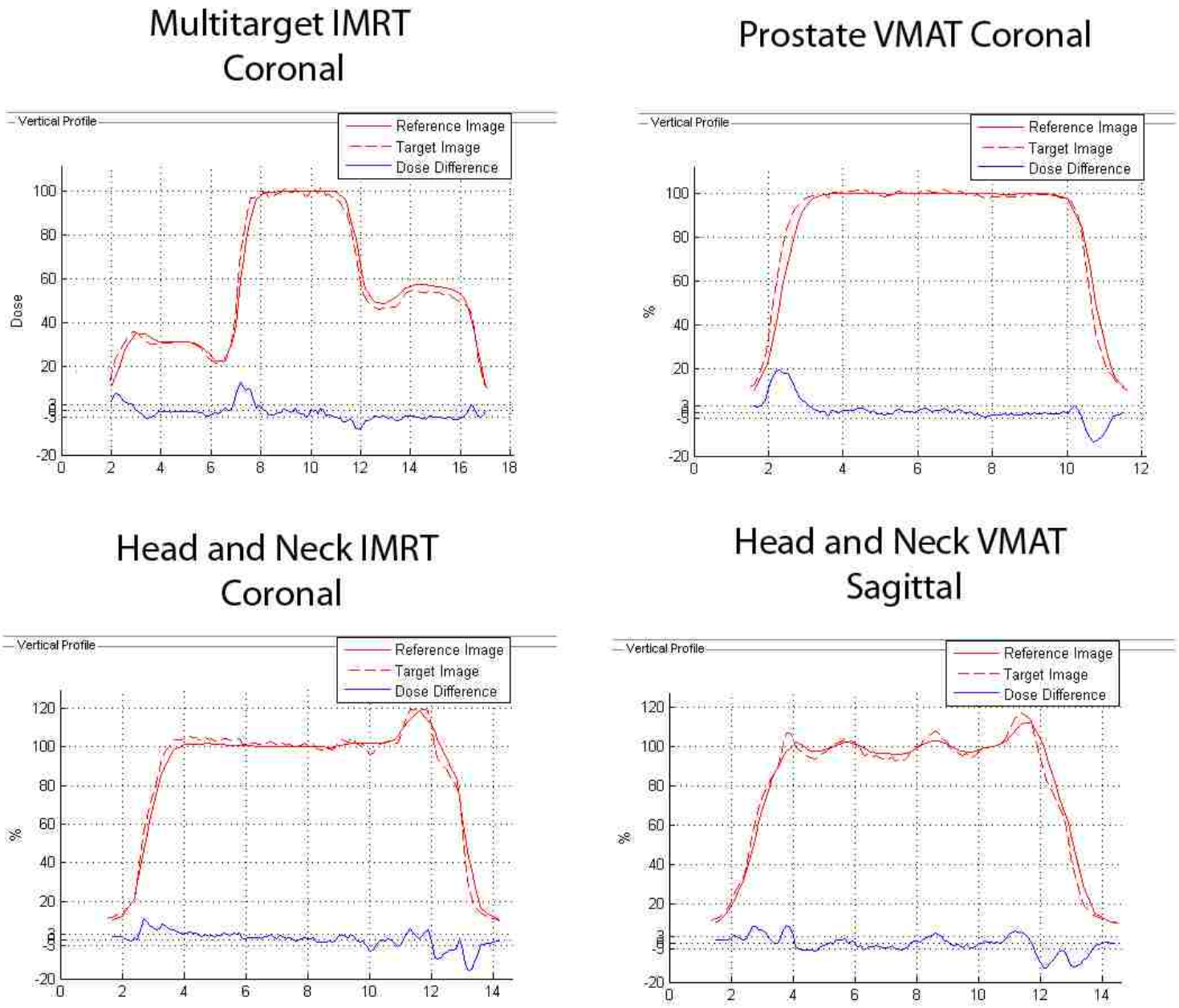

Figure 4.1: Vertical film profiles displaying a systematic shift. In each of these cases, a systematic 1–2 mm shift can be seen between the film (dotted line) and the exported planar dose data (solid line).

the 2.5 mm slice in which they appeared, there is no guarantee that the isocenter defined in Pinnacle[3] is at the exact same location as the actual isocenter of the phantom. This could be the source of the systematic shift in the longitudinal direction. Further testing, including repeating the CT scan of the cylindrical phantom, may be able to verify whether this was the cause of the systematic shift. Regardless of the cause, this shift was seen in almost all film measurements, and so would have a similar effect on both IMRT and VMAT data, and thus should not affect the comparisons.

4.2.1 Normality

One method to increase the power of the statistical tests would be to use a Student's t-test instead of a Wilcoxon rank-sum test. The rank-sum test does not assume normality of the underlying data, while the t-test does. This assumption gives the t-test more power to determine significance. However, if the assumption is false, then the additional power is not justified. To investigate the possibility of using the t-test, histograms were created to assess the normality of the data.

Two different kinds of histograms were constructed to investigate normality of the data for the two different statistical comparisons that were made (see Sec. 2.4.5). To investigate the normality of the data for the site-specific comparisons, the measured data was first transformed by subtracting the mean value of the site from each measurement. For an example, see Table 4.3. Here are listed the five MapCHECK measurements for the

Table 4.3: Site-specific normality check: Data transformation. For each set of repeated measurements, the mean of the set was subtracted from each measurement. This is an example transformation for the C-shape IMRT MapCHECK data.

% diodes passing γ criteria=3%/3 mm	Mean	Measurement minus mean
98.87		0.75
97.74		−0.38
98.50	98.12	0.38
97.74		−0.38
97.74		−0.38

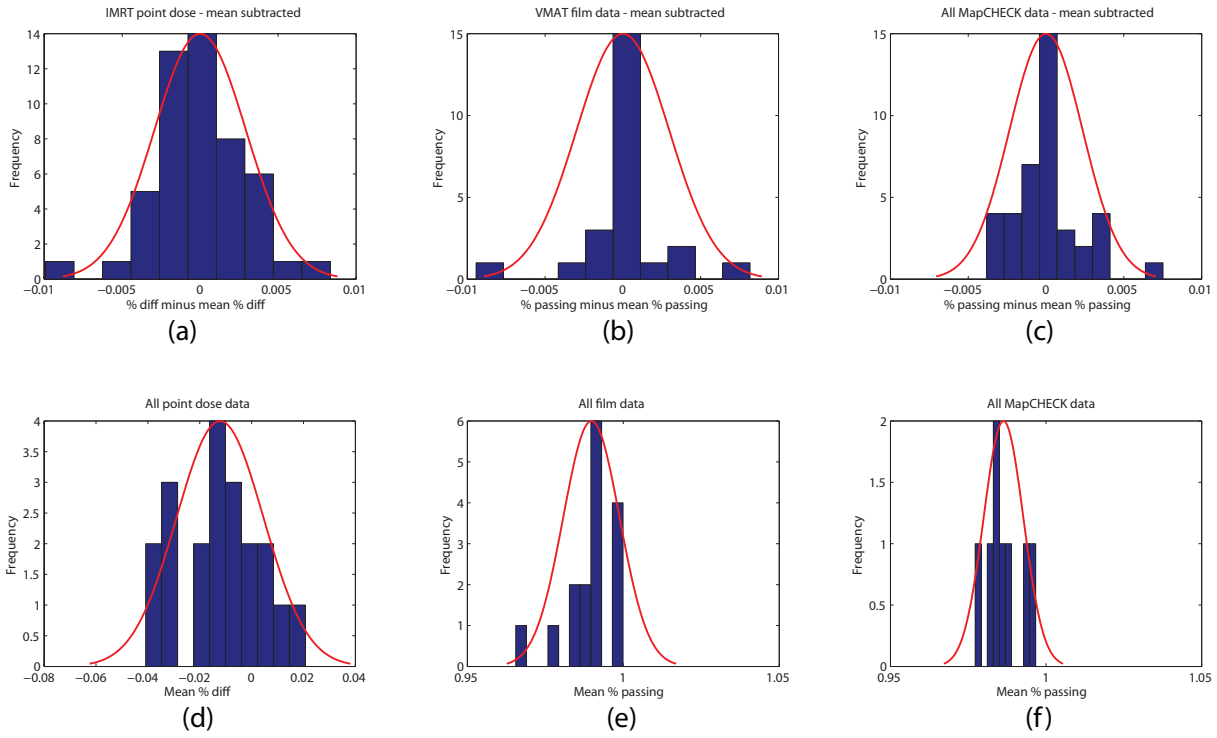

Figure 4.2: Normality histograms. Plots (a–c) are histograms of data with the site-specific means subtracted, and plots (d–f) are histograms of site-specific means. Plots (a–c) are IMRT point dose, VMAT film, and combined IMRT and VMAT MapCHECK data, respectively; plots (d–f) are combined data for point dose, film, and MapCHECK measurements, respectively. In each plot, a Gaussian line with mean and standard deviation equal to the given data is plotted for comparison.

C-shape IMRT delivery. The mean of these five measurements was subtracted from each measurement. The purpose was to isolate the values that represent the inter-measurement variations. This process was repeated for every measurement for each measurement type, and the results were plotted in histograms for each measurement type and modality.

To investigate the normality of the data for global comparisons, the mean results of the repeated measurements for each measurement setup were plotted in histograms.

Some of the histograms created are displayed in Fig. 4.2. Based on these results and other similar plots (not shown), we decided that we could not conclude a normal underlying distribution. While some plots suggested possible normality, others did not, and there did not seem to be enough data points to confidently conclude that the data was normally distributed. As such, we chose to use the Wilcoxon rank-sum test. While this resulted in a

less powerful statistical test, we are confident that we did not violate any assumptions of the test.

4.3 Further Work

This work focused on using a standard set of geometries that has previously been used and given credence by AAPM TG 119. In order to ensure reproducibility of the data, each measurement was taken several times. A further study could be conducted that includes more plans (but perhaps with fewer measurements per plan), especially clinical plans. This would give more data points for the statistical tests comparing VMAT and IMRT data. However, it must be remembered that differences, even if found to be statistically significant, may not carry clinical significance if they are small. If this further work were performed at another institution and showed results similar to ours, it would increase our confidence further that there is no clinical difference between IMRT and VMAT QA.

Chapter 5

Conclusion

In this study, we investigated differences between fixed-beam IMRT and VMAT patient specific QA. IMRT and VMAT plans were constructed for four structure set geometries provided in AAPM Task Group Report 119, *viz.*: multitarget, mock prostate, mock head and neck, and C-shape. The plans were delivered by a linear accelerator to phantom geometries, and the resulting dose distribution was measured using ion chamber, radiochromic film, and a 2D diode array. Each measurement was repeated several times to verify reproducibility of the results. The average percent differences between measured and calculated point doses were less than 2% for both IMRT and VMAT treatments, and both film and diode array measurements yielded averages of better than 98% of pixels/diodes passing the gamma test for both IMRT and VMAT treatments.

Statistical analysis of the aggregate IMRT and VMAT QA results showed no statistically significant differences between the two delivery techniques. These results suggest that it is appropriate to apply IMRT QA methods and action levels to VMAT QA.

References

Andrés, C., A. del Castillo, R. Tortosa, D. Alonso, and R. Barquero. 2010. "A comprehensive study of the Gafchromic EBT2 radiochromic film. A comparison with EBT." *Medical Physics* 37 (12): 6271–6278.

Arbea, Leire, Luis Isaac Ramos, Rafael Martínez-Monge, Marta Moreno, and Javier Aristu. 2010. "Intensity-modulated radiation therapy (IMRT) vs. 3D conformal radiotherapy (3DCRT) in locally advanced rectal cancer (LARC): dosimetric comparison and clinical implications." *Radiation Oncology* 5:17.

Bedford, James L, Young K Lee, Philip Wai, Christopher P South, and Alan P Warrington. 2009. "Evaluation of the Delta4 phantom for IMRT and VMAT verification." *Physics in Medicine and Biology* 54 (9): N167–76.

Bortfeld, T., W. Schlegel, K.-H. Höver, and D. Schulz-Ertner. 1999. "Mini and Micro Multileaf Collimators." *41st AAPM National Meeting*. 1–9.

Buonamici, F. Banci, A. Compagnucci, L. Marrazzo, S. Russo, and M. Bucciolini. 2007. "An intercomparison between film dosimetry and diode matrix for IMRT quality assurance." *Medical Physics* 34 (4): 1372–1379.

Chang, Sha X, Timothy J Cullip, Katharin M Deschesne, Elizabeth P Miller, and Julian G Rosenman. 2004. "Compensators: An alternative IMRT delivery technique." *Journal of Applied Clinical Medical Physics* 5 (3): 15–36.

Childress, Nathan L., Lei Dong, and Isaac I. Rosen. 2002. "Rapid radiographic film calibration for IMRT verification using automated MLC fields." *Medical Physics* 29 (10): 2384–2390.

Earl, M A, D M Shepard, S Naqvi, X A Li, and C X Yu. 2003. "Inverse planning for intensity-modulated arc therapy using direct aperture optimization." *Physics in Medicine and Biology* 48 (8): 1075–1089.

Ezzell, G. A., J. W. Burmeister, N. Dogan, T. J. LoSasso, J. G. Mechalakos, D. Mihailidis, A. Molineu, J. R. Palta, C. R. Ramsey, B. J. Salter, J. Shi, P. Xia, N. J. Yue, and Y. Xiao. 2009. "IMRT commissioning: Multiple institution planning and dosimetry comparisons, a report from AAPM Task Group 119." *Medical Physics* 36 (11): 5359–5373.

Harms, William B., Daniel A. Low, John W. Wong, and James A. Purdy. 1998. "A software tool for the quantitative evaluation of 3D dose calculation algorithms." *Medical Physics* 25 (10): 1830–1836.

International Specialty Products. 2009. Gafchromic EBT2 technical brief.

———. 2010. GAFCHROMIC EBT2 Dosimetry Film product specifications.

Ju, Tao, Tim Simpson, Joseph O. Deasy, and Daniel A. Low. 2008. "Geometric interpretation of the γ dose distribution comparison technique: Interpolation-free calculation." *Medical Physics* 35 (3): 879–887.

Jursinic, Paul A., Renu Sharma, and Jim Reuter. 2010. "MapCHECK used for rotational IMRT measurements: Step-and-shoot, Tomotherapy, RapidArc." *Medical Physics* 37 (6): 2837–2846.

Khan, Faiz M. 2010. *The Physics of Radiation Therapy*. 4th ed. Philadelphia: Lippincott Williams & Wilkins.

Kisling, Kelly. 2010. "Volumeric Modulated Arc Therapy Evaluation with the Radiological Physics Center Head and Neck Phantom." Ph.D. diss., UT Houston.

Korreman, Stine, Joakim Medin, and Flemming Kjaer-Kristoffersen. 2009. "Dosimetric verification of RapidArc treatment delivery." *Acta Oncologica* 48 (2): 185–191.

Kruse, Jon J. 2010. "On the insensitivity of single field planar dosimetry to IMRT inaccuracies." *Medical Physics* 37 (6): 2516–2524.

Létourneau, Daniel, Misbah Gulam, Di Yan, Mark Oldham, and John W. Wong. 2004. "Evaluation of a 2D diode array for IMRT quality assurance." *Radiotherapy and oncology* 70 (2): 199–206.

Low, Daniel A., and James F. Dempsey. 2003. "Evaluation of the gamma dose distribution comparison method." *Medical Physics* 30 (9): 2455–2464.

Low, Daniel A., William B. Harms, Sasa Mutic, and James A. Purdy. 1998. "A technique for the quantitative evaluation of dose distributions." *Medical Physics* 25 (5): 656–661.

Ma, L., C. X. Yu, M. Earl, T. Holmes, M. Sarfaraz, X. A. Li, D. Shepard, P. Amin, S. DiBiase, M. Suntharalingam, and C. Mansfield. 2001. "Optimized intensity-modulated arc therapy for prostate cancer treatment." *International Journal of Cancer* 96 (6): 379–84.

Mackie, T. R., T. Holmes, S. Swerdloff, P. Reckwerdt, J. O. Deasy, J. Yang, B. Paliwal, and T. Kinsella. 1993. "Tomotherapy: A new concept for the delivery of dynamic conformal radiotherapy." *Medical Physics* 20 (6): 1709–19.

Masi, L., F. Casamassima, R. Doro, and P. Francescon. 2011. "Quality assurance of volumetric modulated arc therapy : Evaluation and comparison of different dosimetric systems." *Medical Physics* 38 (2): 612–621.

Nelms, Benjamin E., Heming Zhen, and Wolfgang A. Tome. 2011. "Per-beam, planar IMRT QA passing rates do not predict clinically relevant patient dose errors." *Medical Physics* 38 (2): 1037–1044.

Otto, K., M. Milette, and J. Wu. 2007. "Temporal delivery efficiency of a novel single gantry arc optimization technique for treatment of recurrent nasopharynx cancer." *International Journal of Radiation Oncology, Biology, Physics* 69:S703.

Otto, Karl. 2008. "Volumetric modulated arc therapy: IMRT in a single gantry arc." *Medical Physics* 35 (1): 310–317.

———. 2009. "Letter to the Editor on 'Single-Arc IMRT?'." *Physics in Medicine and Biology* 54 (8): L37–41.

Palma, David, Emily Vollans, Kerry James, Sandy Nakano, Vitali Moiseenko, Richard Shaffer, Michael McKenzie, James Morris, and Karl Otto. 2008. "Volumetric modulated arc therapy for delivery of prostate radiotherapy: comparison with intensity-modulated radiotherapy and three-dimensional conformal radiotherapy." *International Journal of Radiation Oncology, Biology, Physics* 72 (4): 996–1001.

Ramsey, Chester, Scott Dube, and William R. Hendee. 2003. "It is necessary to validate each individual IMRT treatment plan before delivery." *Medical Physics* 30 (9): 2271–2273.

Ramsey, Chester R., Kelly M. Spencer, Rabi Alhakeem, and Adrian L. Oliver. 2001. "Leaf position error during conformal dynamic arc and intensity modulated arc treatments." *Medical Physics* 28 (1): 67–72.

Rao, Min, Wensha Yang, Fan Chen, Ke Sheng, Jinsong Ye, Vivek Mehta, David Shepard, and Daliang Cao. 2010. "Comparison of Elekta VMAT with helical tomotherapy and fixed field IMRT: Plan quality, delivery efficiency and accuracy." *Medical Physics* 37 (3): 1350–1359.

Schreibmann, Eduard, Anees Dhabaan, Eric Elder, and Tim Fox. 2009. "Patient-specific quality assurance method for VMAT treatment delivery." *Medical Physics* 36 (10): 4530–4535.

Shepard, D. M., D. Cao, M. K. N. Afghan, and M. A. Earl. 2007. "An arc-sequencing algorithm for intensity modulated arc therapy." *Medical Physics* 34 (2): 464–470.

Stock, Markus, Bernhard Kroupa, and Dietmar Georg. 2005. "Interpretation and evaluation of the γ index and the γ index angle for the verification of IMRT hybrid plans." *Physics in Medicine and Biology* 50 (3): 399–411.

Van Esch, Ann, Jörg Bohsung, Pekka Sorvari, Mikko Tenhunen, Marta Paiusco, Mauro Iori, Per Engström, Håkan Nyström, and Dominique Pierre Huyskens. 2002. "Acceptance tests and quality control (QC) procedures for the clinical implementation of intensity modulated radiotherapy (IMRT) using inverse planning and the sliding window technique: experience from five radiotherapy departments." *Radiotherapy and Oncology* 65 (1): 53–70.

Verbakel, Wilko F. A. R., Johan P. Cuijpers, Daan Hoffmans, Michael Bieker, Ben J. Slotman, and Suresh Senan. 2009. "Volumetric intensity-modulated arc therapy vs. conventional IMRT in head-and-neck cancer: a comparative planning and dosimetric study." *International Journal of Radiation Oncology, Biology, Physics* 74 (1): 252–259.

Webb, S. 2003. "The physical basis of IMRT and inverse planning." *British Journal of Radiology* 76 (910): 678–689.

Wong, Eugene, Jeff Z Chen, and Jonathan Greenland. 2002. "Intensity-modulated arc therapy simplified." *International Journal of Radiation Oncology, Biology, Physics* 53 (1): 222–235.

Yu, Cedric X. 1995. "Intensity-modulated arc therapy with dynamic multileaf collimation: an alternative to tomotherapy." *Physics in Medicine and Biology* 40:1435–1449.

Yu, Cedric X., X. Allen Li, Lijun Ma, Dongjun Chen, Shahid Naqvi, David Shepard, Mehrdad Sarfaraz, Timothy W. Holmes, Mohan Suntharalingam, and Carl M. Mansfield. 2002. "Clinical implementation of intensity-modulated arc therapy." *International Journal of Radiation Oncology, Biology, Physics* 53 (2): 453–463.

Zabel, A., C. Thilmann, I. Zuna, W. Schlegel, M. Wannenmacher, and J. Debus. 2002. "Comparison of forward planned conformal radiation therapy and inverse planned intensity modulated radiation therapy for esthesioneuroblastoma." *The British Journal of Radiology* 75 (892): 356–361.

Zeidan, Omar A., Stacy Ann L. Stephenson, Sanford L. Meeks, Thomas H. Wagner, Twyla R. Willoughby, Patrick A. Kupelian, and Katja M. Langen. 2006. "Characterization and use of EBT radiochromic film for IMRT dose verification." *Medical Physics* 33 (11): 4064–4072.

Zhu, X. R., P. A. Jursinic, D. F. Grimm, F. Lopez, J. J. Rownd, and M. T. Gillin. 2002. "Evaluation of Kodak EDR2 film for dose verification of intensity modulated radiation therapy delivered by a static multileaf collimator." *Medical Physics* 29 (8): 1687–1692.

Appendix A

Film Images

This appendix includes the remaining film images not shown in Sec. 3.3. The film images shown there consisted of the first film images for each unique combination of geometry, modality, and plane. The following images are the second and third such images.

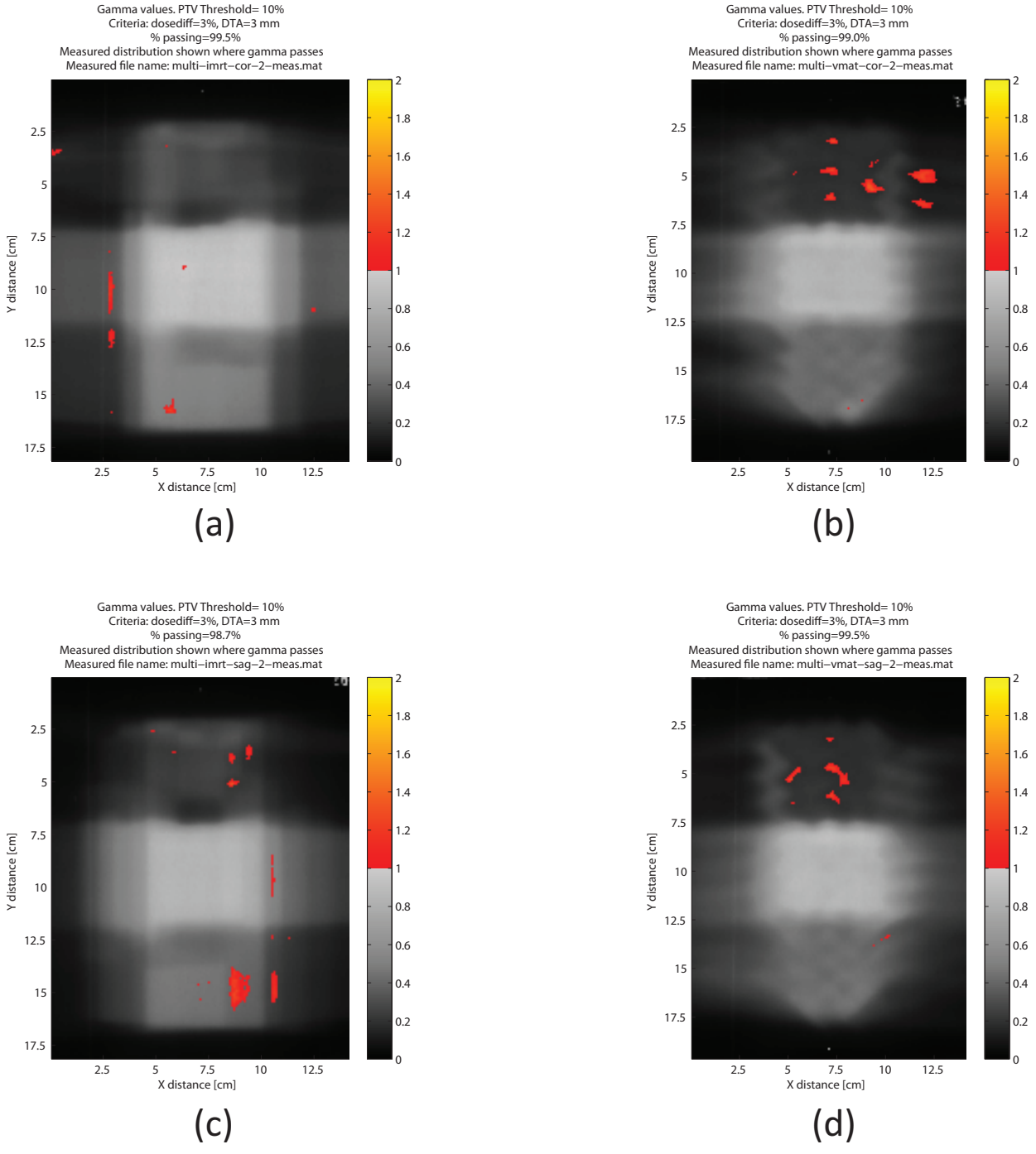

Figure A.1: Second set of gamma results for the multitarget film data. (a) and (b) are the coronal measurements for IMRT and VMAT, respectively; (c) and (d) are the sagittal measurements for IMRT and VMAT, respectively.

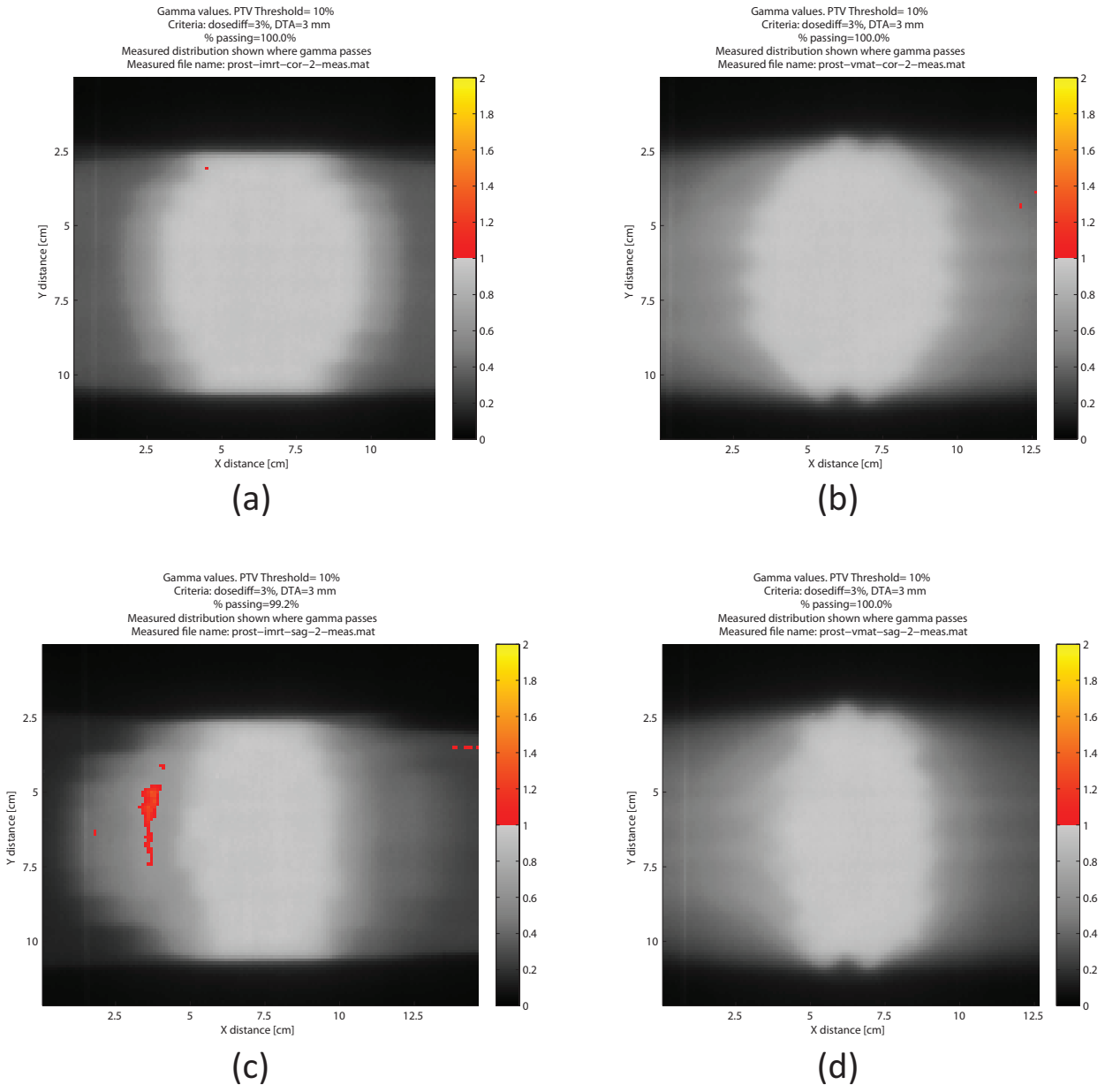

Figure A.2: Second set of gamma results for the prostate film data. (a) and (b) are the coronal measurements for IMRT and VMAT, respectively; (c) and (d) are the sagittal measurements for IMRT and VMAT, respectively.

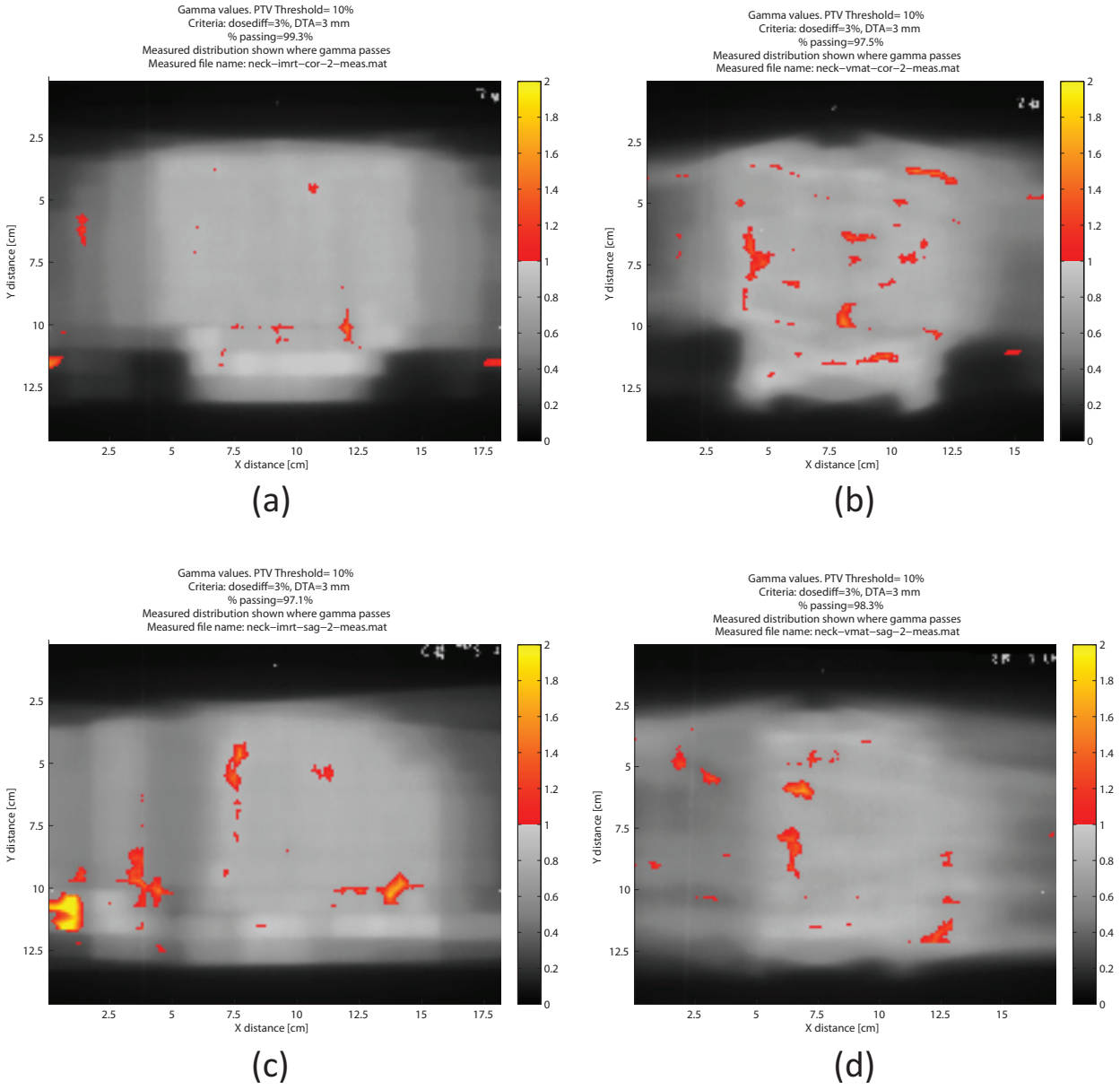

Figure A.3: Second set of gamma results for the head and neck film data. (a) and (b) are the coronal measurements for IMRT and VMAT, respectively; (c) and (d) are the sagittal measurements for IMRT and VMAT, respectively.

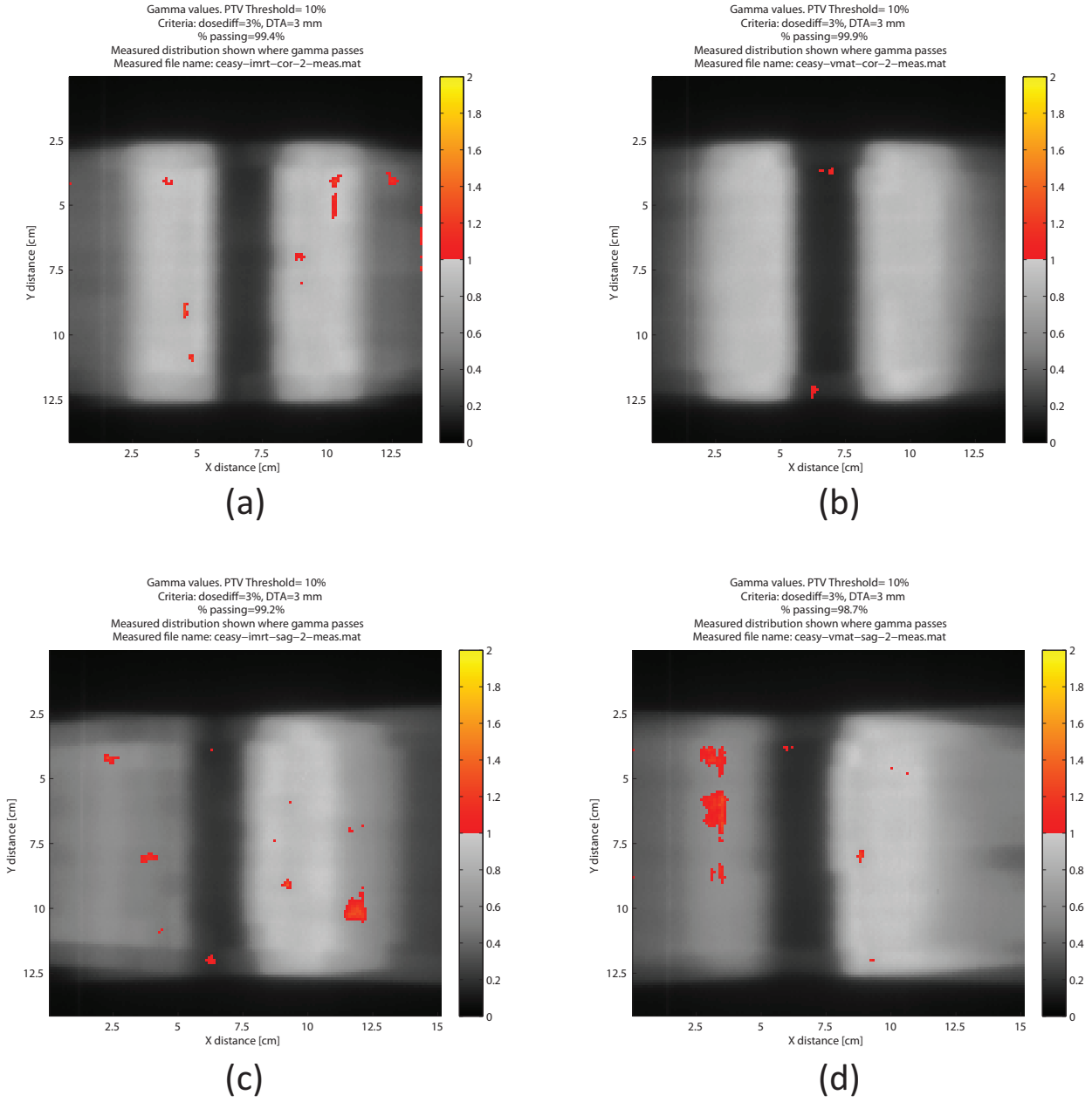

Figure A.4: Second set of gamma results for the C-shape film data. (a) and (b) are the coronal measurements for IMRT and VMAT, respectively; (c) and (d) are the sagittal measurements for IMRT and VMAT, respectively.

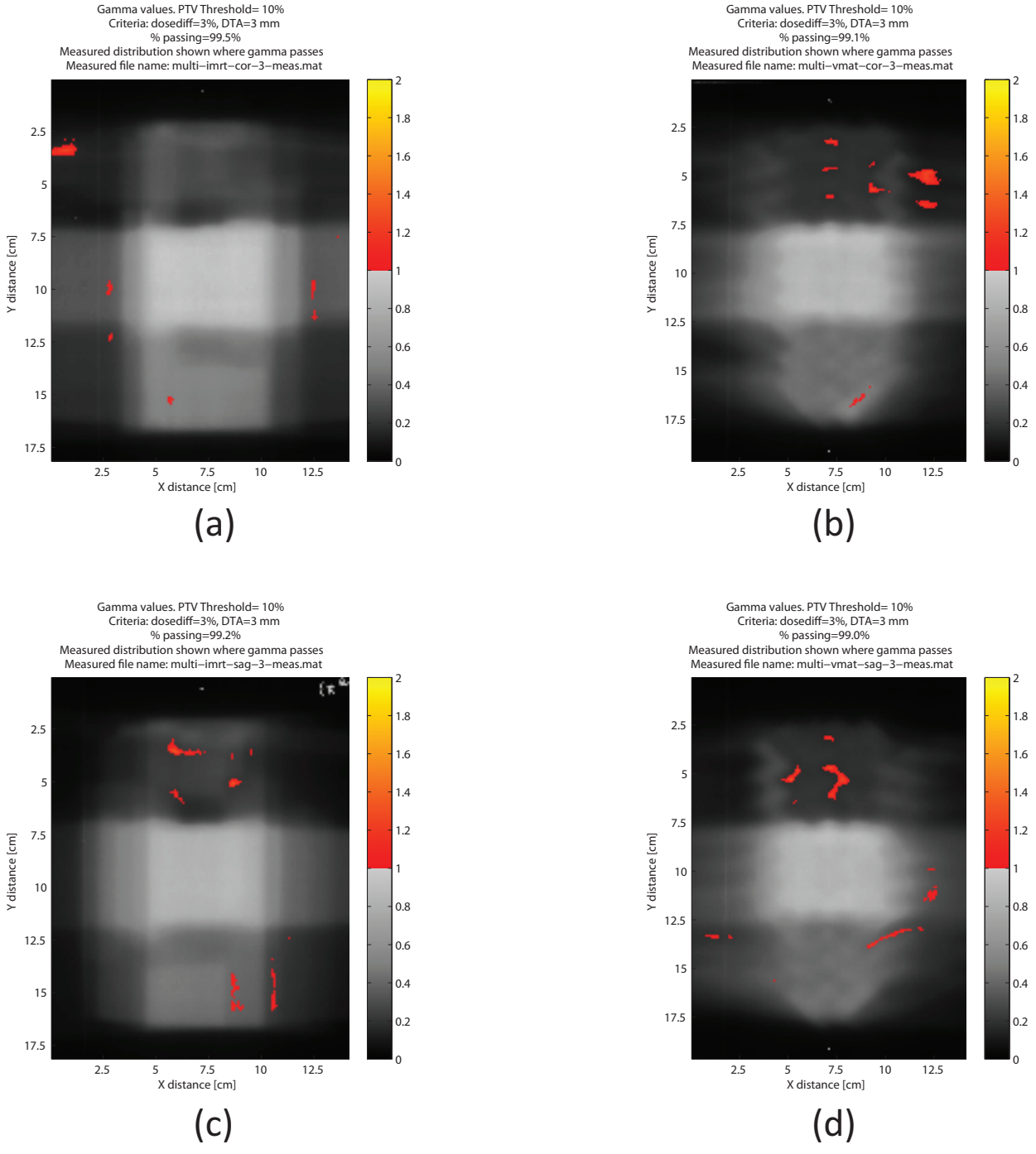

Figure A.5: Third set of gamma results for the multitarget film data. (a) and (b) are the coronal measurements for IMRT and VMAT, respectively; (c) and (d) are the sagittal measurements for IMRT and VMAT, respectively.

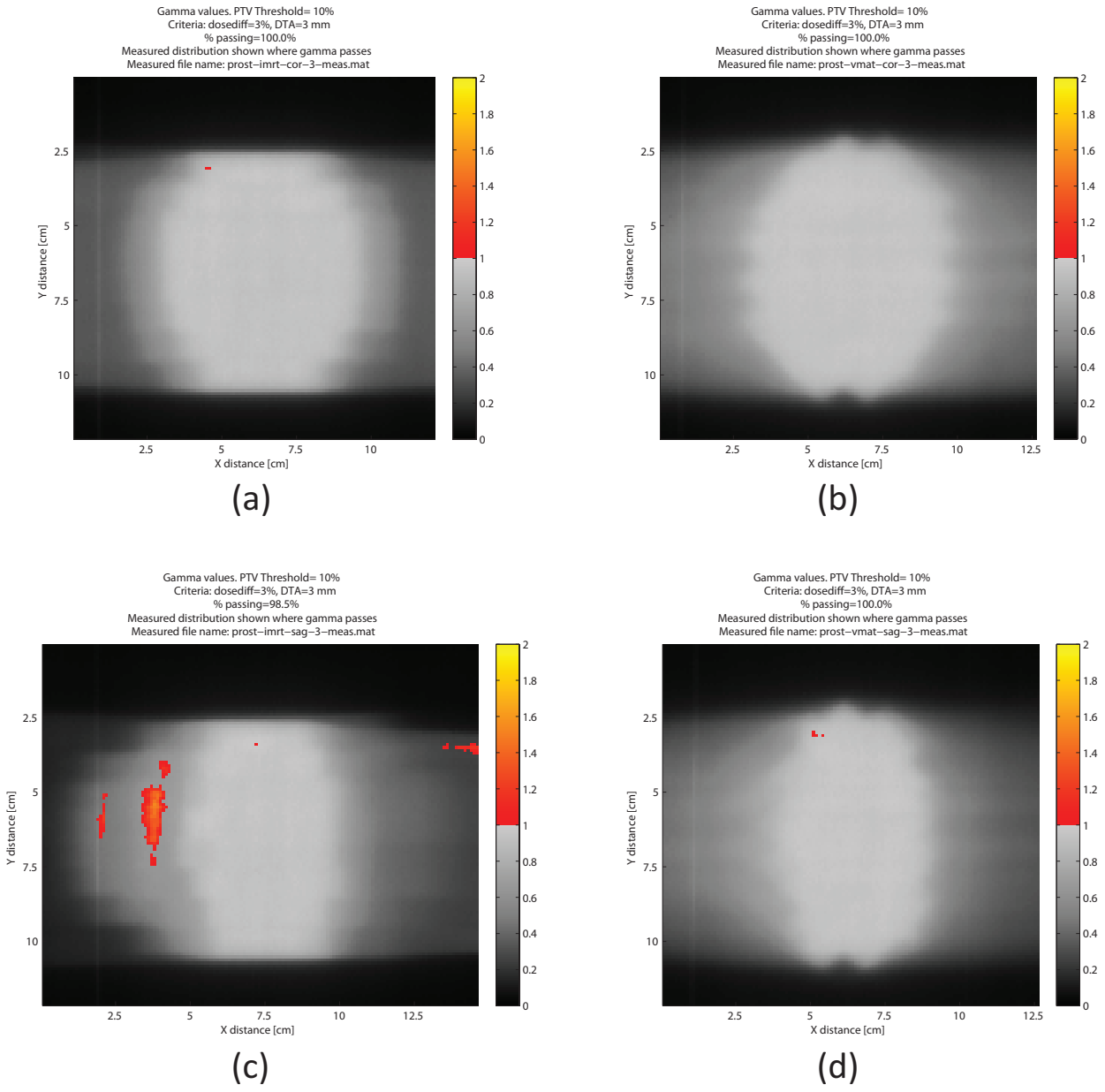

Figure A.6: Third set of gamma results for the prostate film data. (a) and (b) are the coronal measurements for IMRT and VMAT, respectively; (c) and (d) are the sagittal measurements for IMRT and VMAT, respectively.

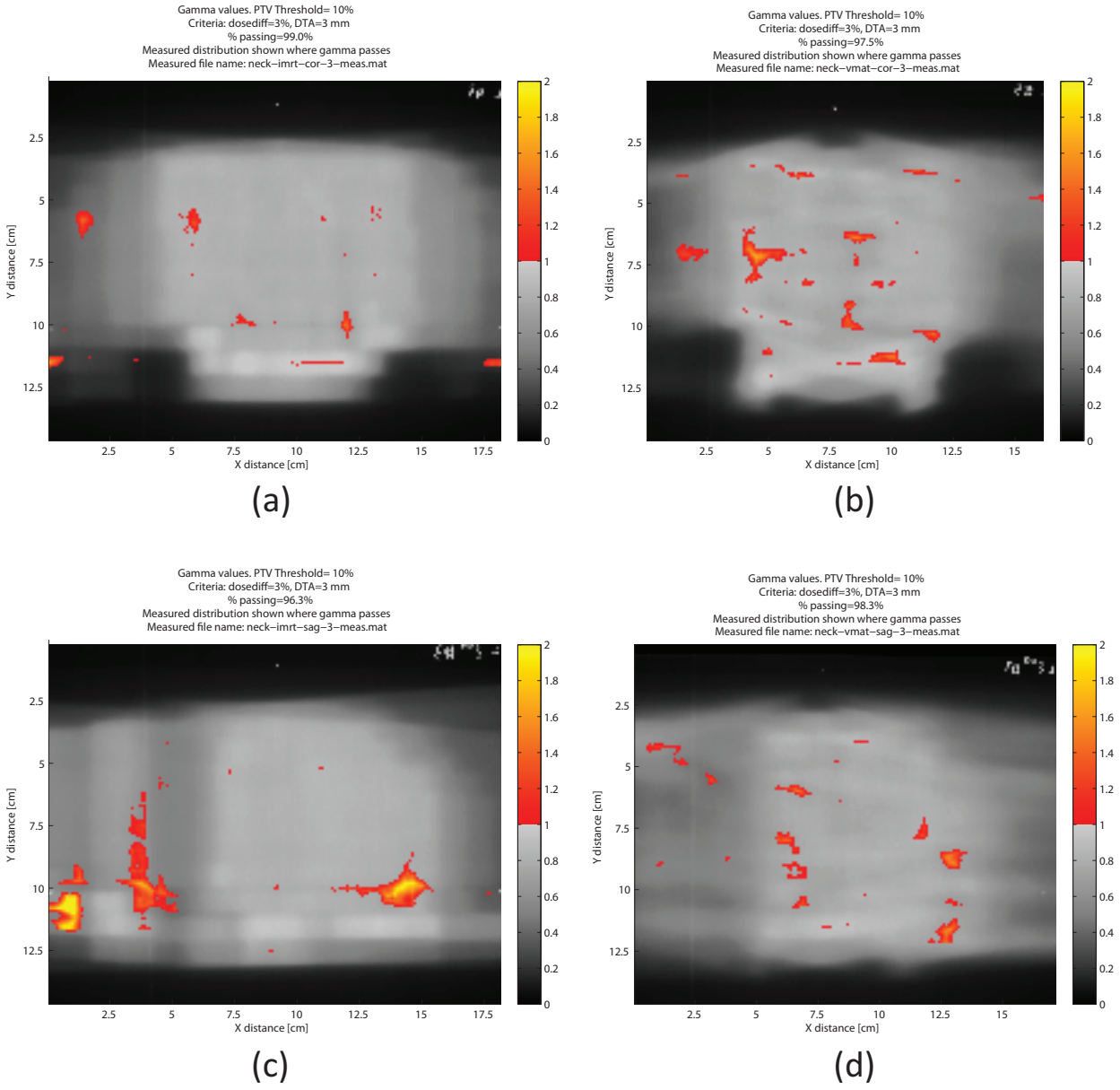

Figure A.7: Third set of gamma results for the head and neck film data. (a) and (b) are the coronal measurements for IMRT and VMAT, respectively; (c) and (d) are the sagittal measurements for IMRT and VMAT, respectively.

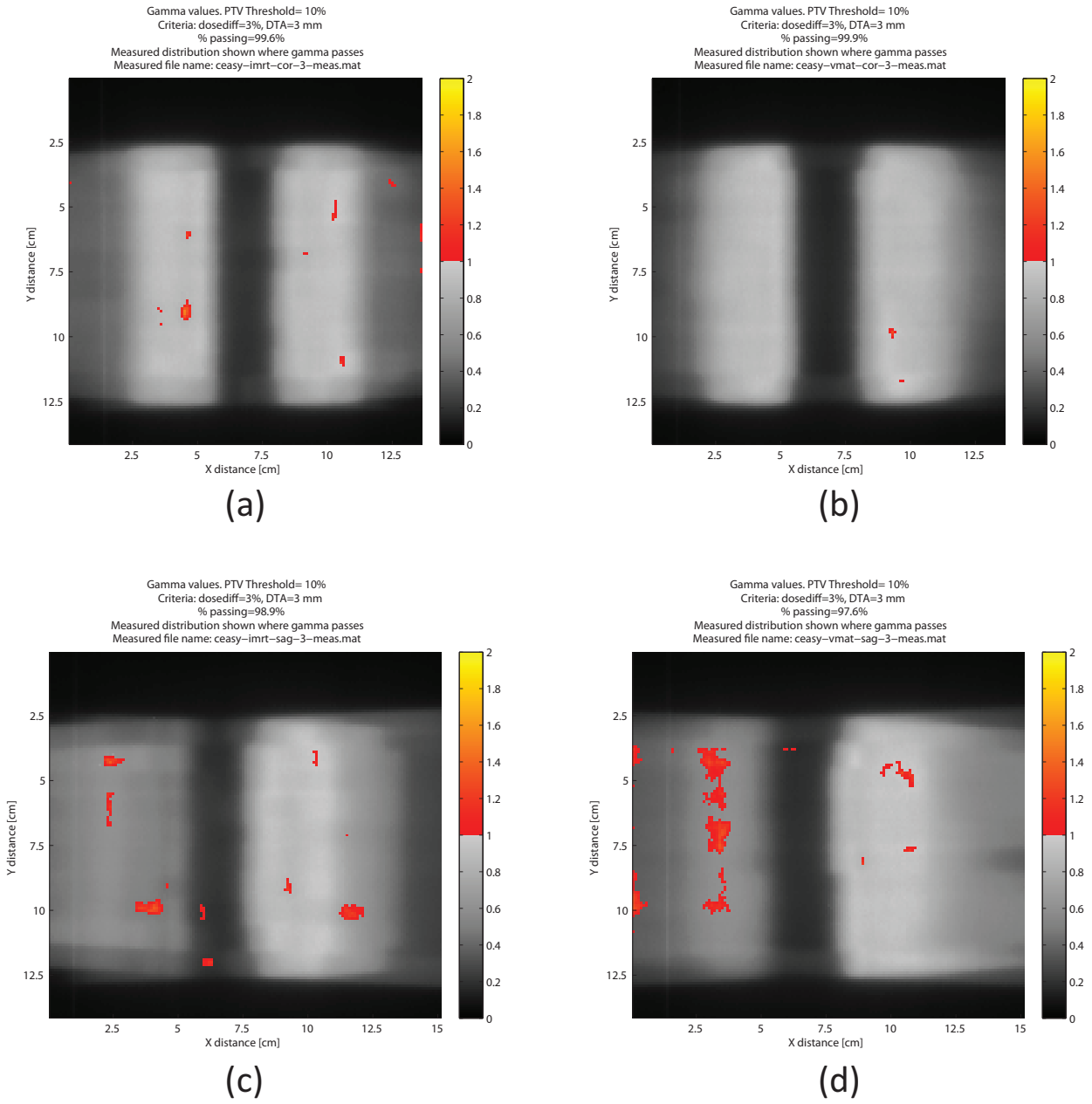

Figure A.8: Third set of gamma results for the C-shape film data. (a) and (b) are the coronal measurements for IMRT and VMAT, respectively; (c) and (d) are the sagittal measurements for IMRT and VMAT, respectively.

Appendix B

MapCHECK Images

This appendix includes the remaining MapCHECK images not shown in Sec. 3.4. The images shown there were the first MapCHECK output images for each unique combination of geometry and modality. The following images are the second through fifth such images.

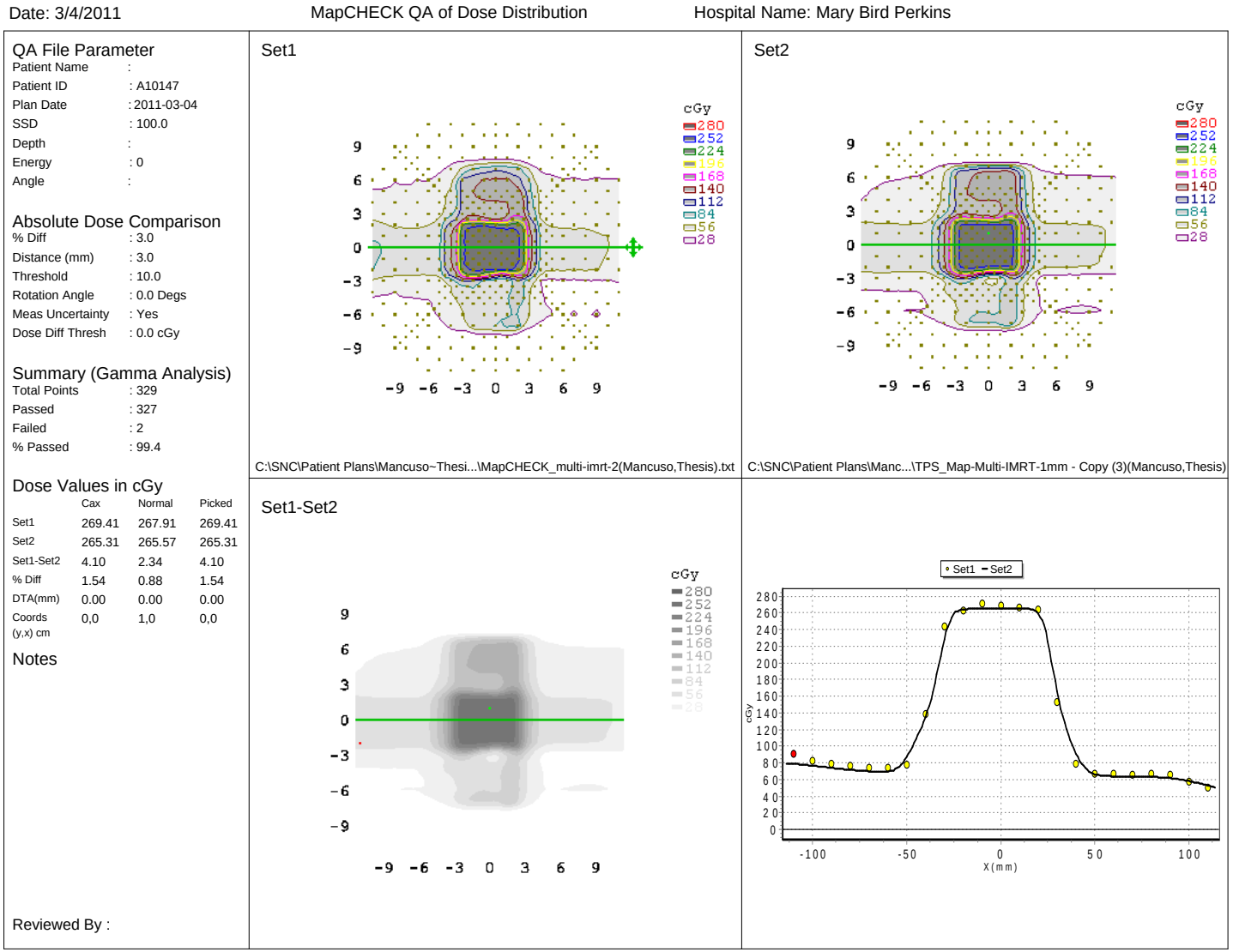

Figure B.1: Second MapCHECK result for the multitarget IMRT delivery.

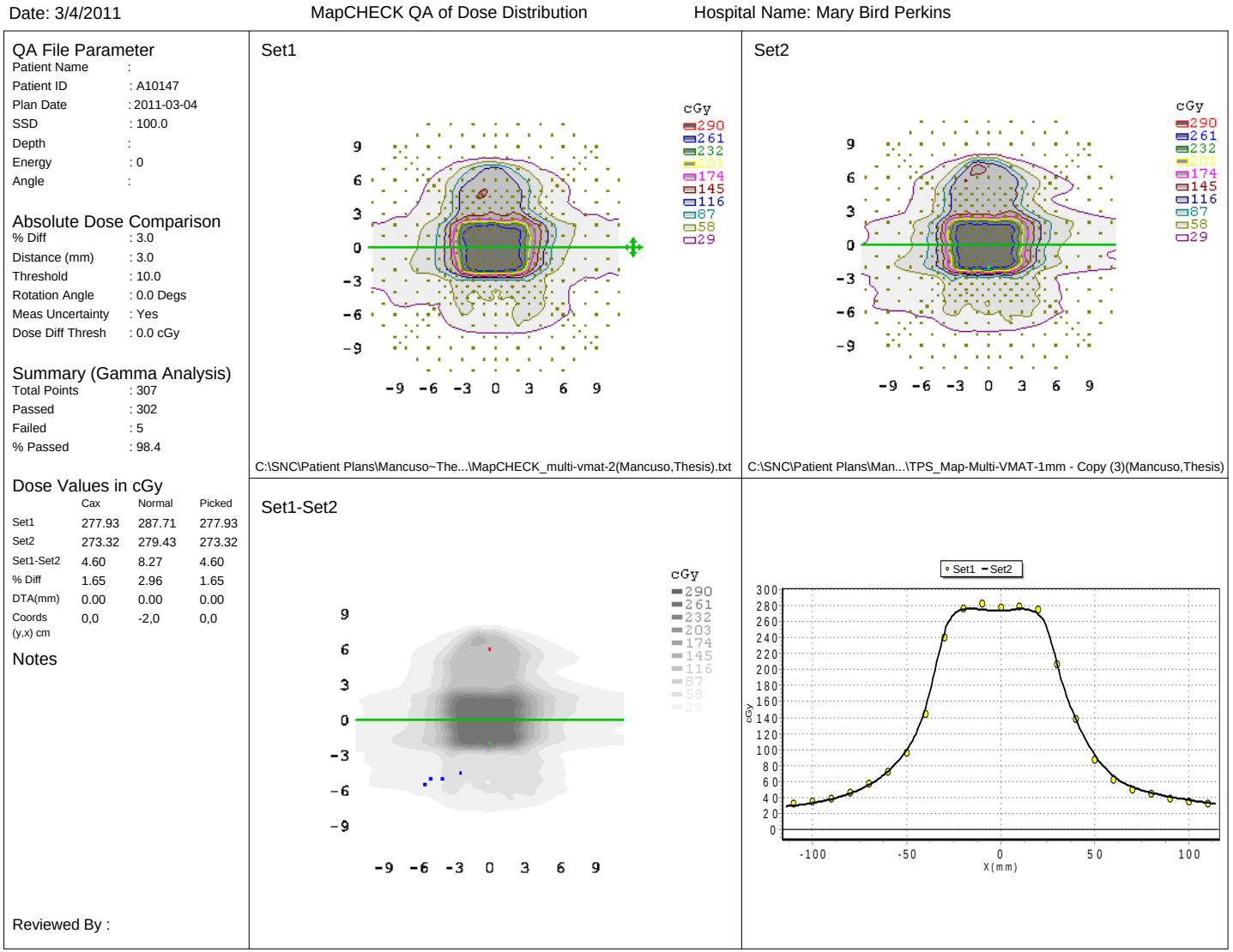

Figure B.2: Second MapCHECK result for the multitarget VMAT delivery.

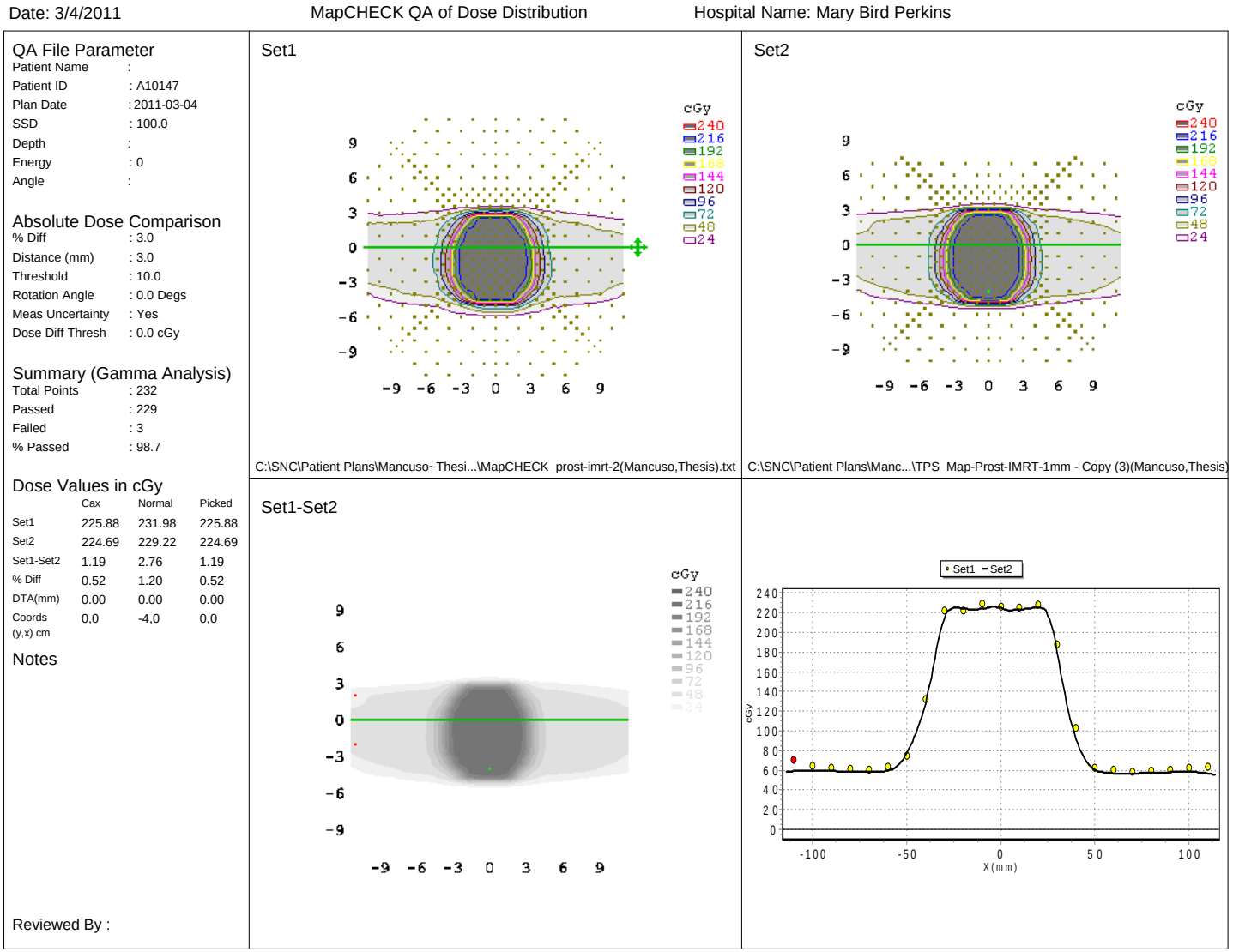

Figure B.3: Second MapCHECK result for the prostate IMRT delivery.

Date: 3/4/2011 MapCHECK QA of Dose Distribution Hospital Name: Mary Bird Perkins

QA File Parameter

Patient Name	:
Patient ID	: A10147
Plan Date	: 2011-03-04
SSD	: 100.0
Depth	:
Energy	: 0
Angle	:

Absolute Dose Comparison

% Diff	: 3.0
Distance (mm)	: 3.0
Threshold	: 10.0
Rotation Angle	: 0.0 Degs
Meas Uncertainty	: Yes
Dose Diff Thresh	: 0.0 cGy

Summary (Gamma Analysis)

Total Points	: 241
Passed	: 240
Failed	: 1
% Passed	: 99.6

Dose Values in cGy

	Cax	Normal	Picked
Set1	221.62	220.60	221.62
Set2	218.03	213.47	218.03
Set1-Set2	3.59	7.13	3.59
% Diff	1.68	3.34	1.68
DTA(mm)	0.00	0.00	0.00
Coords (y,x) cm	0,0	-4.5,0.5	0,0

Notes

Reviewed By :

Set1

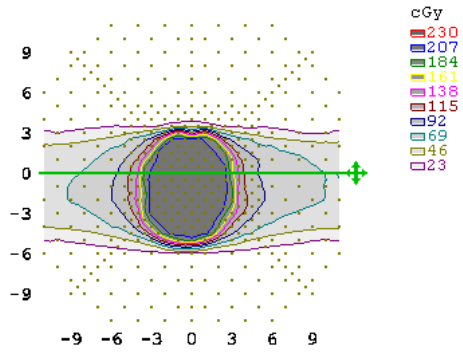

C:\SNC\Patient Plans\Mancuso~The...\MapCHECK_prost-vmat-2(Mancuso,Thesis).txt

Set2

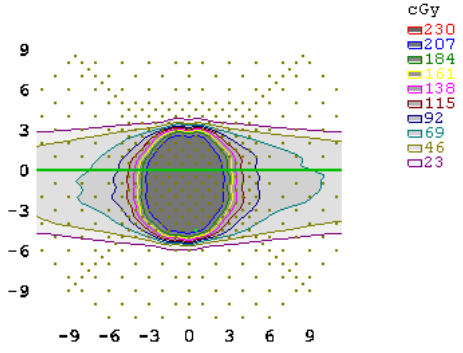

C:\SNC\Patient Plans\Man...\TPS_Map-Prost-VMAT-1mm - Copy (3)(Mancuso,Thesis)

Set1-Set2

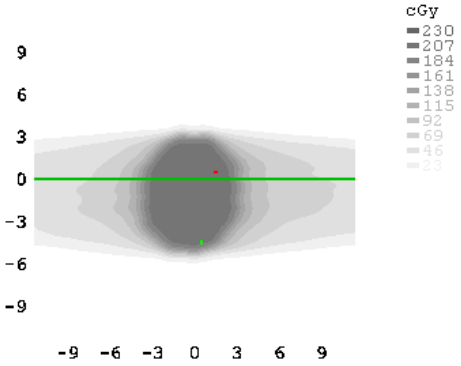

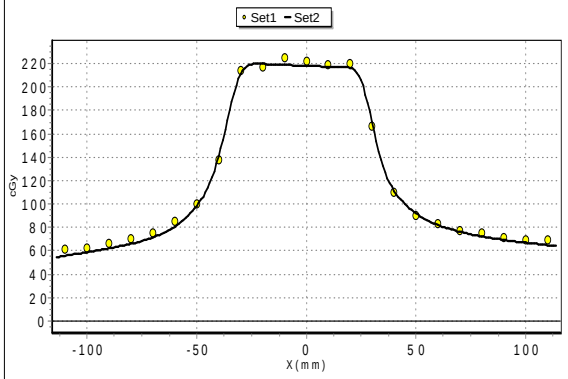

Figure B.4: Second MapCHECK result for the prostate VMAT delivery.

Date: 3/4/2011 MapCHECK QA of Dose Distribution Hospital Name: Mary Bird Perkins

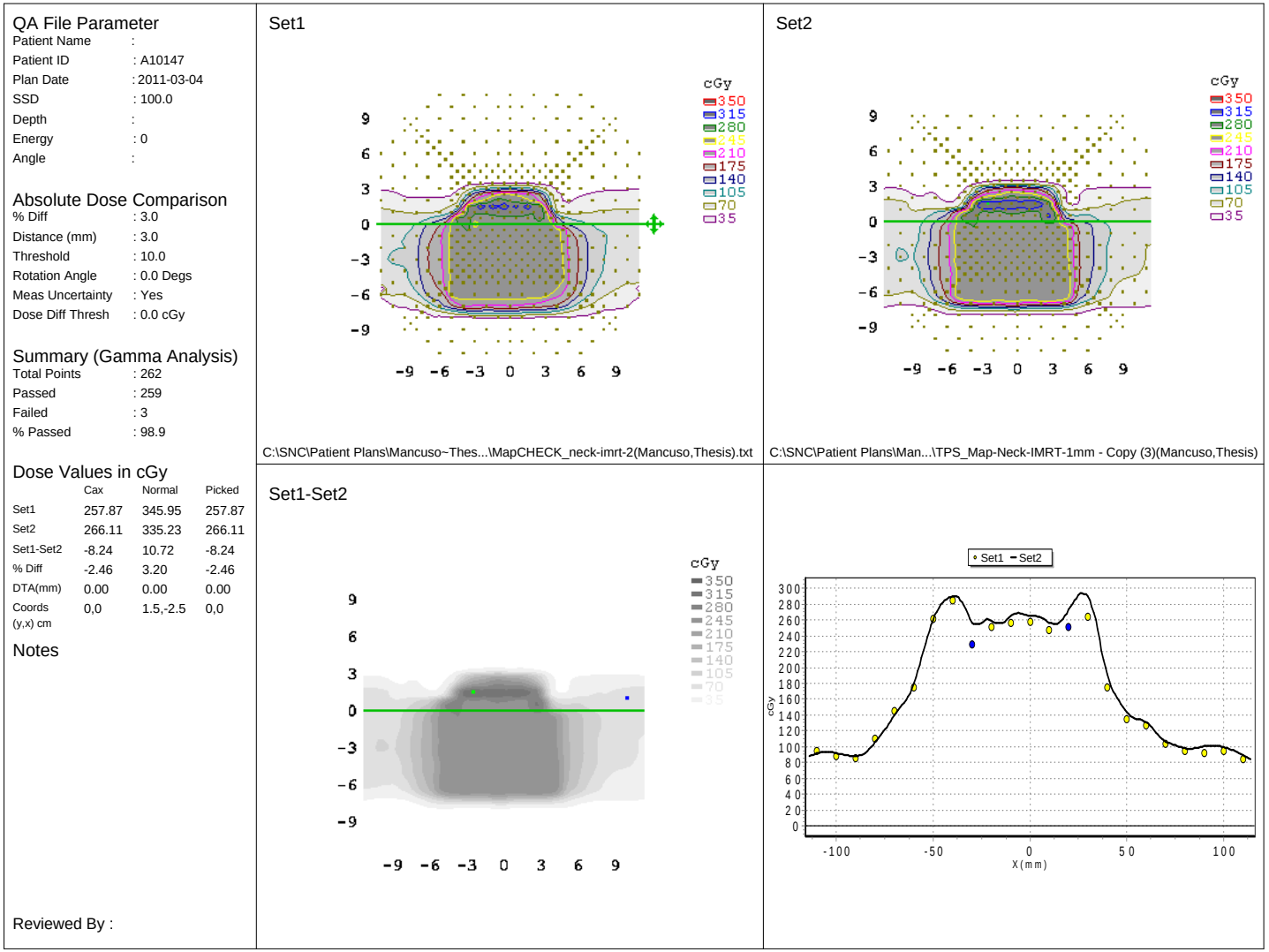

Figure B.5: Second MapCHECK result for the head and neck IMRT delivery.

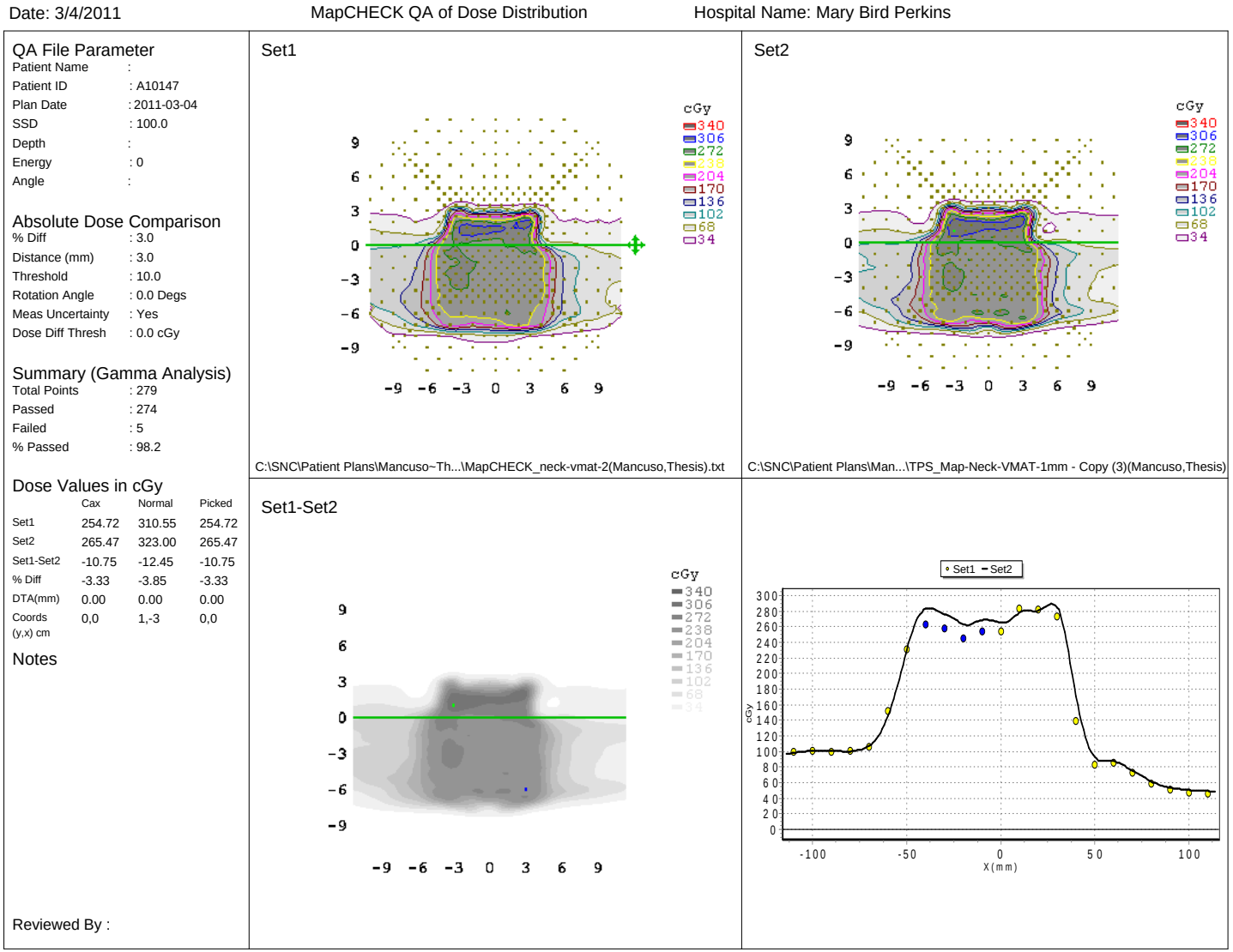

Figure B.6: Second MapCHECK result for the head and neck VMAT delivery.

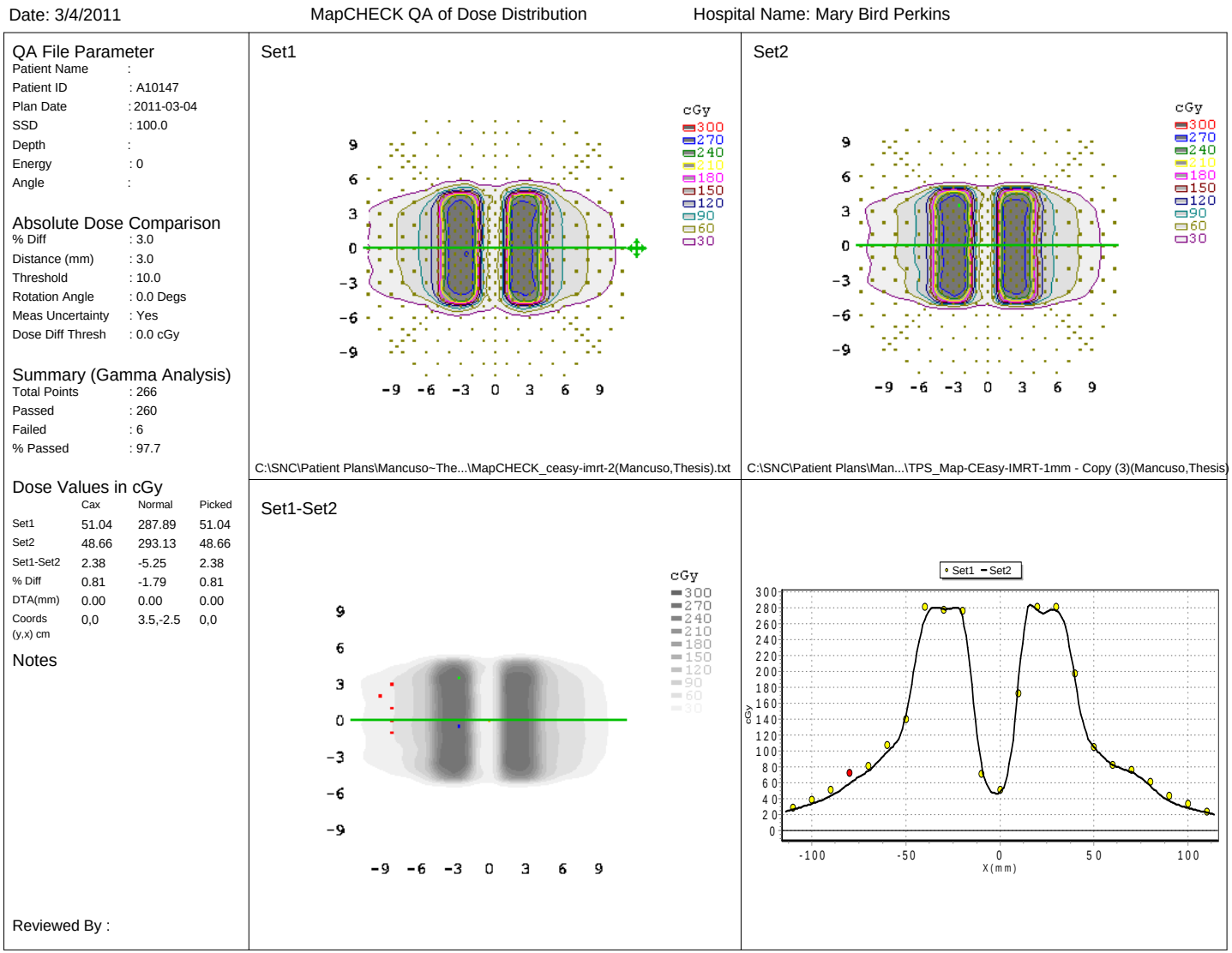

Figure B.7: Second MapCHECK result for the C-shape IMRT delivery.

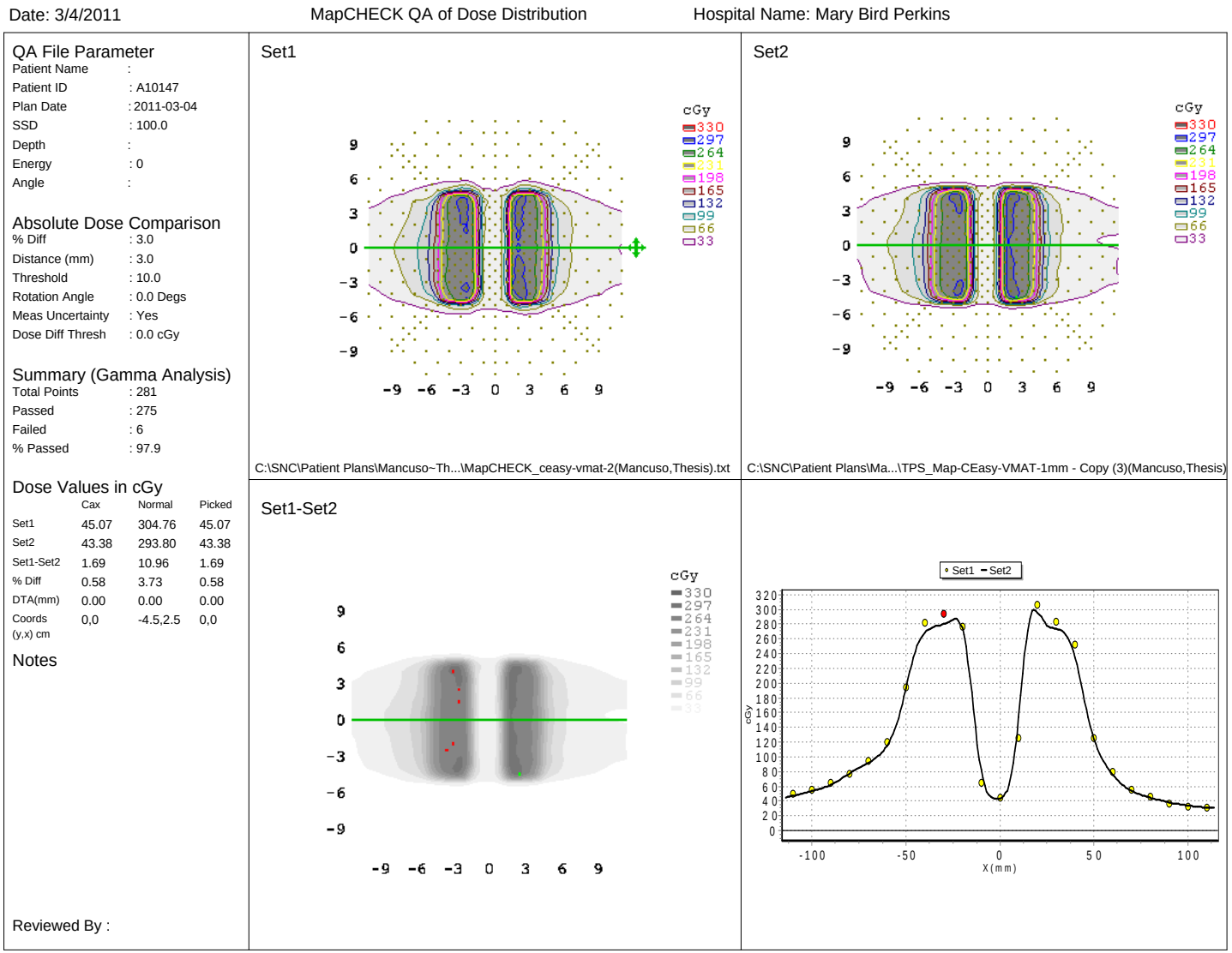

Figure B.8: Second MapCHECK result for the C-shape VMAT delivery.

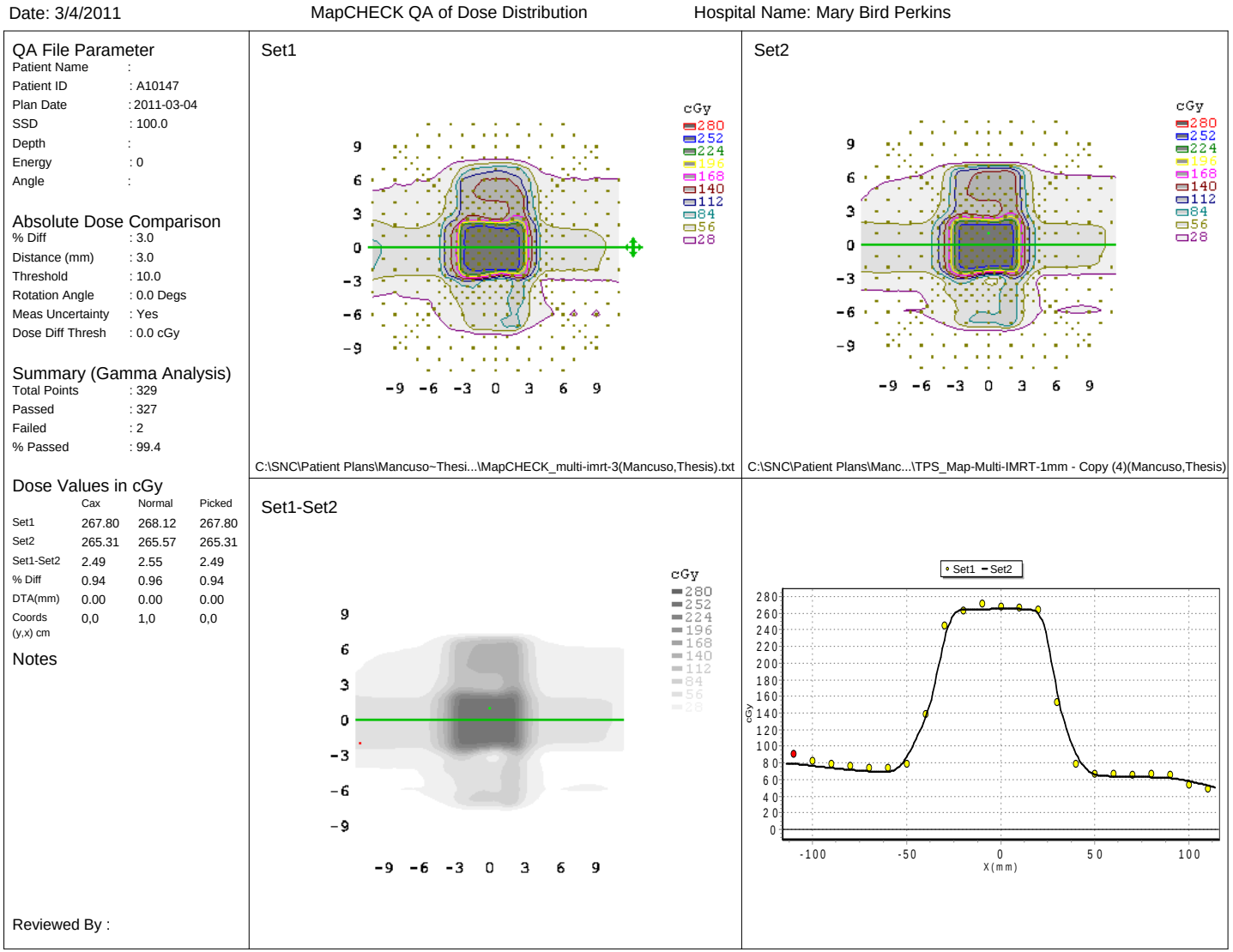

Figure B.9: Third MapCHECK result for the multitarget IMRT delivery.

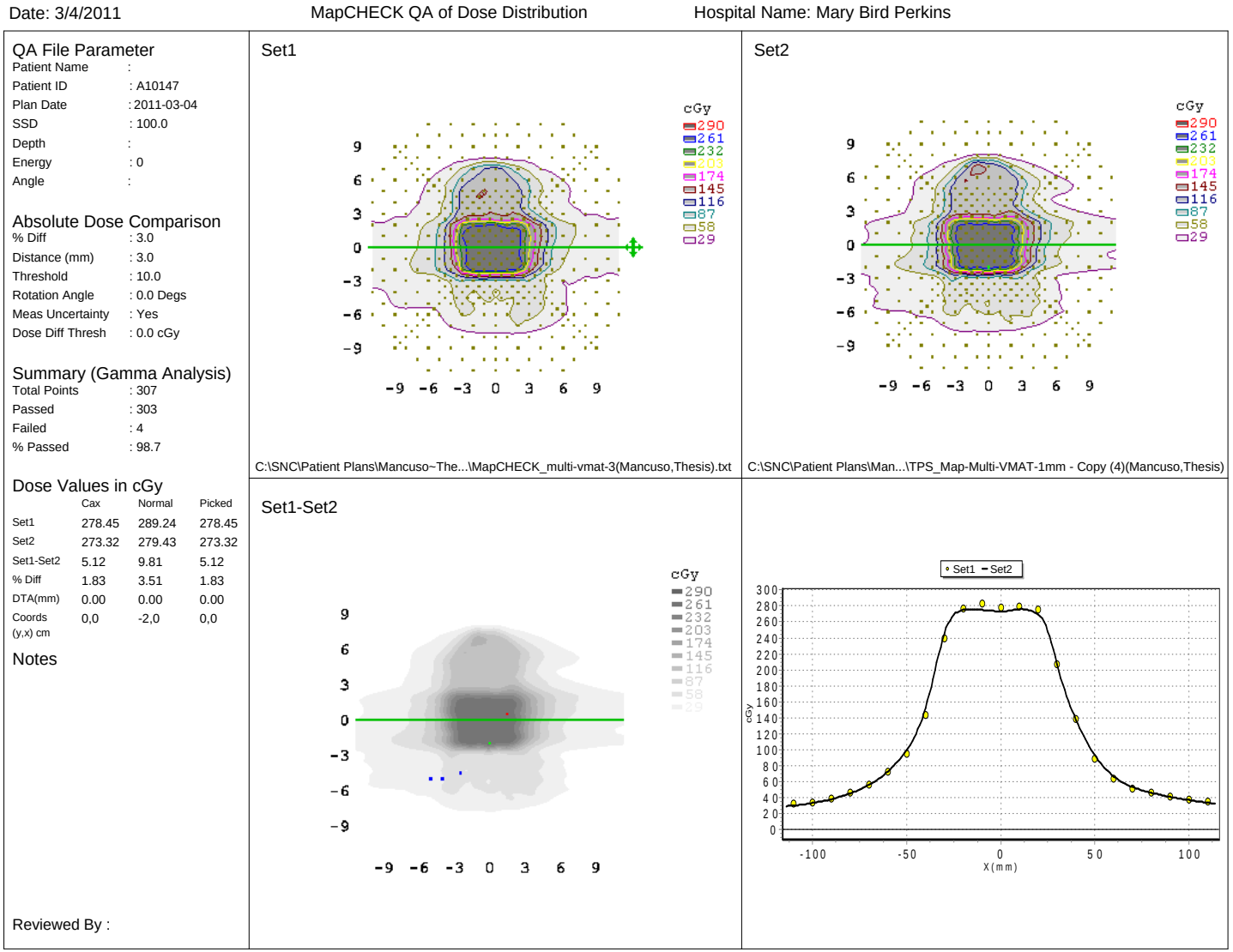

Figure B.10: Third MapCHECK result for the multitarget VMAT delivery.

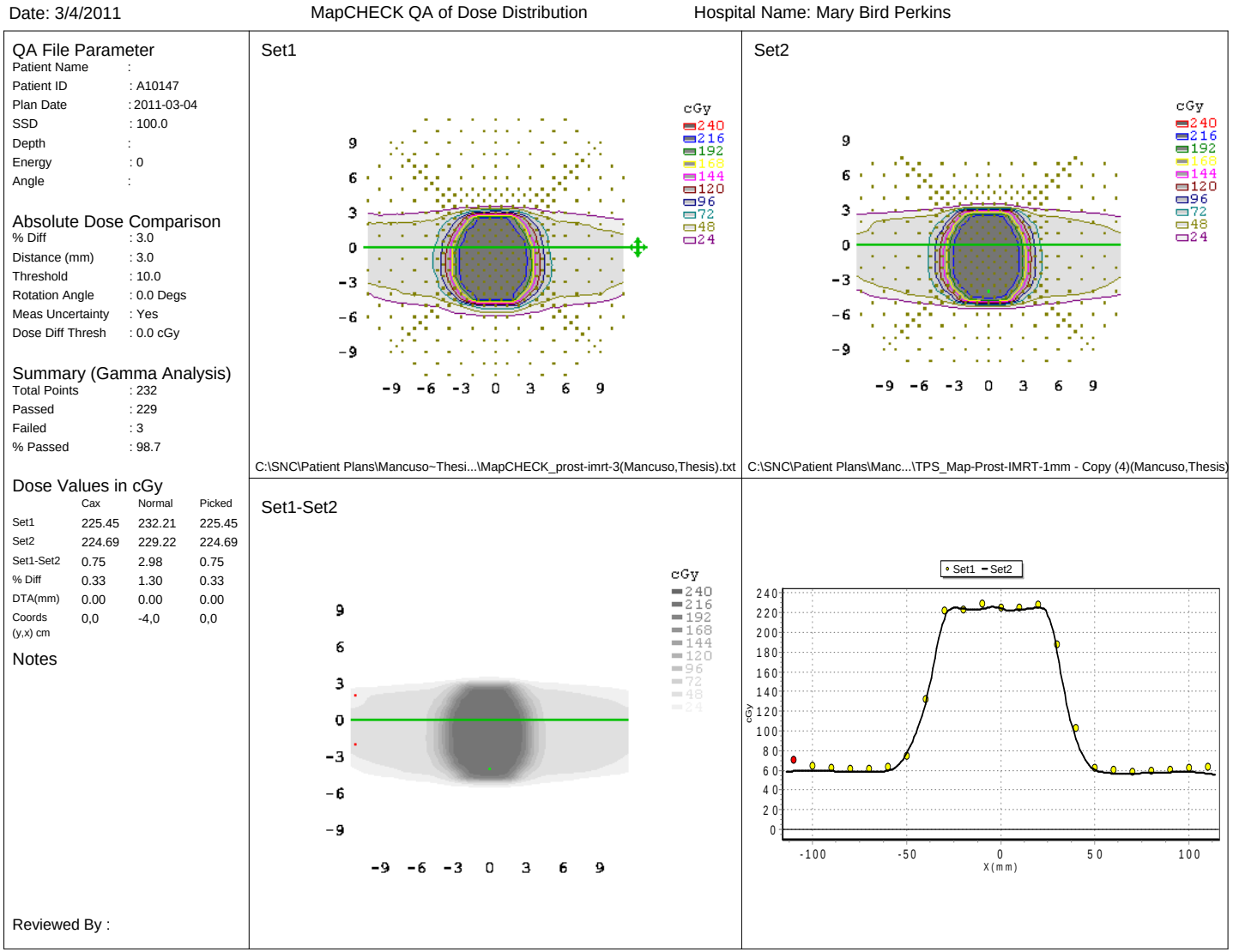

Figure B.11: Third MapCHECK result for the prostate IMRT delivery.

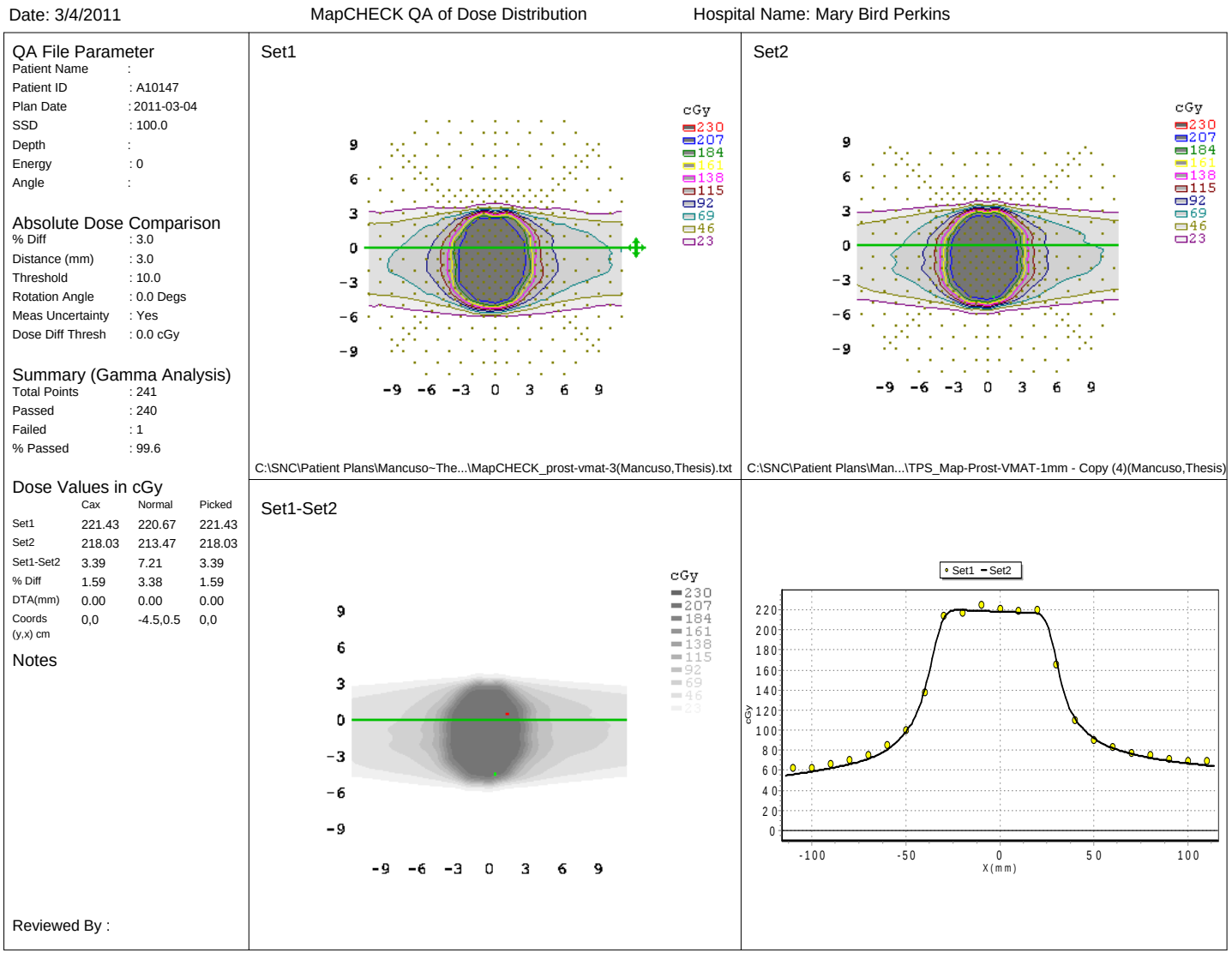

Figure B.12: Third MapCHECK result for the prostate VMAT delivery.

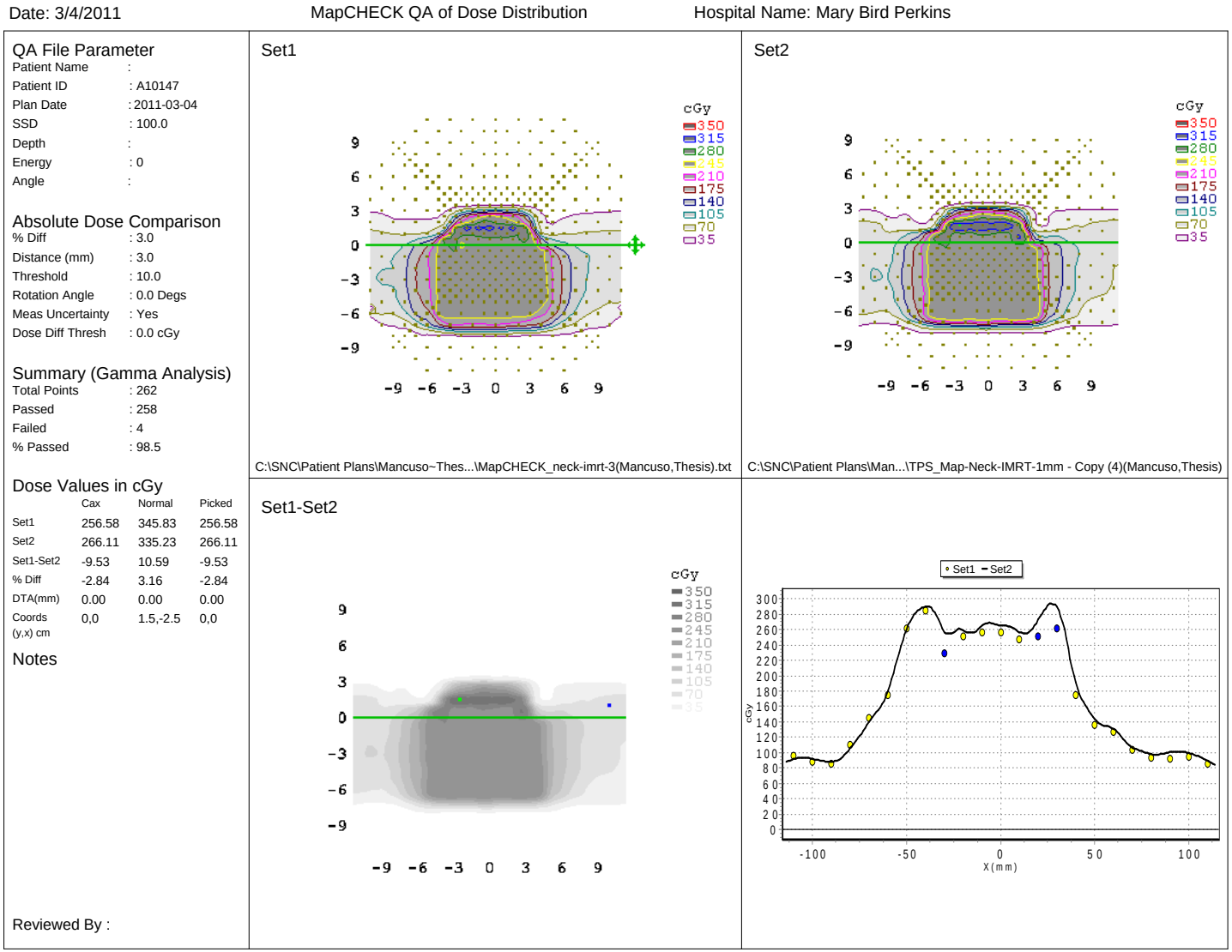

Figure B.13: Third MapCHECK result for the head and neck IMRT delivery.

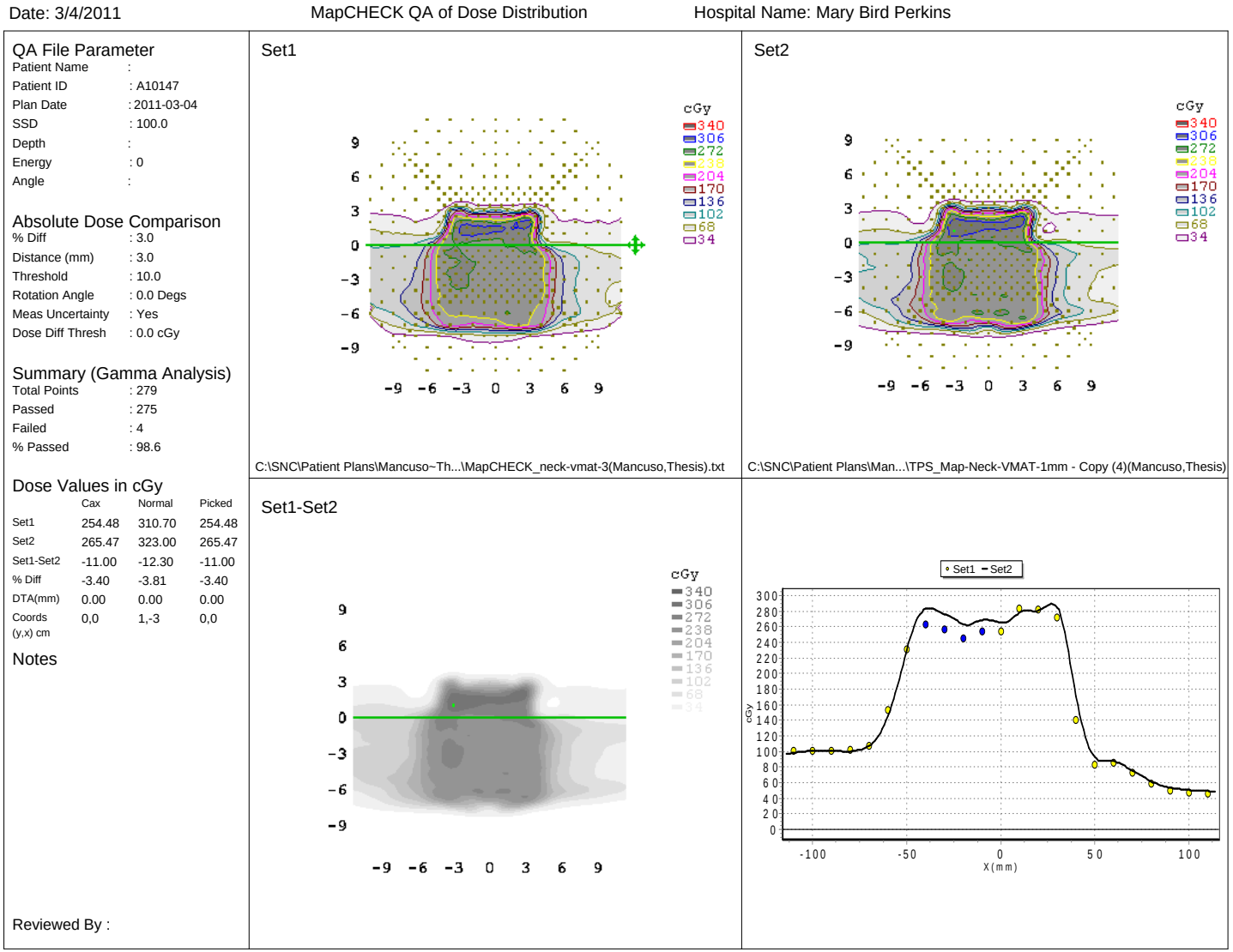

Figure B.14: Third MapCHECK result for the head and neck VMAT delivery.

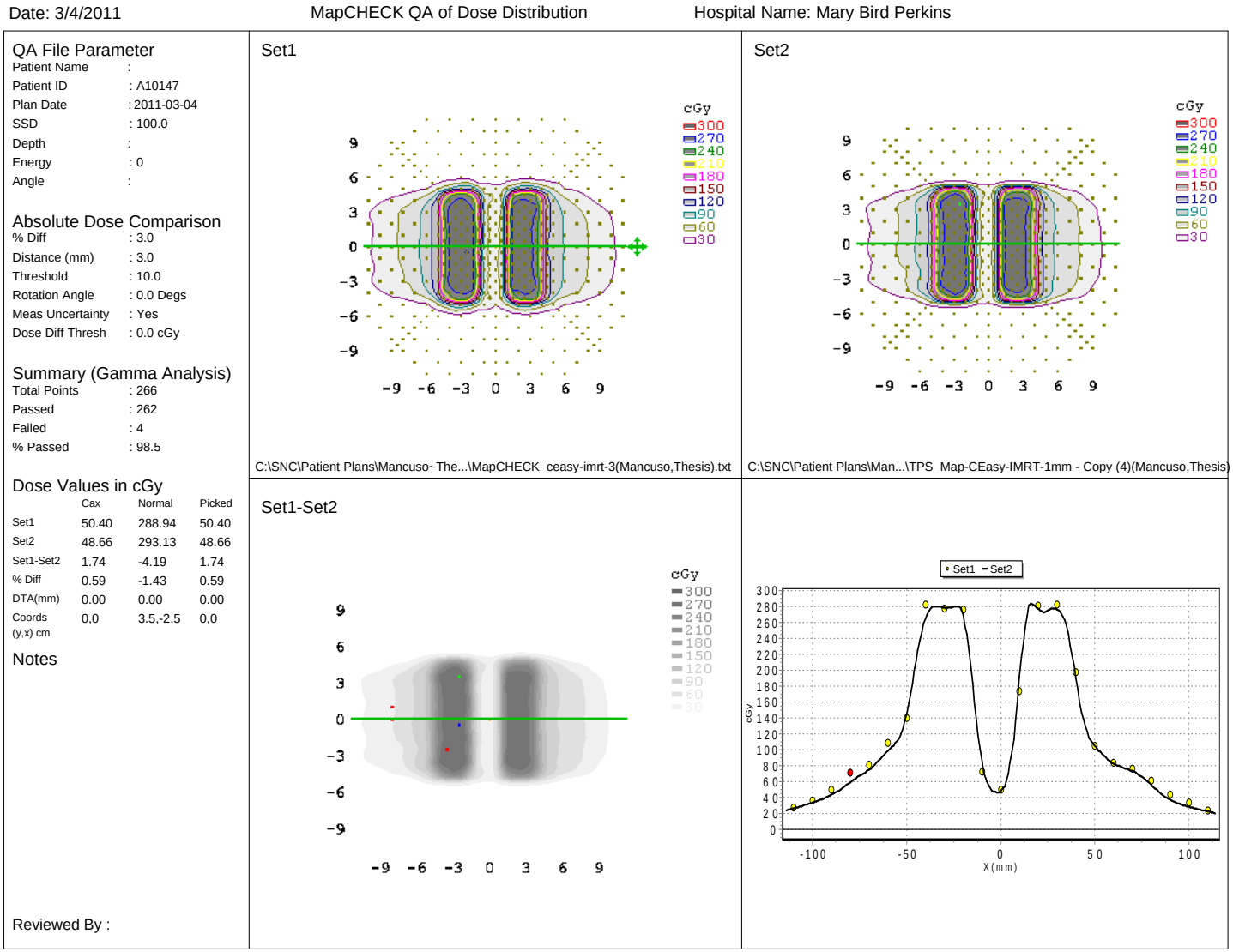

Figure B.15: Third MapCHECK result for the C-shape IMRT delivery.

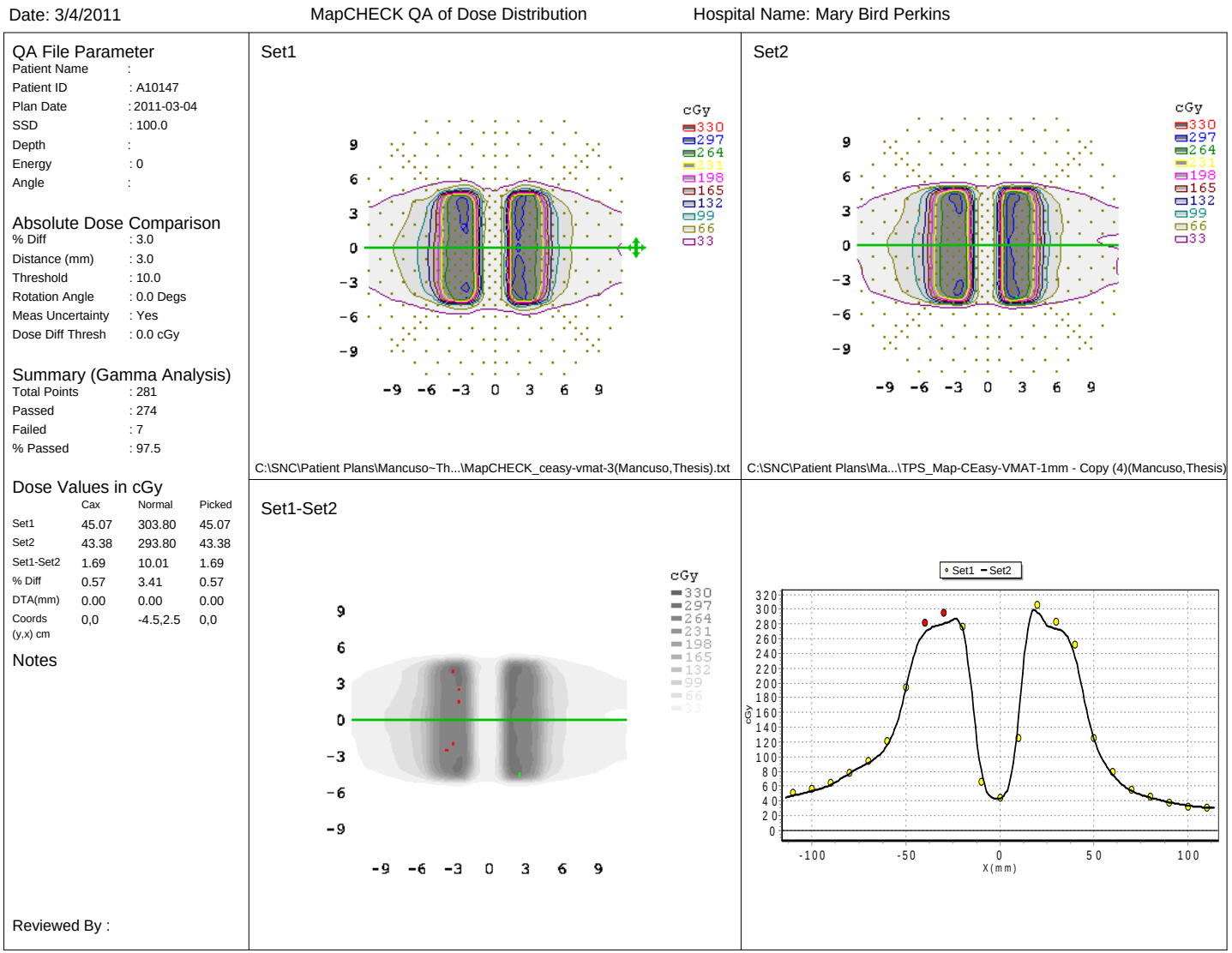

Figure B.16: Third MapCHECK result for the C-shape VMAT delivery.

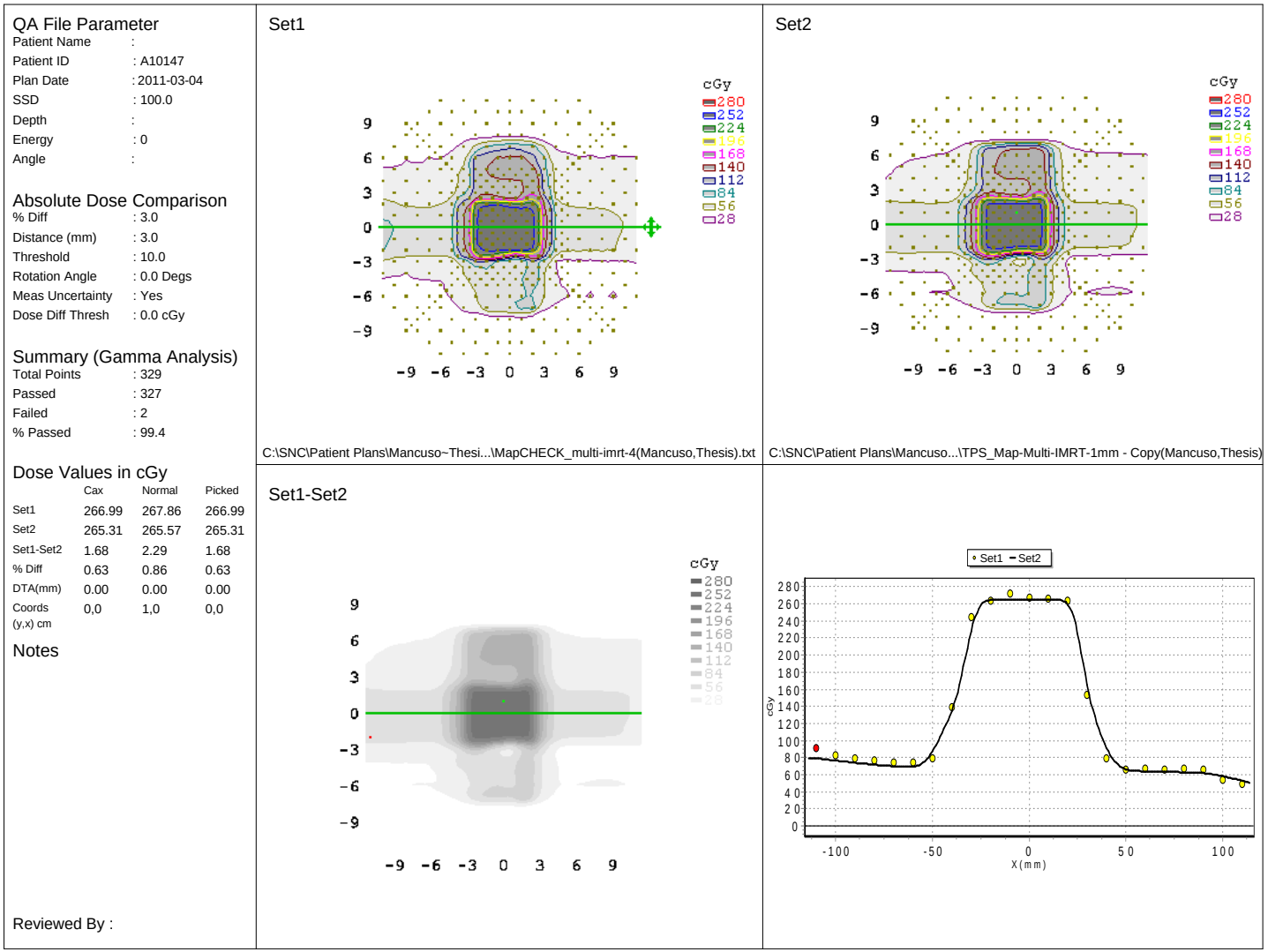

Figure B.17: Fourth MapCHECK result for the multitarget IMRT delivery.

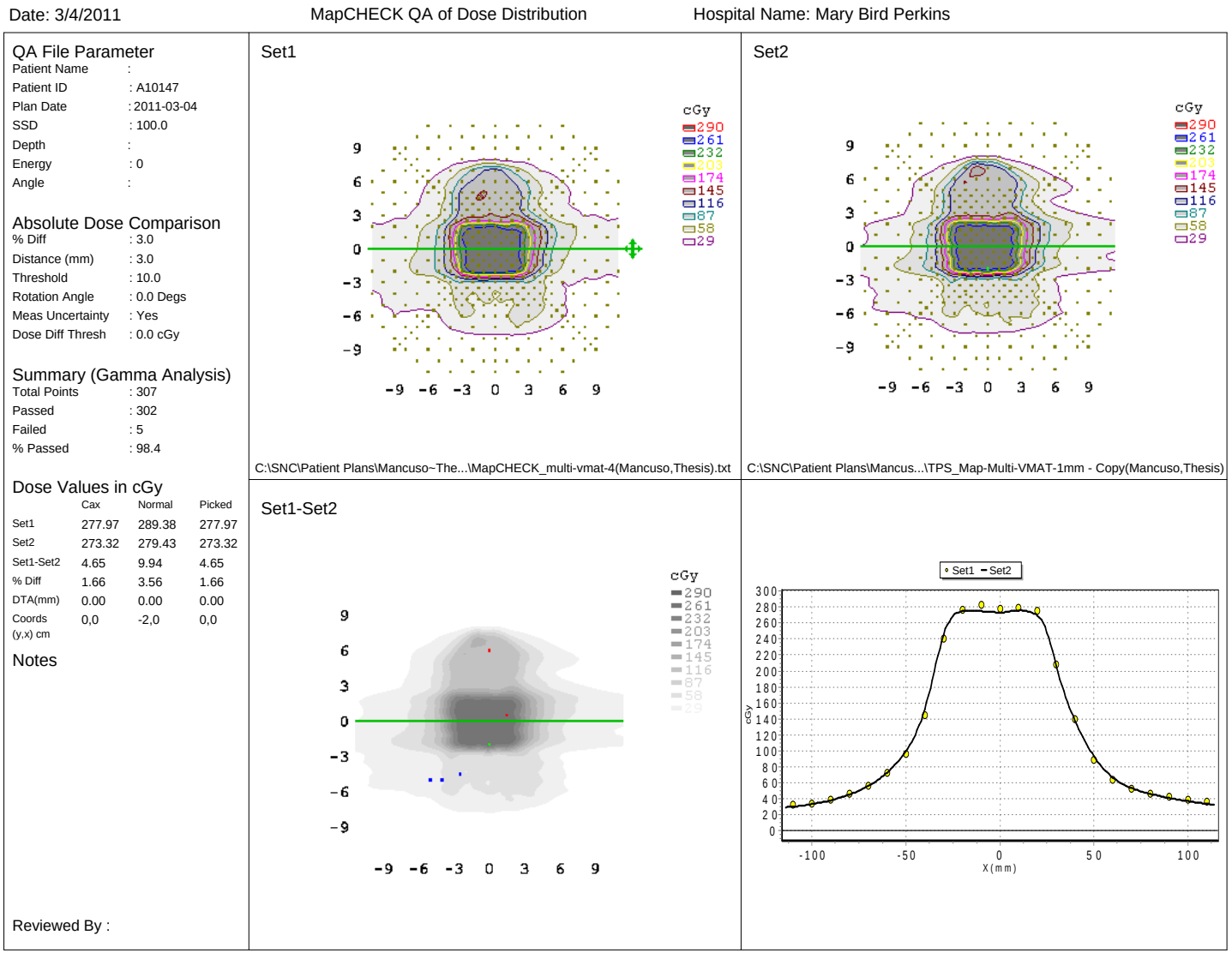

Figure B.18: Fourth MapCHECK result for the multitarget VMAT delivery.

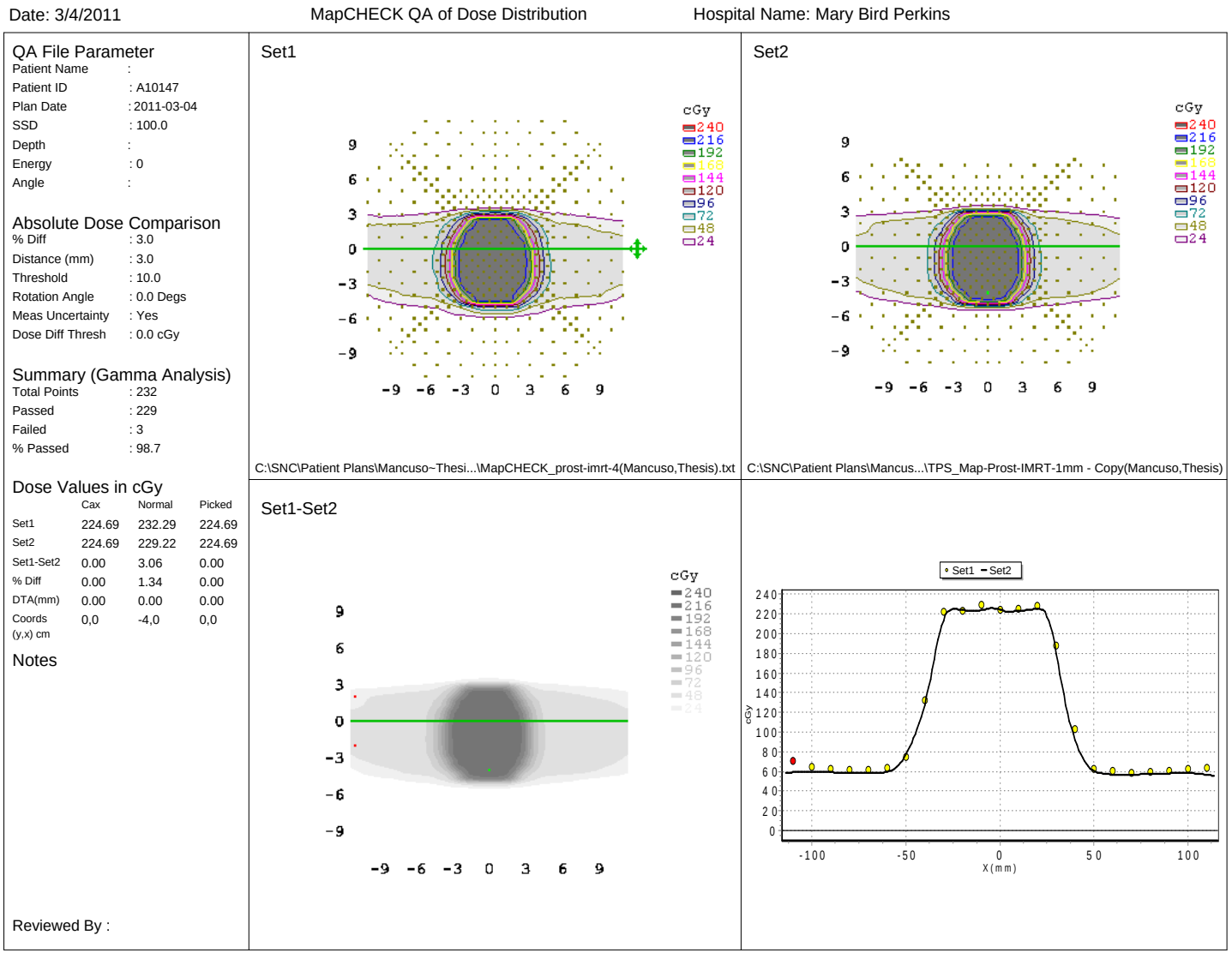

Figure B.19: Fourth MapCHECK result for the prostate IMRT delivery.

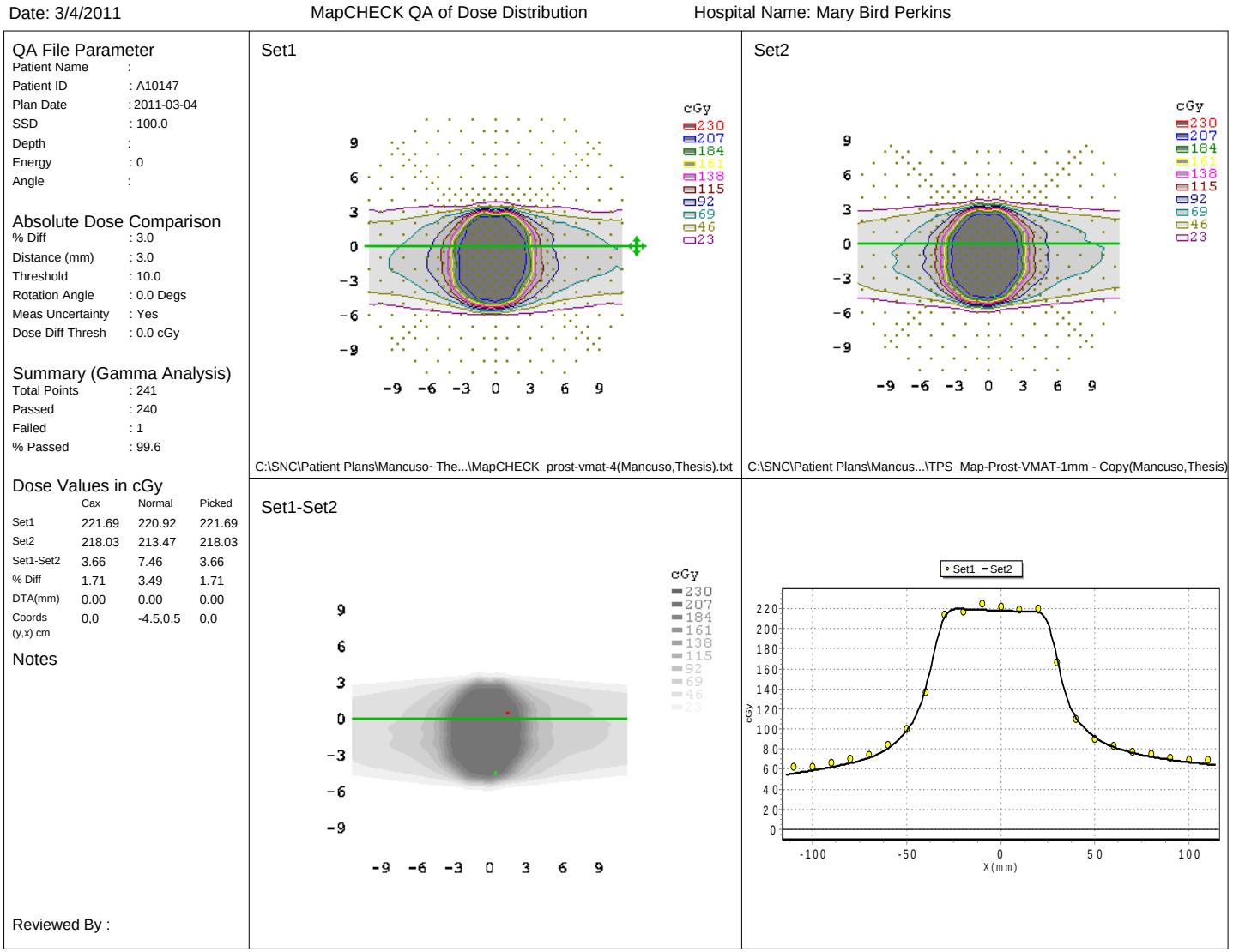

Figure B.20: Fourth MapCHECK result for the prostate VMAT delivery.

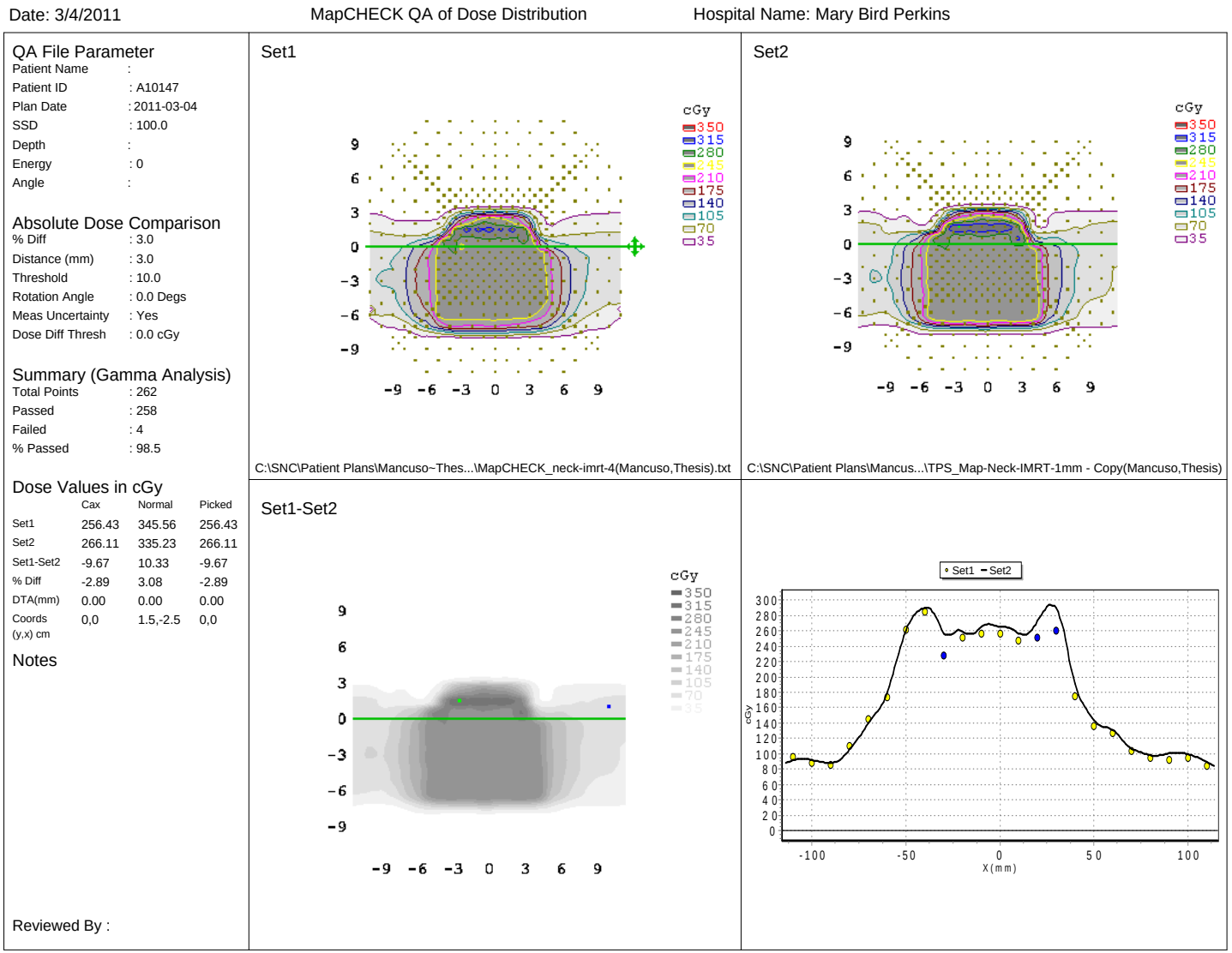

Figure B.21: Fourth MapCHECK result for the head and neck IMRT delivery.

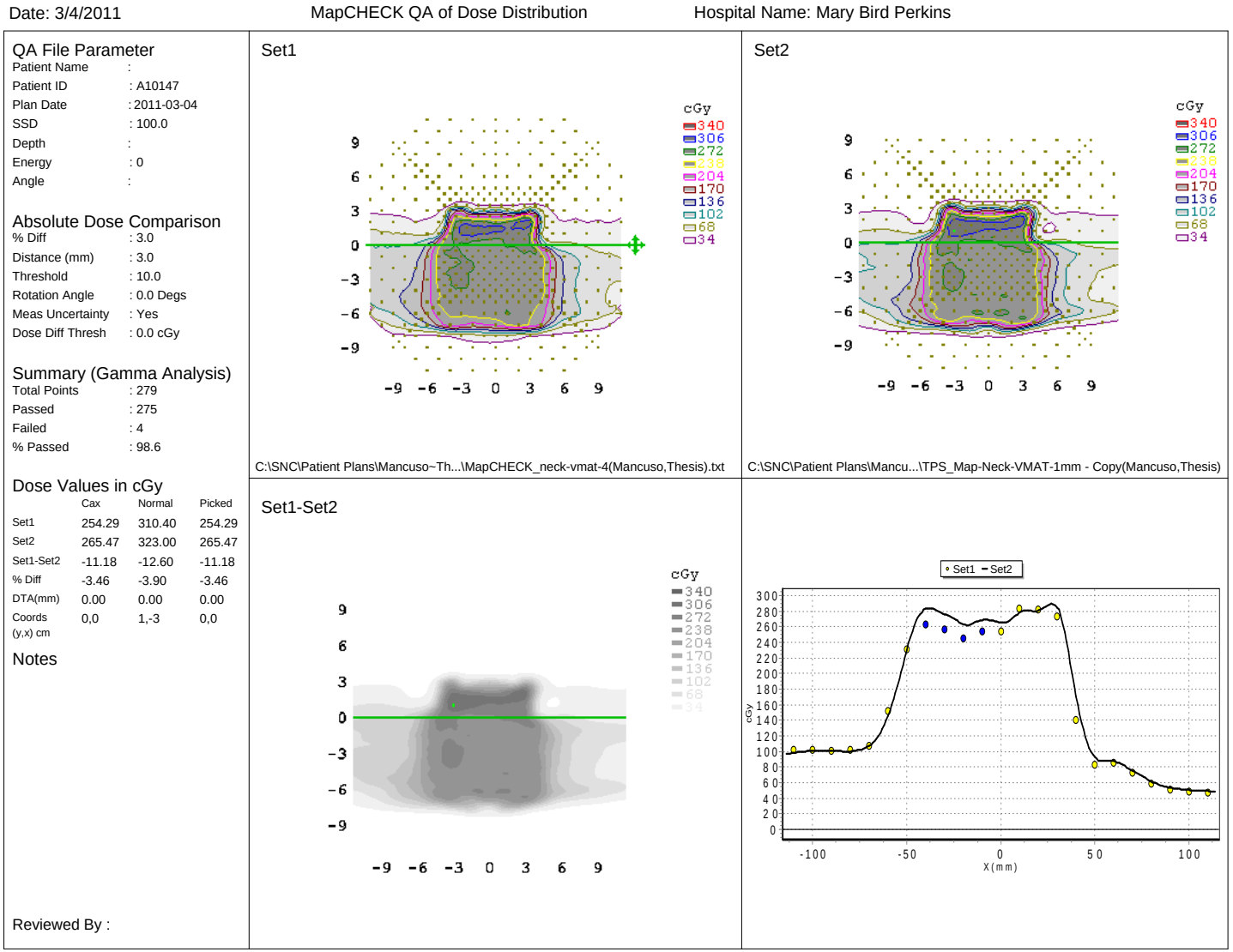

Figure B.22: Fourth MapCHECK result for the head and neck VMAT delivery.

Date: 3/4/2011 MapCHECK QA of Dose Distribution Hospital Name: Mary Bird Perkins

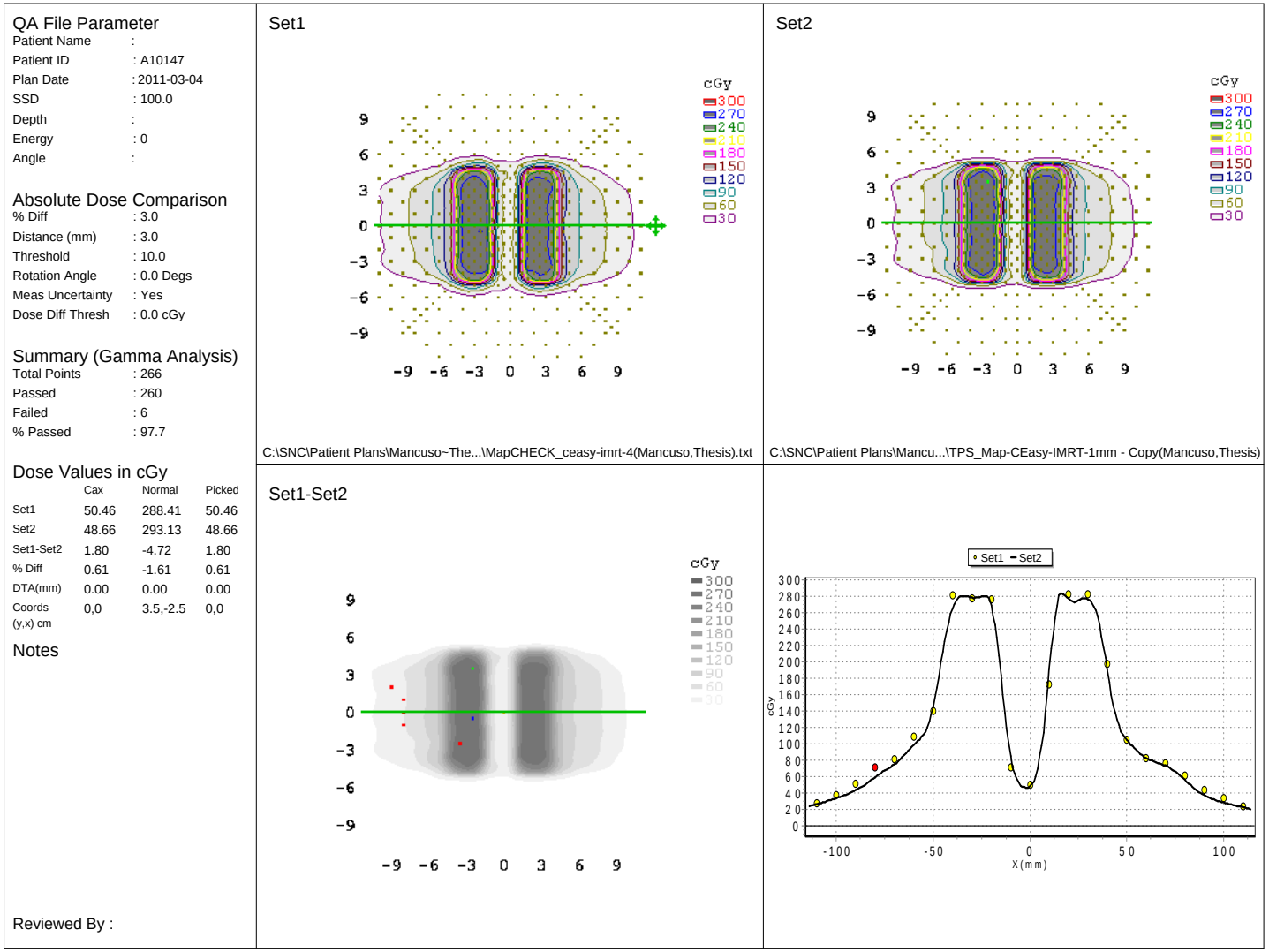

Figure B.23: Fourth MapCHECK result for the C-shape IMRT delivery.

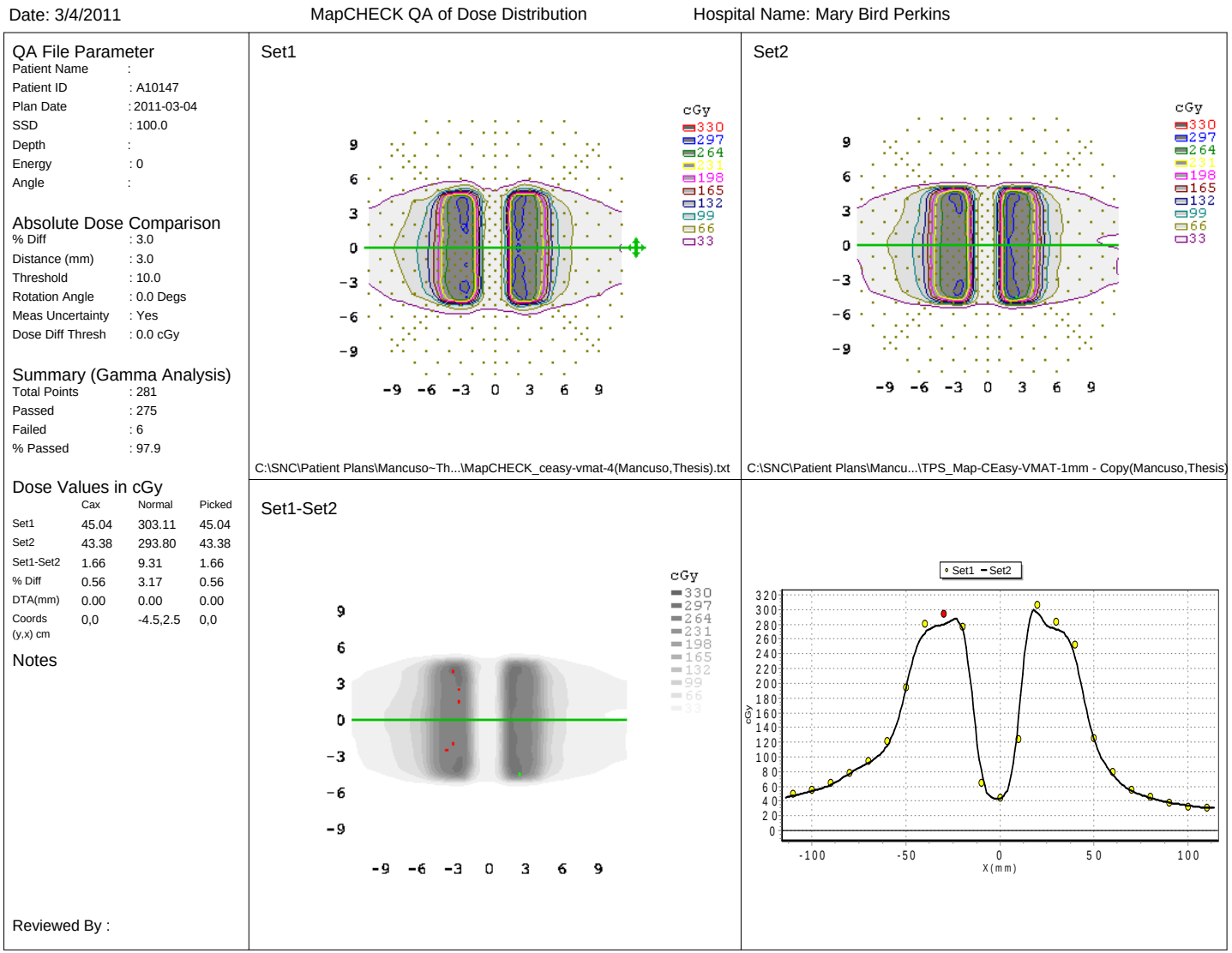

Figure B.24: Fourth MapCHECK result for the C-shape VMAT delivery.

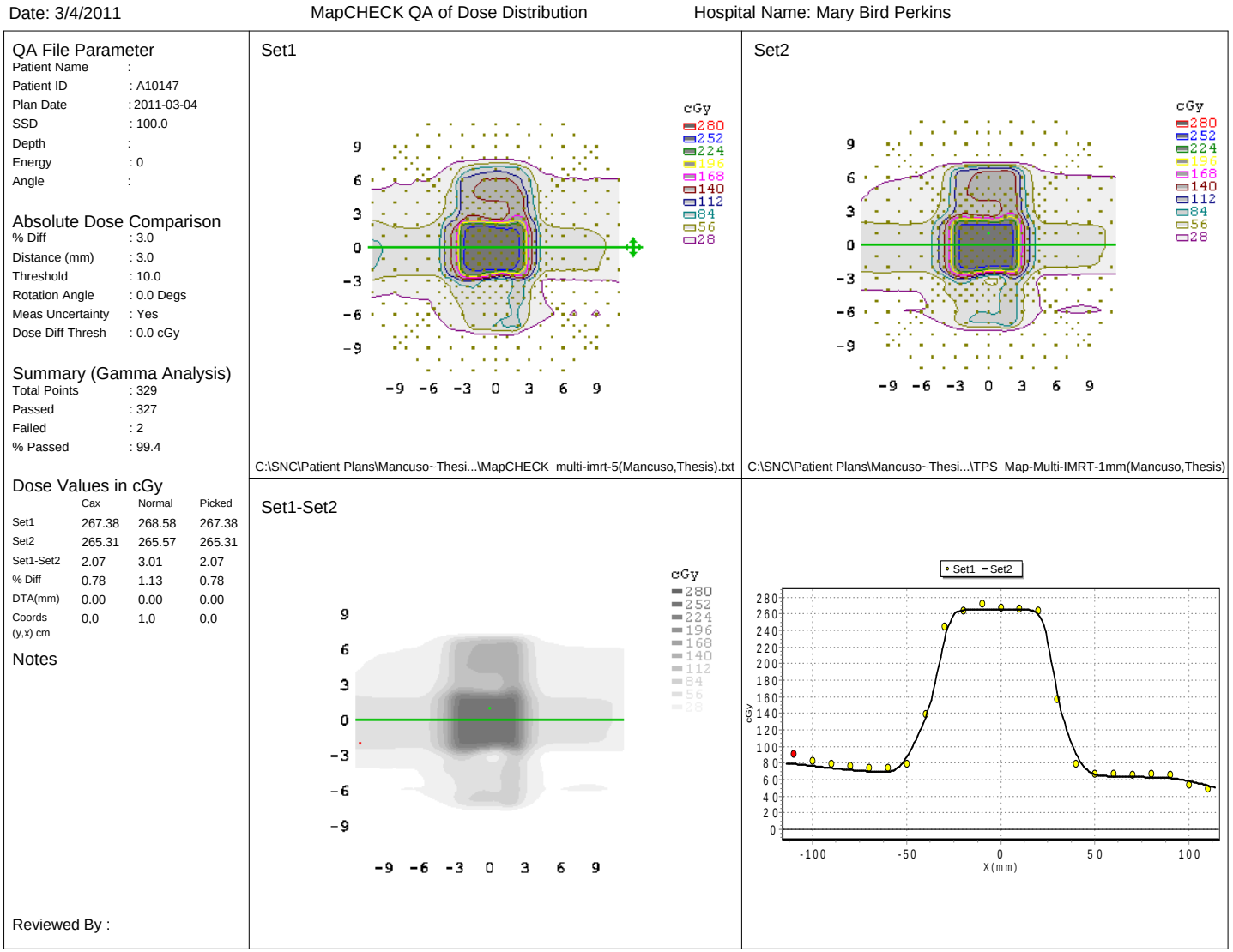

Figure B.25: Fifth MapCHECK result for the multitarget IMRT delivery.

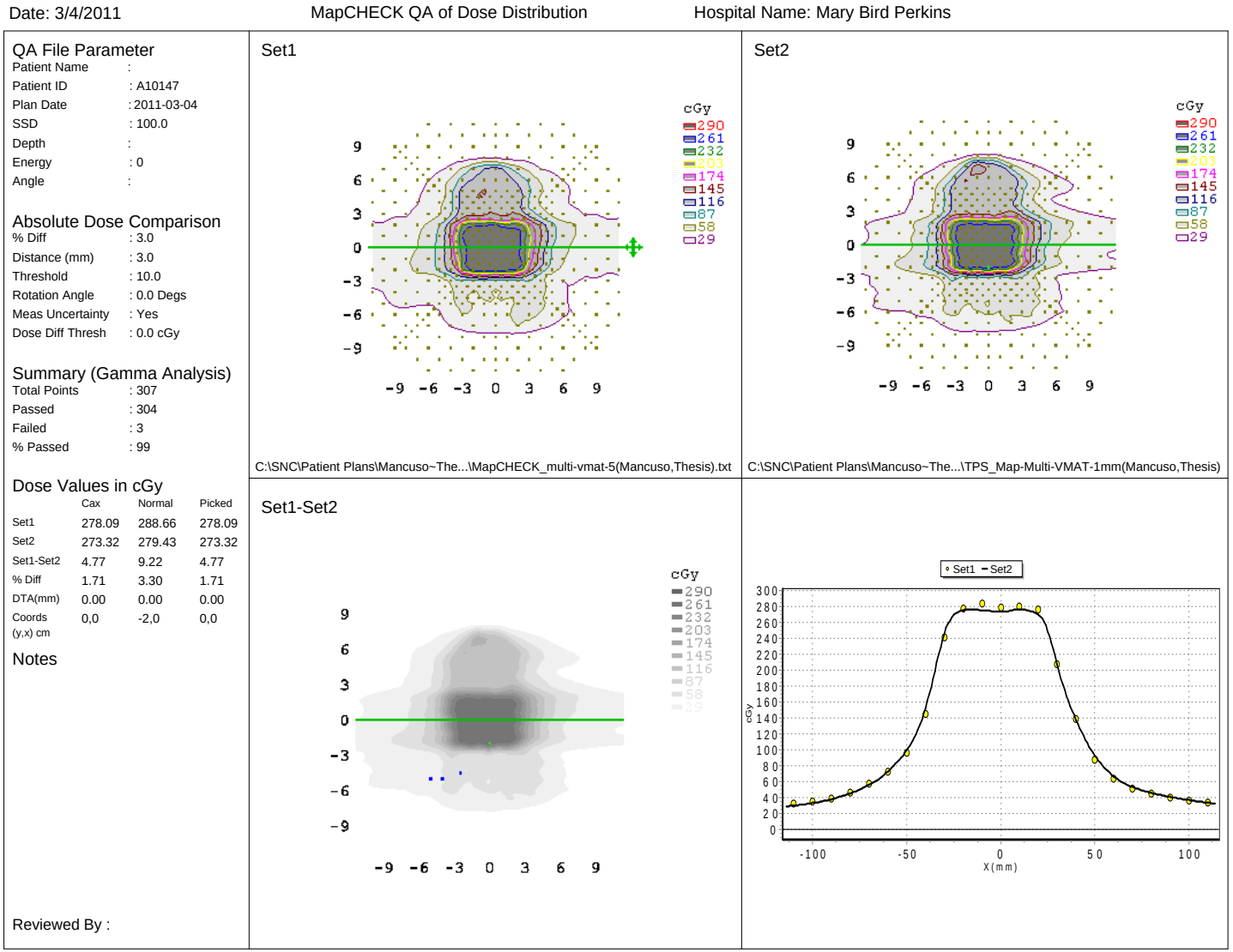

Figure B.26: Fifth MapCHECK result for the multitarget VMAT delivery.

Date: 3/4/2011 MapCHECK QA of Dose Distribution Hospital Name: Mary Bird Perkins

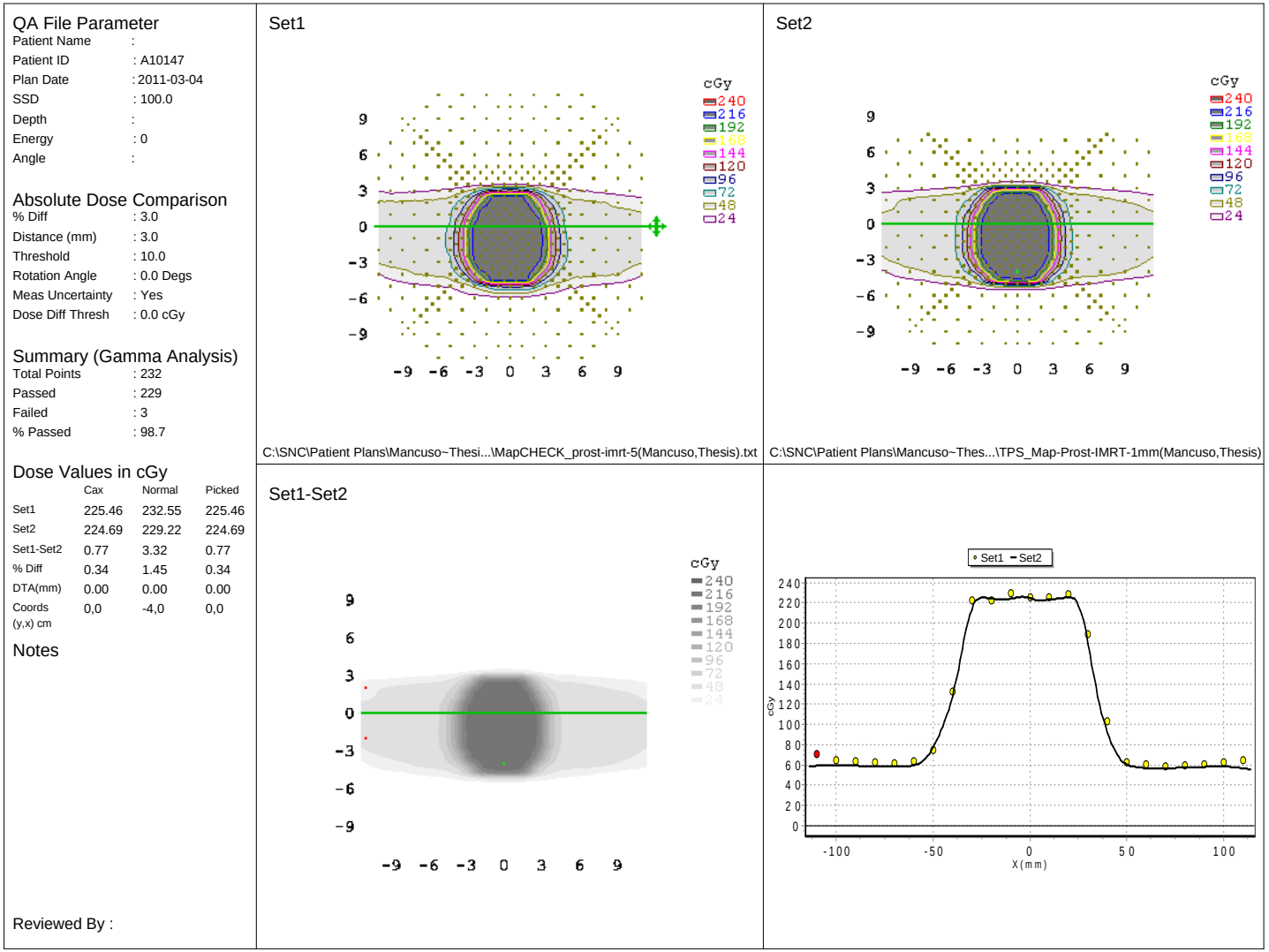

Figure B.27: Fifth MapCHECK result for the prostate IMRT delivery.

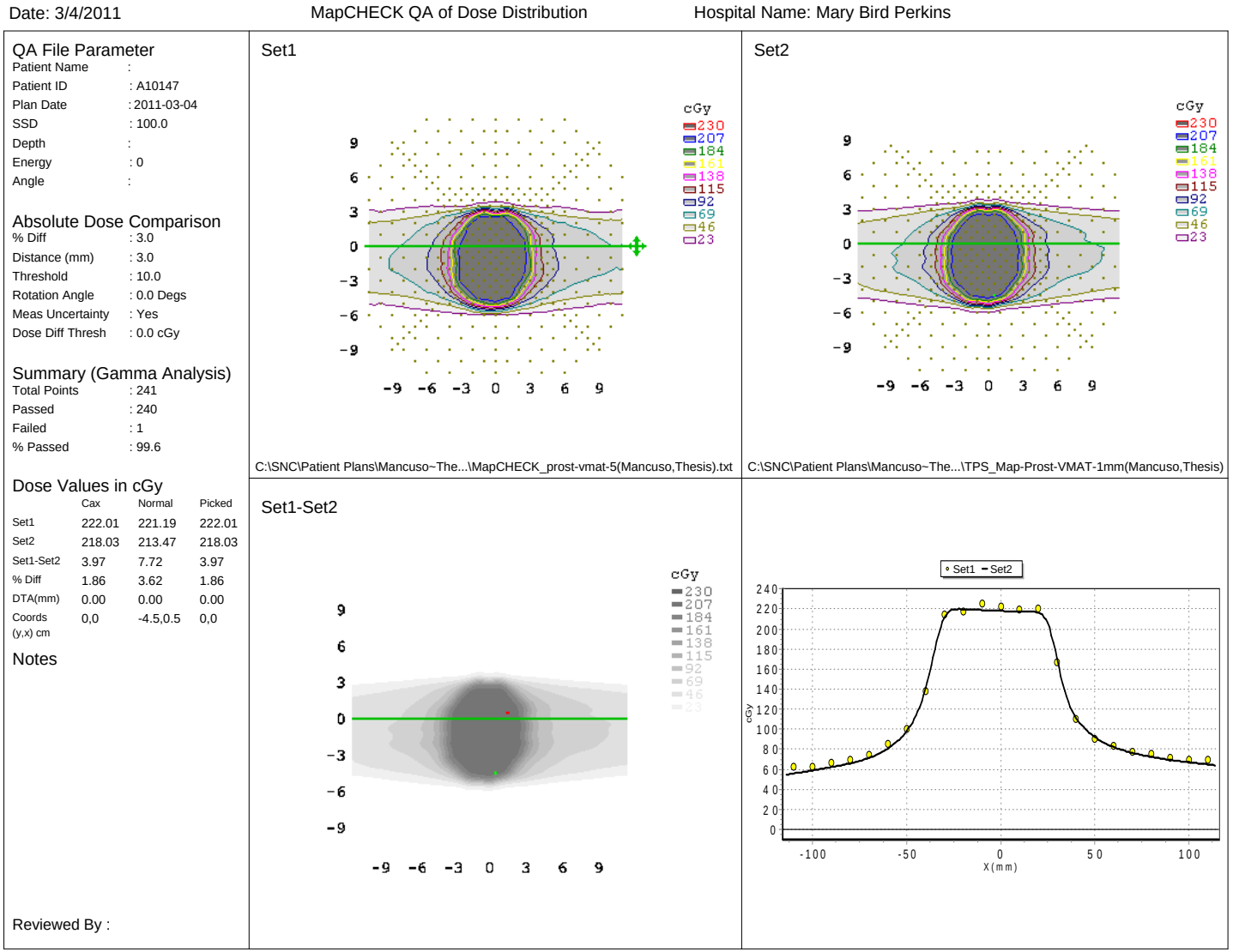

Figure B.28: Fifth MapCHECK result for the prostate VMAT delivery.

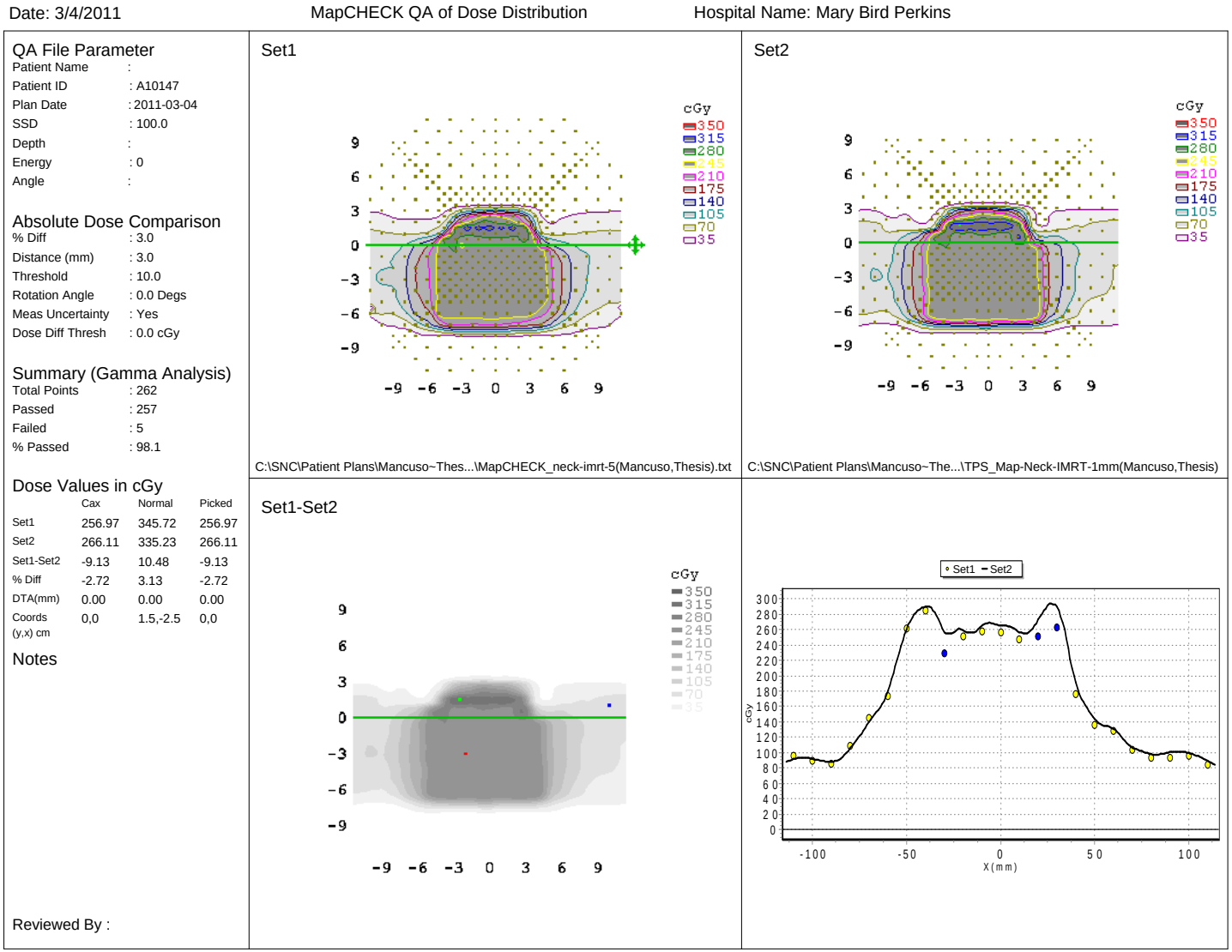

Figure B.29: Fifth MapCHECK result for the head and neck IMRT delivery.

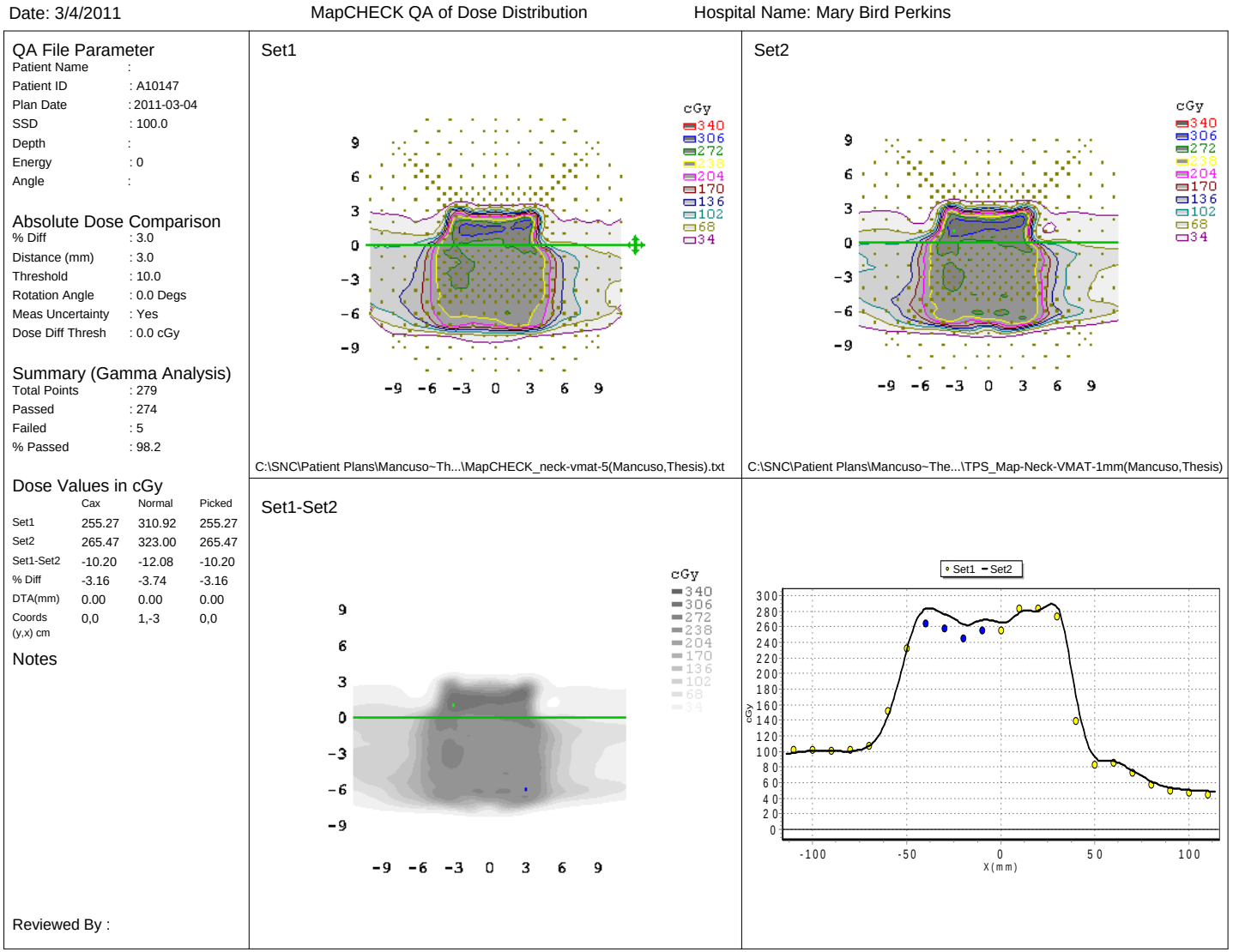

Figure B.30: Fifth MapCHECK result for the head and neck VMAT delivery.

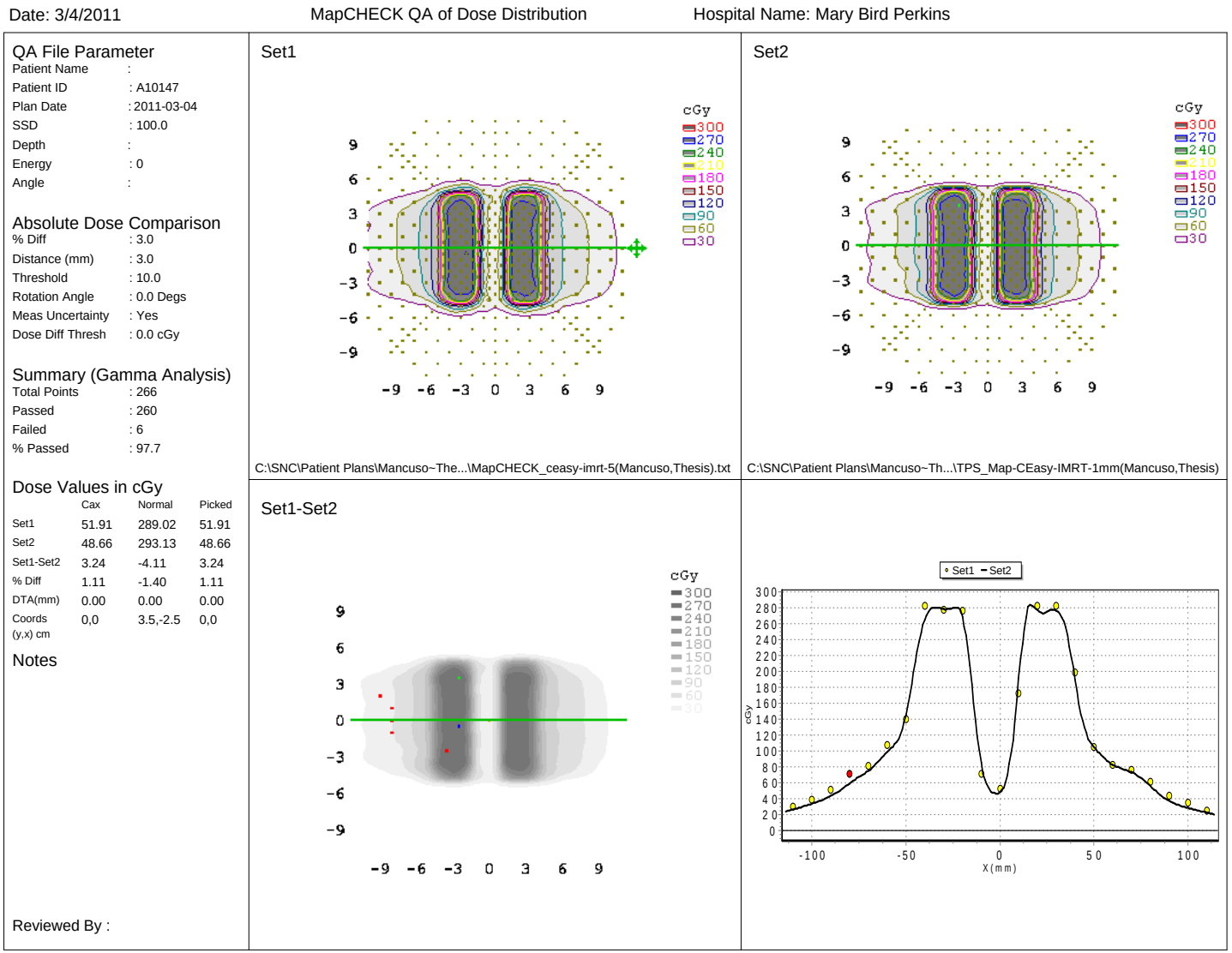

Figure B.31: Fifth MapCHECK result for the C-shape IMRT delivery.

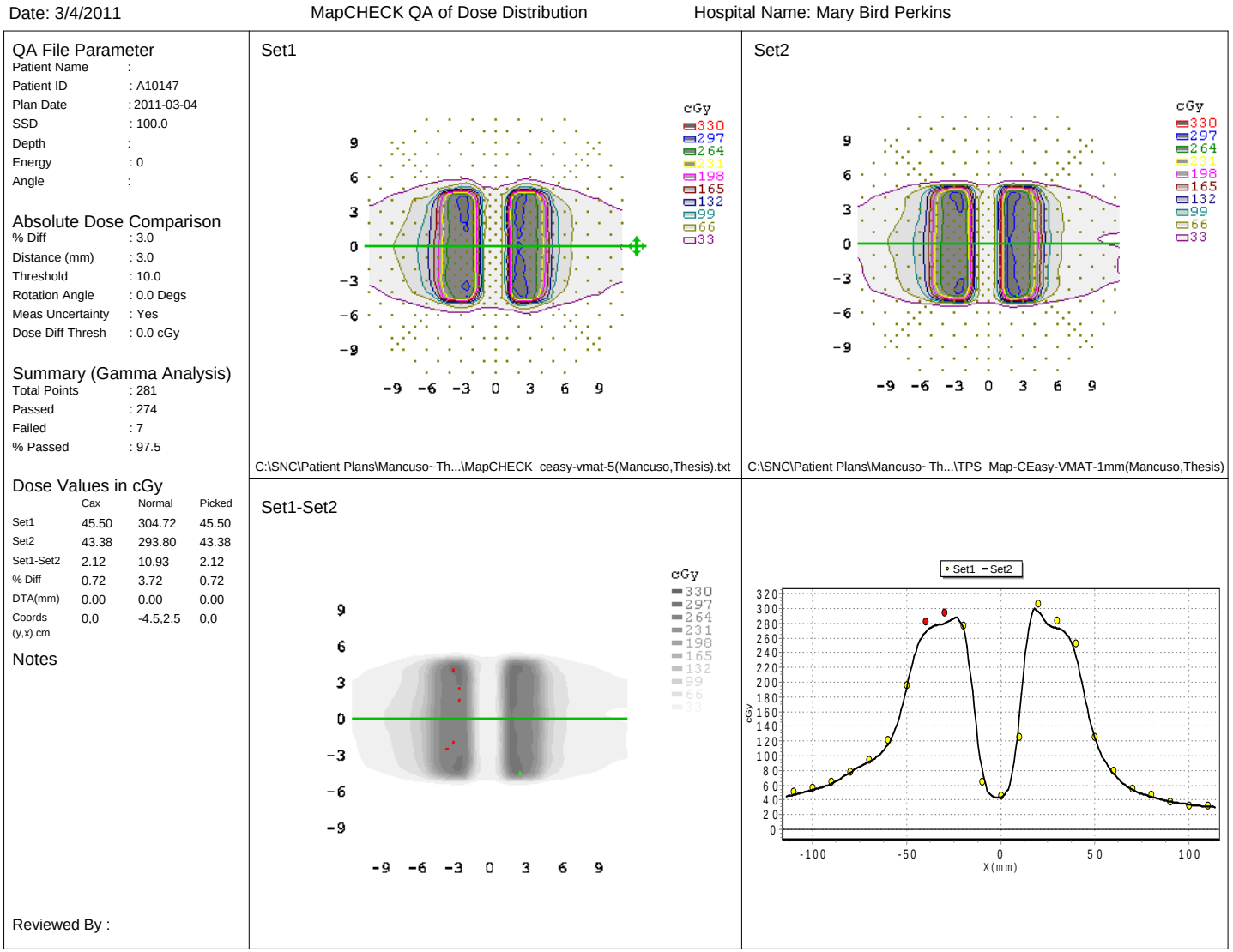

Figure B.32: Fifth MapCHECK result for the C-shape VMAT delivery.

Vita

Gordon Mancuso was born in Provo, Utah, in 1983, and grew up in Rochester, New York. He graduated from Greece Arcadia High School in 2002, and began pursuing a Bachelor of Science degree in physics at Brigham Young University later that year. From 2003 to 2005 he served as a missionary for The Church of Jesus Christ of Latter-day Saints in the Madagascar Antananarivo mission.

After finishing his undergraduate work at BYU in 2008, he moved to Baton Rouge, Louisiana, with his wonderful wife Megan, and began working on a master's degree in medical physics at Louisiana State University. Following graduation, he will begin a two year residency program at OncoLogics in Lafayette, Louisiana, where he will be trained further in clinical medical physics work. He plans to pursue a career in clinical medical physics. His last name is Italian and means "left-handed."